Vortex Dynamics and Instabilities in Ta_xGe_{1-x}/Ge Multilayers

by

Benjamin John Ruck

A thesis submitted to Victoria University of Wellington
in fulfilment of the requirements for the degree of
Doctor of Philosophy in Physics.

Victoria University of Wellington
November 1998

This thesis was prepared on a Macintosh 7200/120 computer using LaTeX 2ε. The thesis class which determined the formatting of the entire document was supplied by James Quilty.

Abstract

In this thesis the magnetic response of a layered type-II superconducting system is explored across the entire range of fields, temperatures and currents where superconductivity exists, with the results providing valuable insight into the role of reduced dimensionality in determining the behaviour of type-II materials such as the new high temperature superconductors. The system in question consists of alternating layers of amorphous Ta or Ta_xGe_{1-x} ($x \approx 0.3$) with amorphous Ge where the individual layer thicknesses vary between 17Å and 210Å. These multilayers were fabricated by vapour deposition in a high vacuum chamber which allowed the creation of samples with uniform layers of high purity. The resistive transport properties have been measured from T_c ($\approx$ 1-3 K) to temperatures as low as 50 mK in some cases, and in fields of up to 15 T. The upper critical fields have been determined from the fluctuation conductivity both with the field parallel and perpendicular to the layer plane of the samples. The results show clearly the dependence of the dimensionality on the superconducting layer thickness and the degree of coupling across the Ge layers. For the samples with the most two-dimensional properties the zero field resistive transition is governed by the unbinding of thermally created vortex-antivortex pairs as described by the Berezinskii-Kosterlitz-Thouless theory. A detailed investigation of the perpendicular field vortex states and dynamics has been performed, including measurement of the activation energies needed for thermally activated vortex motion. Qualitative difference are observed between the activation energies in two- and three-dimensional samples, with the barriers being generally higher in 3D. The non-linear current-voltage characteristics of the samples provide evidence for the existence of a vortex glass state which melts into a liquid below H_{c2}, although the divergence of the activation barriers in the glass can be restricted by the finite sample thickness. A brief investigation of the corresponding parallel field regime showed considerably less dissipation, due largely to the transparent nature of the Ge layers to the magnetic field. At the highest currents an instability is observed in the vortices which can drive the samples discontinuously back into the normal state. This instability is shown to be of the type predicted by Larkin and Ovchinnikov (LO), including quantitative agreement between the measured and predicted values of the critical vortex velocity. Several features of the instability are noted which are not specifically predicted by the LO theory, and comparisons are drawn between these and the prevailing vortex state at lower currents.

Acknowledgements

Firstly I would like to thank my supervisor Professor Joe Trodahl both for his guidance and continued encouragement on this project and for his tremendous assistance in helping me along the path to a career in physics. I also owe a huge debt of gratitude to Professor John Abele from Lewis and Clark College whose inspiration and generous hospitality provided the spark that set this research alight. Many thanks to Simon Brown[1] and Richard Newbury of the University of New South Wales for access to their dilution refrigerator and for their experimental assistance, along with a most enjoyable introduction to Sydney.

A big thank you to the technical staff at Victoria University, especially Jono Hewison, Dave Gilmour, Alan Rennie and Bill Leck, and also Steve Attinasi of Lewis and Clark College for their help with the many practical aspects of experimental physics research for which I am not qualified. I gratefully acknowledge the efforts of Leigh Johnson who began the Ta/Ge multilayer studies ahead of me and whose samples I was able to use, Kieran Newell who also provided one of the samples and C.K. Subramaniam (Mani) who taught me much about experimental techniques.

Thanks to all of my fellow students, especially James Quilty, Neil Kemp, Stephan Rupp, Kirk Collins and Jonas Törnquist who provided not only many stimulating discussions but also much light relief and companionship when it was needed. A further thank you to James Quilty for the use of his LaTeX document class and to Neil Kemp for the use of pictures from his honours thesis.

A warm thank you to my parents and to all of my friends and family for their encouragement and support. Lastly and very importantly I would like to thank Anne Vekony for her love and understanding. I look keenly forward to sharing the fruits of this endeavour with her. This research was partially supported by the New Zealand Foundation for Research Science and Technology.

[1] Present address: Department of Physics and Astronomy, Canterbury University, Private Bag 4800, Christchurch, New Zealand.

Contents

List of Figures

List of Tables

Chapter 1

Introduction

Ever since its discovery by H. Kamerlingh Onnes in 1911 [1] superconductivity has continued to present some of the most exciting and challenging problems in condensed matter physics. Of particular interest is the way in which superconductors interact with an applied magnetic field. It has long been known that two types of superconductors exist [2,3]; those known as type-I superconductors that exhibit the Meissner effect in which a magnetic field is completely expelled from the bulk, and those known as type-II superconductors that allow penetration of a magnetic field in the form of quantised vortices of magnetic flux. The existence of these vortices allows type-II materials to maintain superconducting order in much greater fields than type-I materials, giving type-II superconductors a considerable advantage in terms of their practical applications. These advantages, however, are not as straightforward as might be hoped because of the complexity introduced by the vortices themselves. Due to their magnetic nature the vortices interact with an applied current in such a way that they are compelled to move, with adverse effects on the superconductivity.

As a result of much intensive research a consistent theoretical description of these vortices began to emerge, based mainly on phenomenological models such as the Ginzburg–Landau theory which describe superconductivity from a macroscopic point of view [4]. These theories included a description of how and why vortex motion could affect superconductivity and seemed to provide a clear and coherent framework for understanding type-II materials. However in 1986 J.G. Bednorz and K.A. Müller [5] discovered an entirely new class of ceramic type-II superconductors with T_c higher than any previously known compounds. These new superconductors, known as the high-T_c's, displayed many new and unexplained phenomena particularly with regard to the vortex state, sparking an enormous resurgence of interest in type-II superconductivity [6]. It was quickly

discovered that superconductivity in these high-T_c materials is related to the existence of CuO_2 planes within the crystal structure which are coupled together through interleaving charge reservoir layers (the name high-T_c cuprates is commonly used). The layered structure gives rise to an anisotropy in the superconducting properties, and furthermore the degree of anisotropy was found to vary amongst the different high-T_c compounds. This immediately raised questions about the role of reduced dimensionality in determining how the high-T_c superconductors behave in a magnetic field. For example when the anisotropy is strong the vortex lines are not well defined between the superconducting layers, leading to a qualitatively different picture of the vortex state than in the isotropic case.

As well as the layering the complexity of the high-T_c superconductors is also related to their unusual characteristic length scales [6]. The first microscopic theory of superconductivity was provided in 1957 by J. Bardeen, L.N. Cooper and J.R. Schreiffer [7] (the BCS theory). The BCS theory showed that superconductivity results from the pairing of charge carriers which leads to the formation of a coherent wave function describing all of the pairs. The BCS theory, along with the Ginzburg–Landau theory, also implies two basic length scales associated with the superconductivity known as the coherence length ξ and the penetration depth λ. The coherence length determines the length scale over which the BCS wave function can vary whereas the penetration depth is the screening length which determines the scale of variation of the magnetic field within the superconductor. The distinction between type-I and type-II superconductors lies in the ratio of these two lengths, with type-I materials having $\lambda/\xi < 1/\sqrt{2}$ and type-II materials having $\lambda/\xi > 1/\sqrt{2}$.

All superconductors have a finite critical field $H_c(T)$ which marks the thermodynamic boundary between the superconducting and normal states. Type-I superconductors exhibit the Meissner effect right up until H_c, above which the superconductor reverts back to the normal state. Type-II superconductors on the other hand, exhibit the Meissner effect only up until a lower critical field $H_{c1} < H_c$, above which the vortex state is entered. This partial penetration of the field, termed the mixed state, allows superconductivity to persist up until the upper critical field $H_{c2} > H_c$. As well as the critical fields all superconductors have a finite critical current j_c which represents the maximum dissipationless current that can be carried in the superconducting state. An upper limit is placed on this by the depairing current j_0 which is given by

$$j_0 = \frac{\Phi_0}{3\sqrt{3}\pi\mu_0\lambda^2\xi} \tag{1.1}$$

where Φ_0 is the flux quantum (see Section 5.1.1) and μ_0 is the permeability of free space. At currents greater than j_0 the paired charge carriers tend to be broken up, thus destroying the superconductivity. In type-II superconductors however, j_c is usually limited to values well below j_0 by the vortices. As mentioned above the applied current interacts with the magnetic vortices via the Lorentz force, compelling them to move in a way that tends to take energy from the supercurrent and therefore gives rise to dissipation. In order to restore true superconductivity the vortices must be prevented from moving in some fashion, which can be achieved through the introduction of inhomogeneities to which the vortices are attracted. Therefore j_c is defined as the minimum current needed to induce motion of the vortices away from these so-called pinning sites, with the ratio j_c/j_0 providing an estimate of the strength of the pinning.

The combination of the critical fields and the critical current would appear to give a complete description of the superconducting state, defining sharply the boundary between superconducting and non-superconducting behaviour. However the sharpness of the boundary is reduced considerably by thermal fluctuations where the finite temperature of the sample allows for thermally activated motion of the vortices even at currents below j_c. The importance of thermally induced vortex motion can be measured by the so-called Ginzburg number [6] which is defined by

$$G_i = \frac{1}{2}\left(\frac{\gamma k_B T_c \mu_0}{4\pi B_c^2(0)\xi^3(0)}\right)^2 . \tag{1.2}$$

The Ginzburg number is the ratio of the thermal energy within a volume of dimension equal to the coherence length to the superconducting condensation energy in the same volume. When G_i is large thermal fluctuations play an important role in determining the superconducting properties. Equation 1.2 shows that G_i depends strongly on the parameter γ which provides a numerical measure of the degree of anisotropy induced by the layering (see Chapter 5).

In high-T_c superconductors G_i is significantly greater than the values found for conventional low-T_c materials, whereas the ratio j_c/j_0 is considerably less than typical low-T_c values. This tends to encourage motion of the vortices away from the pinning sites, and indeed the high-T_c superconductors do show significant flux motion at currents well below j_c (known as giant flux creep), although a detailed understanding of this phenomenon is still lacking. A complete description of the superconducting state must also cover the opposite regime of currents in excess of j_c. In the simplest case high currents would be expected to drive the vortices over the pinning sites resulting in free flux motion where the pinning

is irrelevant. Experimental results on the other hand, based on both high- and low-T_c systems, indicate that the details of the crossover to free flux flow depend critically on the field and temperature regime [8–14]. At high currents Larkin and Ovchinnikov [15, 16] have also predicted a fundamental instability in the moving vortex system which occurs when the vortices exceed a critical velocity. This instability is capable of driving the superconductor discontinuously into the normal state, although at this stage the details of the transition in the presence of pinning forces have not been fully explored.

The above discussion has made it clear that in the high-T_c superconductors there are a large number of parameters relating both to the sample morphology (such as the degree of anisotropy) and to the experimental setup (such as the strength of the applied current). The combination of this with the many unknown factors relating to the microscopic origin of the superconductivity makes an understanding of the high-T_c cuprates particularly difficult to achieve. Furthermore there is much fundamental interest in gaining an understanding of low dimensional systems and the various length scales which characterise them. One area which shows much hope of providing insight into the relationship between the many degrees of freedom is the systematic study of a model layered system where the parameters can be tailored continuously to represent either the two- or three-dimensional regime. This thesis presents the results of such a study based on multilayer samples of superconducting amorphous Ta or Ta_xGe_{1-x} interleaved with non-superconducting amorphous Ge. This system was chosen due to the high degree of disorder with which the films grow [17] which causes these low-T_c materials to be strongly type-II and therefore better able to mimic high-T_c superconductors. Because the individual layer thicknesses are controllable the multilayers can be manufactured to represent the entire range from weakly layered three-dimensional systems through to highly anisotropic (decoupled) two-dimensional systems. The fundamental interest in the study of such a system should also not be overlooked simply because of the diversity of the physics involved.

Several previous studies have been performed on similar systems, most notably using Nb/Ge [18–22], Mo/Ge [8, 9, 23–26] or YBCO/PrBCO [27–29] based multilayers and thin films, although numerous other systems have also been investigated [30–34]. As expected these systems have provided many fascinating results, but as yet a complete understanding of their temperature/magnetic field phase diagrams has not been realised, thus warranting the study of a comple-

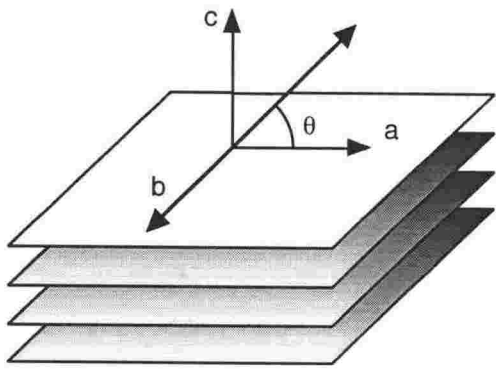

Figure 1.1: The multilayer coordinate system showing the ab plane, the c direction and a definition of the angle θ.

mentary system. Furthermore the use of the Ta_xGe_{1-x}/Ge[1] system with its lower T_c's actually has several advantages over the higher T_c systems mentioned above, as will be described in the following chapters. In this study the resistive transport properties (especially the current-voltage (IV) characteristics) of the Ta_xGe_{1-x}/Ge multilayers have been investigated for a wide range of anisotropies in order to try and determine the effects of the layering. Measurements have been made over the whole range of temperatures and fields below $H_{c2}(T)$ and also using applied currents both well below and well above j_c. The transport current is applied parallel to the layer planes, but the angle θ between the field and the layers is varied from parallel to perpendicular. The coordinate system used to describe these measurements is illustrated in Figure 1.1 where the two equivalent in-plane axes have been marked a and b and the out-of-plane axis has been marked c to coincide with the notation used to describe the high-T_c superconductors.

SI units are used in all equations throughout this thesis with $\mu_0 = 4\pi \times 10^{-7}\,\mathrm{N/A^2}$, however for convenience the symbol H will be used in the text and figures to refer to the applied field in Teslas rather than writing $\mu_0 H$, and similarly the symbol H_{c2} will be used for the critical fields in Teslas. Note also that in type-II superconductors with large values of the Ginzburg–Landau parameter κ it can be shown that in equilibrium the microscopic field B is approximately equal to the applied field $\mu_0 H$ (referred to here as H) for nearly all values of H [2].

[1]Note that pure Ta/Ge multilayers are just a special case of Ta_xGe_{1-x}/Ge multilayers with $x = 1$. Single layer samples are also a special case where the number of layers is one.

Chapter 2

Sample Fabrication

As mentioned in Chapter 1 numerous authors have conducted investigations into the superconducting properties of amorphous thin films and multilayers. In these studies a variety of techniques have been employed to manufacture the samples such as sputtering [8, 9, 18–26, 30, 34, 35] and molecular beam epitaxy onto cryogenically cooled substrates [31]. In the present study of amorphous multilayers and films of Ta and Ge the samples were prepared by evaporative deposition in an ultra high vacuum system using a resistive boat for the Ge and an electron gun for the Ta. This kind of evaporative deposition is relatively simple, and in the case of Ta and Ge it can be employed to make amorphous samples with a wide range of layer thicknesses without the need for any substrate cooling. The evaporations were performed under high vacuum to ensure that the evaporation pressures were low enough to produce high purity samples.

A selection of samples was needed in order to trace the superconducting properties from the limit of decoupled two dimensional layers to coupled three dimensional layered systems. To satisfy this requirement three types of samples were fabricated. The first type of sample consisted of layers of pure Ta multilayered with pure Ge. This type of sample formed the starting point for this investigation as it has been used previously for a detailed study of the normal state properties of amorphous multilayers [17, 36]. A second type of multilayer was also employed which consisted of alloyed Ta_xGe_{1-x} layers and pure Ge layers. These alloyed multilayer samples had a higher T_c than the samples with pure Ta layers meaning that a greater portion of the magnetic phase diagram was accessible to experiment. The third type of sample was a single layer Ta_xGe_{1-x} alloy which was used to help with the interpretation of the multilayer data. Details of the substrates, vacuum system, the evaporation techniques and a discussion of the films produced are given in this chapter.

2.1 Substrates and Sources

All of the samples for transport measurements were prepared on glass substrates cut from microscope slides to either 13 or 18 mm diameter. The substrates were cleaned immediately before insertion into the vacuum system in a multi-step process as described by Johnson [17]. The first step involved an initial clean using acetone to remove the bulk of any grease on the substrates. This was followed by a brief immersion in a solution of water, HNO_3 and HF[1] (ratios 12:7:1) and several rinses in distilled water to remove any excess acid. The substrates were then placed in a fresh volume of distilled water and put into an ultrasonic bath for approximately 30 minutes, with the water being changed at least once during this stage of the cleaning process. Finally the substrates were dried in a stream of instrument grade (99.99% pure) nitrogen gas. All substrates were inspected visually before use to check for streaking or scratches on the glass. During fabrication of the pure Ta/Ge multilayers additional films were grown on mylar substrates for later inspection by Transmission Electron Microscopy (see Chapter 3). Before use these substrates were cleaned with a rinse in acetone followed by drying in instrument grade nitrogen gas.

Two different Ge sources were employed to fabricate the samples. The first source, which was used to make the multilayers with pure Ta layers, consisted of 99.999% pure Ge lumps of typical dimension 20 mm supplied by Goodfellow Cambridge Ltd. The large chunks were broken up before use to improve the thermal contact with the resistive boat. The second Ge source, which was used to make the samples with alloyed Ta_xGe_{1-x} layers and also the single layer alloy, consisted of 99.999% pure Ge granules of typical size 3–5 mm, also supplied by Goodfellow. The small granules of this source maintained better thermal contact with the boat leading to a lower incidence of the boat cracking under thermal stress.

Similarly, two different Ta sources were used for the evaporations. The first source consisted of high purity (impurities < 20 ppm), 0.030″ diameter Ta wire supplied by Electronic Space Products International (ESPI). The wire was wound into a tight coil and placed in the electron gun to be used with the rotating substrate assembly to make the pure Ta multilayers. Some difficulties were experienced in maintaining a steady rate with this source due to the tendency for sections of the wire to be melted through. A second source consisting of 10 mm diameter Ta rod (purity 99.95%) was obtained from Princeton Scientific Corpo-

[1] HF is commonly used to etch glass so care had to be taken not to expose the substrates to the acid solution for too long.

ration for use in the evaporation of the alloy multilayers and single layer sample. With this source excellent Ta evaporation rate stability was achieved.

2.2 Vacuum Systems

Two different configurations of the Varian *FC-12E Ultra High Vacuum System* were used for the preparation of the two different types of multilayer samples. A third configuration was used in a separate *FC-12E* vacuum system to prepare single layer alloy samples, however many of the aspects of the evaporations were common to each setup. Most importantly, in each case the vacuum chamber was pumped down to very low pressures in order to evaporate pure samples. The procedure for pumping down the system used to fabricate the multilayers was as follows. Firstly the vacuum chamber was cleaned using tissue paper soaked in isopropyl alcohol. Any excess material was removed from the bottom of the chamber with a vacuum cleaner. The chamber was then sealed and initially roughed with either a venturi pump or a diaphragm pump. This was followed by pumping with a set of two Varian *Vacsorb* sorption pumps to bring the pressure down below 5×10^{-5} Torr at which point the poppet valve to the lower chamber was opened allowing the five Varian *Vacion* pumps and the three filament titanium sublimation pump to operate. The pressure then dropped rapidly to around 10^{-7} Torr allowing the sources to be outgassed by mild heating. The entire system was wrapped in heating coils and insulation which was used to bake the system at a temperature of around 100°C for several days. During this time the Ta source was further outgassed to prevent a significant rise in pressure during evaporation caused by the outgassing of the components surrounding the electron gun. After the chamber cooled further pumping with the ion pumps and the titanium sublimation pump reduced the pressure to the final value of less than 10^{-9} Torr. The procedure for pumping down the system used for the single layer alloy samples differed only in that this system lacked a poppet valve to isolate the ion pumps when the system was opened. This meant that the entire system had to be roughed out and the ion pumps restarted for each evaporation, but nevertheless the final pressures obtained were comparable for both systems.

For the evaporation of the multilayers the Ta was evaporated by a 2kW Varian *e-Gun* at rates of between 43 and 115Å·min^{-1} at the substrates, and the Ge was evaporated from a resistively heated tungsten boat at rates of between 140 and 1200Å·min^{-1}. Comparable rates were used for the evaporation of the single layer alloy. Earlier evaporations were controlled by two Sloan *DDC-1000 Digital*

Deposition Controllers, however these deposition controllers were upgraded and later evaporations were controlled by two Sycon Instruments *STC-200/SQ Deposition Rate Controllers* which linked each source in a feedback loop with a quartz crystal rate monitor. Fluctuations in the evaporation rates of both sources were typically on very short time scales so that the fluctuations averaged out over the thickness of a layer. The overall rate stabilities measured at the sensors were thus very good at about ±5–10%.

There are, however, additional sources of uncertainty in the determination of the actual evaporation rate at the substrates. In the multilayer system the substrates are positioned below the sensors meaning that the rate at the sensors is not the same as the rate at the substrates. This is further complicated by the fact that the substrates are distributed around the vacuum chambers such that the source to substrate distance is not the same in each case. The effects of this were partly compensated for by the inclusion of a tooling factor in the deposition controllers, determined from the approximate equation

$$T \equiv \frac{R_{sub}}{R_m} \approx \frac{r_m^2}{r_{sub}^2} \tag{2.1}$$

where R_{sub} is the actual rate at the substrates, R_m is the rate measured at the sensors, r_{sub} is the average source to substrate distance and r_m is the source to sensor distance. Characterisation of the samples performed after the evaporations (see Chapter 3) indicated that the calculated tooling factor (≈1.7 for both sources) was close to the actual value.

The evaporated flux from the electron gun was also somewhat unevenly distributed around the vacuum chamber where it tended to be concentrated forward of the gun. The size of the variation in evaporation rate between the most widely spaced substrates was estimated to be less than 30% based on measurements on the single layer alloy evaporation system (see Section 2.2.2 and also [37]). Fortunately, although this adds to the uncertainty in setting the desired rate it does not lead to appreciable rate fluctuations. Thus the layers will still be uniform and the only effect is a slight deviation from the desired layer thickness or alloy concentration. For example, for a desired alloy concentration of 30 atomic% Ta the 30% variation in Ta evaporation rate leads to a difference in Ta concentration of about 10% between the most widely spaced samples.

To help to quantify the uncertainties in the rate determination glass slides were placed in the vacuum chamber near the substrates in such a way that they were exposed to one or other of the sources for the entire duration of the evaporation. Upon completion of the evaporation these slides were removed and

Multiple Beam Interferometry (MBI) was used to measure the total deposited thickness of the Ta or Ge on the slides (see Chapter 3). It is important to note that these slides were exposed to the sources not just during the actual deposition, but also while the shutter was in the shut position. Thus, to determine the total thickness deposited on the substrates the thickness measured by MBI had to be corrected for the time during which the substrates were not exposed to the source.

2.2.1 Multilayer Deposition

The pure Ta/Ge multilayers were made using a rotating substrate assembly designed by Williams [39] using a procedure described extensively by both Williams and by Johnson [17]. The basic idea is that the substrates are rotated alternately through the separate streams of evaporated flux, thus producing the layered structure. The substrates are mounted on one of three geared wheels attached to an external stepping motor which provides the rotation. Each of the geared wheels holds two 13 mm diameter glass substrates, two 18 mm diameter glass substrates and two 18 mm diameter mylar substrates. The layer thicknesses are determined by the speed of the stepping motor, the rate of evaporation and the gearing of the wheels holding the substrates. A shutter was used to control the start and finish time of the evaporations.

It proved difficult to manufacture the Ta_xGe_{1-x}/Ge multilayers using the rotating substrate assembly so the vacuum chamber was modified to the simpler configuration shown schematically in Figure 2.1. The top view of the vacuum chamber is shown in Figure 2.2 illustrating the position of the sensors and substrates relative to the sources. Here the substrates are mounted in a fixed substrate holder and the incident flux is controlled by an externally operated shutter with three operating positions. In the first position (marked [A] in Figure 2.1) the shutter is closed and no flux reaches the substrates. This position was used at the start of the evaporation while the sources are being conditioned and also after completion of the evaporation. In the second position (marked [B]) the substrates are exposed only to the Ge source while in the third position (marked [C]) the substrates are exposed to both the Ge and the Ta sources. The layered structure was created by repeatedly switching the shutter from position [A] to position [C]. The layer thicknesses were determined by the evaporation rates and the time between the switching of the shutter, whereas the concentration of the alloy in the Ta_xGe_{1-x} layers was determined solely by the ratio of the evaporation rates at the substrates. During all evaporations it was ensured that both the top and

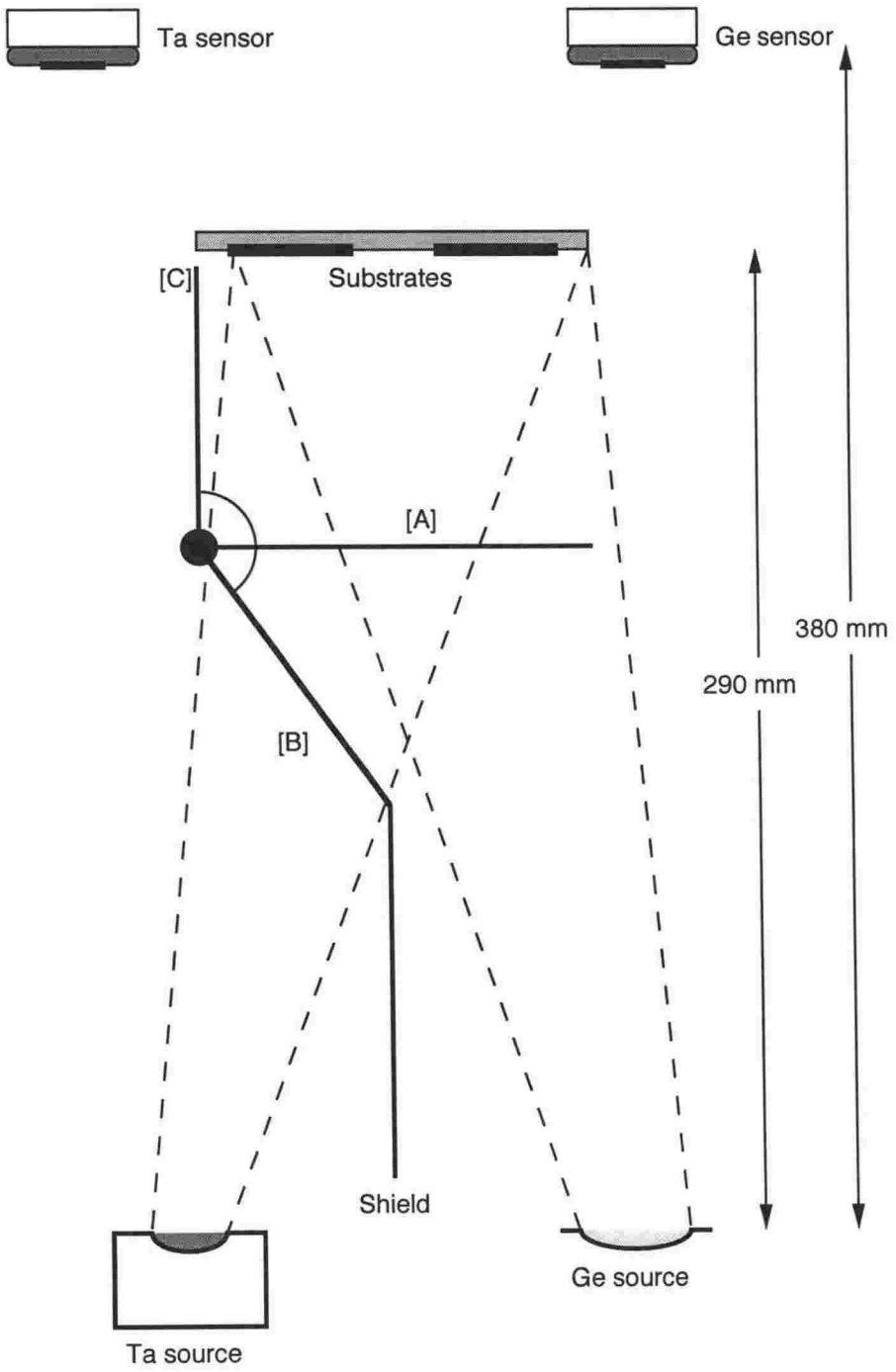

Figure 2.1: A schematic view of the vacuum chamber setup used to make the Ta_xGe_{1-x}/Ge multilayers (not to scale). The three shutter positions are: [A] Shut; [B] Ge only; [C] Ta_xGe_{1-x}.

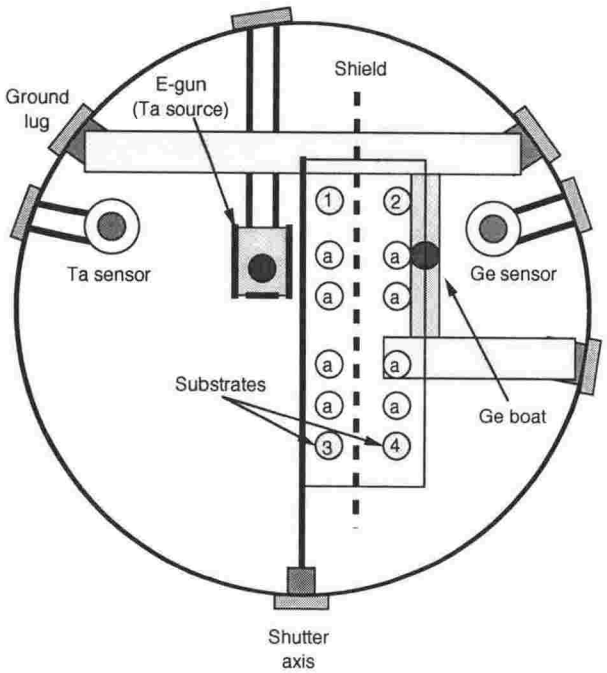

Figure 2.2: Top view of the vacuum chamber setup used to make the Ta_xGe_{1-x}/Ge multilayers (approximately to scale). The diameter of the vacuum chamber is 280 mm. The positions of the substrates used in this study are marked 1–4. The substrates marked with an *a* are obliquely deposited multilayers used in a separate study [38].

bottom layers were Ge thus giving the samples some protection against exposure to the environment. The quartz crystal monitors were exposed to their respective sources at all times.

2.2.2 Single Layer Alloys

Single layer alloy samples were fabricated in a similar manner to the alloyed multilayer samples but in a different vacuum chamber[2]. Identical sources, controllers and monitors were used in both systems. A schematic view of the vacuum chamber is shown in Figure 2.3 and the top view is shown in Figure 2.4. Once again an externally operated shutter was employed in the system but in this case the only function of the shutter was to cover the substrates before the start and after the end of the evaporation. While the shutter was open the substrates were exposed to both sources thus forming a single alloy layer, where the composition of the alloy was determined by the relative rates of evaporation of the two sources. It can be seen from the top view that a range of samples were prepared in each evaporation. Due to the spatially inhomogeneous nature of the evaporated Ta flux each of these samples had a different alloy composition which depended

[2]The vacuum chamber setup was designed by Keiran Newell who also performed the evaporation of these samples.

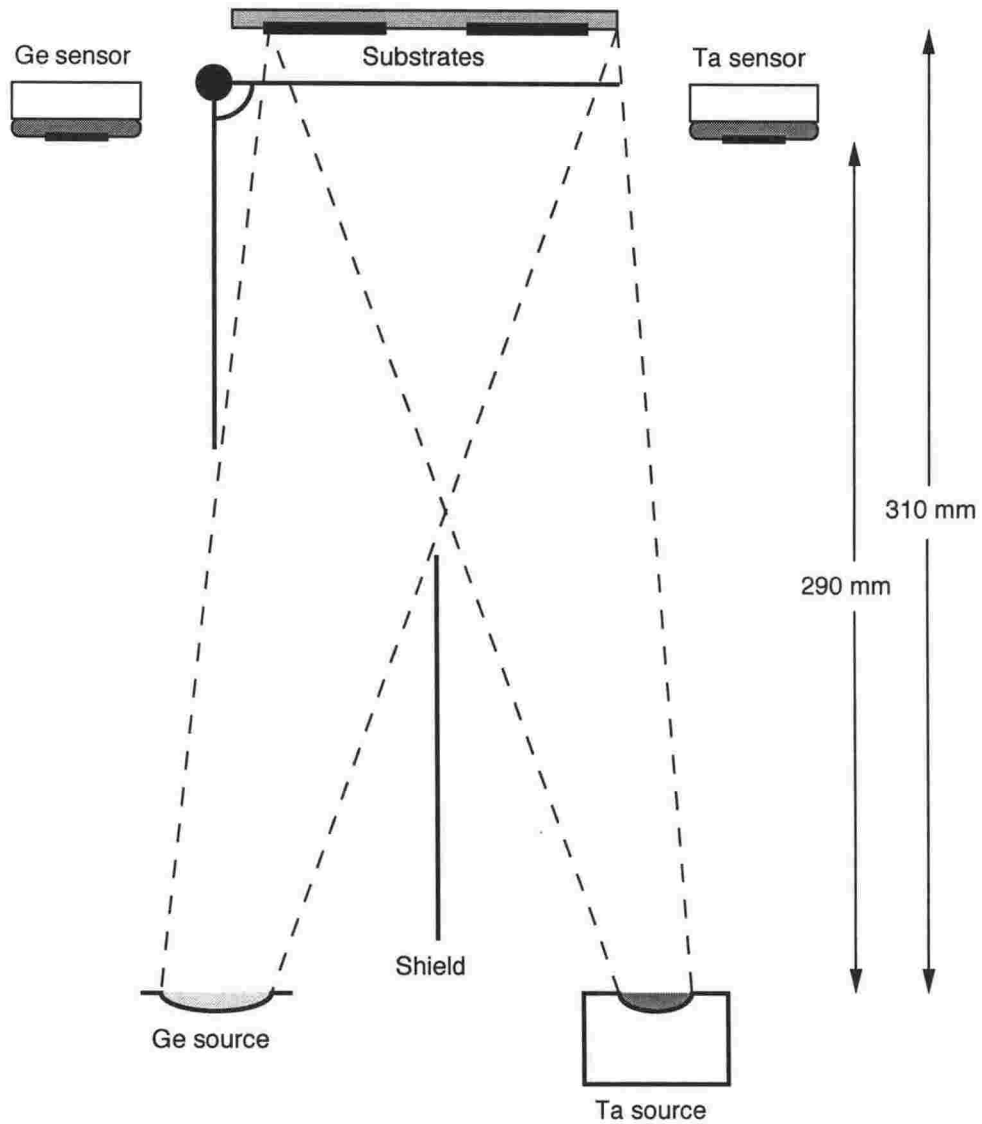

Figure 2.3: A schematic view of the vacuum chamber setup used to make the single layer Ta_xGe_{1-x} alloys (not to scale).

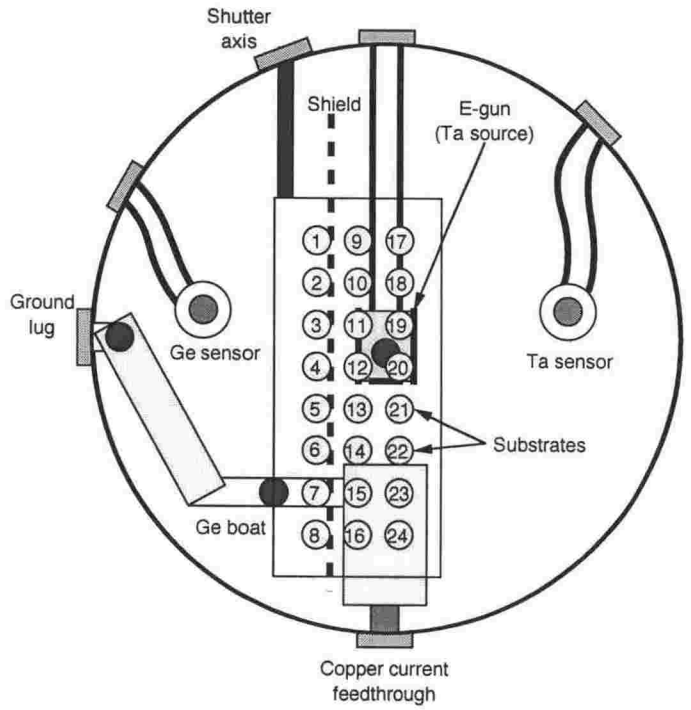

Figure 2.4: Top view of the vacuum chamber setup used to make the single layer Ta_xGe_{1-x} alloys, showing the positions of the sensors and substrates relative to the sources (approximately to scale). The diameter of the vacuum chamber is 280 mm.

on the position of the substrate in the vacuum chamber. As mentioned above, characterisation of these samples indicated that the variation in evaporation rate across the size of the substrate holder was about 30%.

2.3 Deposition Parameters

The details relating to the evaporations of all of the samples used in this investigation are displayed in Table 2.1. The name of each of the samples is a combination of the number of the run in which it was made and the position of the sample in the vacuum chamber (see Figures 2.2 and 2.4 and also Ref. [17]). The column entitled Setup refers to the three vacuum chamber configurations with which the samples were made. Samples marked I have pure Ta superconducting layers and were made with the rotating substrate assembly. The sample marked II is a single layer alloy. Samples marked III have Ta_xGe_{1-x} alloy superconducting layers and were made with the fixed substrate setup. So, for example, sample 60/3G4 is a multilayer with pure Ta layers made with the rotating substrate assembly during run number 60. The G refers to the fact that the substrate was glass. The sample was in the fourth position on the third substrate wheel. Similarly sample 5/G1 is a multilayer with alloyed Ta_xGe_{1-x} layers, where the substrate was in

position 1 of the substrate holder during run number 5 of the alloyed multilayer fabrication process.

The column entitled #Layers gives the number of superconducting layers in the sample. The column labeled r_{Ta} gives the Ta evaporation rate set on the deposition controllers. This rate includes the tooling factor calculated from Equation 2.1, so should give a fair approximation to the actual rate at the substrates. In order to maximise the T_c of the alloy samples the evaporation rates were set such that the alloy composition was approximately 30 atomic% Ta (i.e. $Ta_{0.3}Ge_{0.7}$) [40].

The Maximum Evaporation Pressure (M.E.P.) is critical in determining the level of impurities captured in the sample during evaporation. Baker [41] has given a method for determining the ratio R of the arrival rates of Ta and of residual gas at the substrate which depends on the partial pressure of residual gas P and the evaporation rate r via

$$R = 2 \times 10^{-8} \frac{r}{P} \tag{2.2}$$

where r is in Å·min^{-1} and P is in Torr. From this and the sticking coefficient of the residual gas α_s (assumed to be oxygen on Ta, $\alpha_s = 10^{-2}$) Johnson [17] calculates the maximum impurity concentration in the Ta layers (α_s/R). A similar calculation is given here, although it should be noted that this is strictly valid only for pure Ta multilayers and not the alloyed multilayers or single layer. In the case of the alloyed samples the evaporation rate used is the sum of the Ta and Ge rates where the Ge rate was 165 Å·min^{-1} for the single layer sample and 255 Å·min^{-1} for each of the multilayers. The impurity concentration calculated for these samples is likely to overestimate the actual value due to the effectiveness of pure Ta as a getter [42], and instead provides an upper estimate of the impurity level. In any case the calculations indicate a range in the purities of the superconducting layers, although all samples have less than 2.3% calculated impurity levels due to the use of the ultra high vacuum chambers.

As a further comment it should be noted that in these amorphous superconductors impurities may actually enhance the flux pinning characteristics of the films [6, 43, 44]. Thus, although impurities make exact characterisation of the films more difficult, such films are still of interest in this study.

Sample	Setup	#Layers	r_{Ta} (Å·min^{-1})	M.E.P. (Torr)	Impurity %
29/2G4†	I	15	56	1×10^{-8}	0.009
30/3G4†	I	5	115	4×10^{-9}	0.002
32/2G1†	I	14	43	2×10^{-6}	2.3
33/1G4†	I	17	108	1×10^{-6}	0.46
36/2G1†	I	12	65	2×10^{-7}	0.15
60/3G1‡	I	25	115	1×10^{-7}	0.043
60/3G4‡	I	25	115	1×10^{-7}	0.043
2/G6††	II	1	61	8×10^{-7}	0.18
5/G1	III	12	102	5×10^{-6}	0.7
5/G2	III	12	102	5×10^{-6}	0.7
6/G2	III	8	102	2×10^{-6}	0.28
7/G1§	III	13	112	1×10^{-7}	0.014

Table 2.1: The main parameters associated with the fabrication of each sample used in this study. Samples marked with a † were grown by H.L. Johnson, those with a ‡ were grown by C.K. Subramaniam and B.J. Ruck, those with a †† were grown by K. Newell and those with a § were grown by O. Pantoja and H.J. Trodahl. All others were grown by B.J. Ruck and S. Rupp.

2.4 Summary

This chapter has provided a discussion of the method of fabrication of all of the samples used in this investigation. Details of the basic characteristics aimed for in each sample have also been provided. Further details on the characterisation of the samples are contained in Chapter 3, where, among other things, determinations are made of the actual layer thicknesses and the alloy concentration.

Chapter 3

Sample Characterisation

In order to interpret the experimental data in a meaningful way it is neccessary to have an accurate knowledge of the morphology of the samples. The parameters of interest include the layer thicknesses, the diffuseness of the layer boundaries and the composition and structure of the individual layers. In Chapter 2 it was shown that the growth of the multilayers can be tailored through careful control of the deposition parameters, however it is clearly desirable to perform independent measurements to investigate the samples after the fabrication process. This chapter presents the results obtained from a variety of techniques aimed at sample characterisation. The techniques used were Multiple Beam Interferometry, Rutherford Back Scattering, X-Ray Fluorescence, Transmission Electron Microscopy and Ion Beam Thinning. A summary of the most accurate results from the characterisation is given near the end of the chapter.

3.1 Multiple Beam Interferometry

Multiple Beam Interferometry (MBI) is a simple technique which may be used to measure the thickness of a thin film. It is used here to measure the total thickness of Ta or Ge deposited onto glass slides placed in the multilayer vacuum chamber in such a way that the slides were exposed to one or the other evaporant throughout the entire evaporation. No MBI measurements were undertaken in the vacuum chamber used to make single layer alloys. The slides were placed as closely as possible to the substrates so that the evaporation rate at the slides and at the substrates was similar. Thus, a measure of the thickness of the films on the slides enables a calibration of the evaporation rate at the substrates which in turn enables the layer thicknesses and also the compositions of the alloy multilayers to be determined.

MBI relies on the interference fringes produced when monochromatic light is shone onto two nonparallel surfaces which have been brought together to produce a wedge of air. If there is a change in height of one of the surfaces due to the existence of a thin film covering part of the surface then there will be a discontinuity in the interference fringes of a size proportional to the thickness of the film.

To produce the step needed to perform MBI measurements it was neccessary to partially mask the slides during the evaporation. To observe clear fringes it is also helpful to have a highly reflecting surface so a layer of aluminium of approximate thickness 1000 Å was deposited over the entire surface. This left the height of the step at the edge of the film unchanged, although it did tend to broaden the width of the step somewhat. In practice a slight broadening of the step is desirable as it smoothes the discontinuity in the interference fringes making them easier to follow. A Varian *Å-scope* interferometer was used to measure the thickness of the films deposited on the slides.

For the pure multilayer samples a total of four slides were distributed above the Ta source and a further two slides were placed above the Ge source. The thickness of the film on each slide was measured and the amount deposited onto each of the samples was determined from the average thickness on the two closest slides. This helped to account for the nonuniformity of the Ta rate in the vacuum chamber as discussed in Chapter 2. The method used for calculating the thickness of the layers from the film thickness on the slide has been given by Johnson [17].

For the alloyed multilayers two slides were placed above the Ta source and one was placed above the Ge source. The Ta evaporation rate at the substrates was then estimated from the average thickness on the two slides above the Ta source. The calculation of the layer thickness and alloy composition of these samples from the MBI measurements was as follows. Firstly the actual Ge and Ta evaporation rates were calculated using

$$r_x = \frac{D_x(1-c)}{T} \tag{3.1}$$

where r_x is the evaporation rate of source x, D_x is the total evaporated thickness from source x determined by the MBI measurement and T is the total evaporation time. The thickness D_x is adjusted down by a factor $(1-c)$ to account for the amount deposited on the slide during the conditioning of the source. The amount c is estimated from the ratio of the thickness measured by the quartz crystal rate monitors at the start and at the end of the evaporation, and was typically much less than one. From the Ta and Ge evaporation rates the thickness of the layers

can be calculated according to

$$d_{\mathrm{Ge}} = r_{\mathrm{Ge}} \times t_{\mathrm{Ge}} \tag{3.2}$$

$$d_{\mathrm{Ta}_x\mathrm{Ge}_{1-x}} = (r_{\mathrm{Ge}} + r_{\mathrm{Ta}}) \times t_{\mathrm{Ta}_x\mathrm{Ge}_{1-x}} \tag{3.3}$$

where t_x is the evaporation time for the individual layer x. The atomic percentage of Ta in the alloy layer is calculated in a similar fashion according to

$$\%\mathrm{Ta} = \frac{r_{\mathrm{Ta}}\rho_{\mathrm{Ta}}}{r_{\mathrm{Ge}}\rho_{\mathrm{Ge}} + r_{\mathrm{Ta}}\rho_{\mathrm{Ta}}} \tag{3.4}$$

where ρ_x is the atomic density of the evaporant. The MBI results are summarised in Table 3.1, where the uncertainties result from a combination of the variation between the different films and the resolution of the *Å-scope* itself. The columns entitled d_{Ta}, $d_{\mathrm{Ta}_x\mathrm{Ge}_{1-x}}$ and d_{Ge} give the calculated thicknesses of the individual Ta, $\mathrm{Ta}_x\mathrm{Ge}_{1-x}$ or Ge layers respectively. The column entitled %Ta gives the calculated Ta concentration in the alloyed layer of the alloyed multilayer samples.

It is also important to note that several approximations have to be made when calculating the sample characteristics from the MBI measurements. Firstly the rate at the substrates is assumed to be the same as the rate at the slides. The use of more than one slide for the MBI measurements partly compensates for this, but differences in height from the sources between the slides and the substrates adds an uncertainty of up to 2% to the determination of the layer thicknesses of the pure Ta multilayers, and up to 10% uncertainty to the alloy multilayer layer thicknesses. Harder to quantify is the uncertainty involved in assuming that the density of the material in the multilayers is the same as the density of the much thicker MBI films. This is likely to be most severe in the case of the alloyed layers where it has been assumed that the layer thickness is simply the sum of the individual evaporation rates multiplied by the time of evaporation. In reality the density of the amorphous layers is likely to be somewhat less than the density of the bulk MBI films. Nevertheless MBI provides a good method for approximating some of the sample characteristics, and serves as a consistency check for further characterisation methods.

Sample	d_{Ta} (Å)	$d_{Ta_xGe_{1-x}}$ (Å)	d_{Ge} (Å)	%Ta (x)
29/2G4	17±2	-	151±5	-
30/3G4	100±10	-	131±2	-
32/2G1	18±3	-	82±2	-
33/1G4	26±6	-	53±2	-
36/2G1	53±6	-	50±1	-
60/3G1	15±2	-	23±1	-
60/3G4	15±2	-	23±1	-
2/G6	-	-	-	-
5/G1	-	56±3	170±9	30±5
5/G2	-	56±3	170±9	30±5
6/G2	-	190±20	180±10	37±6
7/G1	-	-	-	-

Table 3.1: Individual layer thicknesses and alloy layer composition for each of the samples as determined from MBI measurements (where available).

3.2 Rutherford Back Scattering

Rutherford Back Scattering (RBS) is a more accurate technique than MBI for determining the total amount of each evaporant deposited onto the substrate during the evaporation. In RBS experiments a monoenergetic beam of charged particles (usually He^+) is scattered from the charged nucleii of the atoms in the sample. The distribution of energies of the scattered particles allows a determination of the absolute concentration of each atomic species in the sample. The results appear as a two-dimensional atomic densities i.e. in units of atoms per unit area.

RBS has been performed on the pure Ta multilayers by Johnson [17] who gives a complete description of both the theory and experimental details of the process.

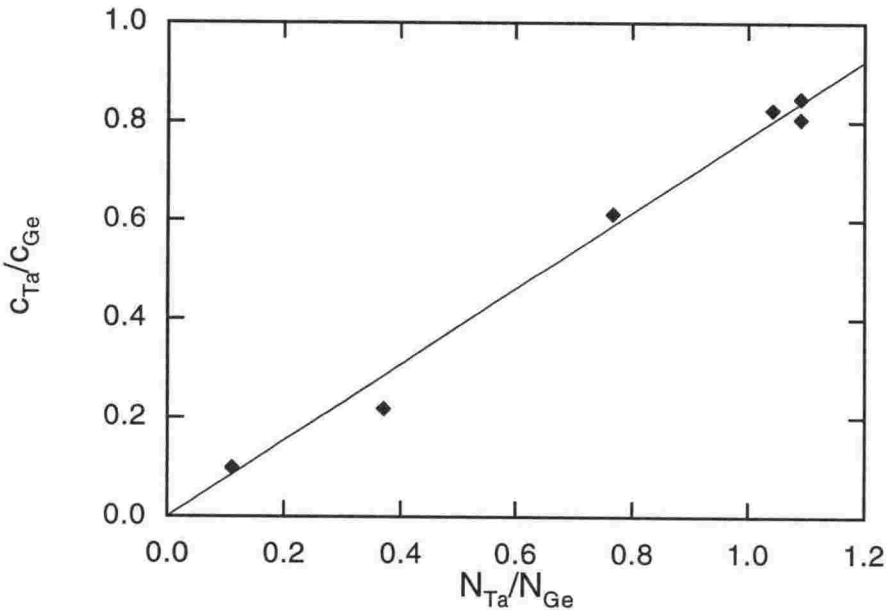

Figure 3.1: X-Ray Fluorescence calibration curve. The horizontal axis shows the ratio of known atomic percentages, while the vertical axis shows the ratio of counts in the Ta and Ge peaks.

For the purposes of this study only the results are quoted here (at the end of Section 3.3). The layer thicknesses have been calculated from the two-dimensional atomic densities using the bulk atomic density of Ta (0.46×10^{-23} atoms·cm^{-3}) and of Ge (0.43×10^{-23} atoms·cm^{-3}). As discussed in Section 3.1 this is likely to overestimate the density slightly and thus underestimate the layer thicknesses.

3.3 X-Ray Fluorescence

The atomic concentrations in the alloyed multilayers and the single layer alloy were determined by X-Ray Fluorescence (XRF). XRF is a non-destructive technique in which samples are illuminated by an X-Ray source causing them to re-emit X-Rays which are characteristic of the sample composition. The intensities of the various energy peaks in the spectrum are proportional to the concentration of the corresponding elements. In this case the measurements were performed on a Phillips *PW1404/10* wavelength dispersive X-ray Fluorescence spectrometer. Because the penetration depth of the X-Rays into Ta or Ge is much greater than the thickness of the films the results from the XRF analysis can be taken to represent the entire sample rather than just the surface.

Data for each sample consisted of the integrated number of counts under the peaks corresponding to Ta and Ge. To convert this information into the atomic ratios of Ta and Ge required a comparison with data taken from reference sam-

ples of known composition. The reference samples were selected from the best of the pure Ta multilayers for which the atomic density had been accurately determined using RBS (see Section 3.2 above). Once XRF data had been obtained for several reference samples the ratio of integrated count rates was plotted against the known ratio of atomic densities to provide the calibration curve shown in Figure 3.1. It can be seen that the points for all samples lie on a reasonably straight line, demonstrating the consistency of the XRF and RBS methods. The scatter about the curve gives an estimate of the uncertainties involved. Using this curve the ratio of integrated counts in the Ta and Ge peaks of the unknown samples could be converted into the relative atomic concentration. It must be stressed that this provides only the ratio of the atomic densities, not a direct measurement of the atomic density itself.

To calculate the composition in the superconducting alloyed layers allowance must be made for the fact that the measured composition includes the pure Ge insulating layers as well. The composition is determined by multiplying the ratio of atomic concentrations by the ratio of the total Ge and Ta evaporation times according to

$$\frac{N_{Ta}}{N_{Ge}}\frac{T_{Ge}}{T_{Ta}} = \frac{x}{1-x} \tag{3.5}$$

where N_{Ta}/N_{Ge} is the ratio of atomic densities in the sample determined from the XRF results, T_{Ge} and T_{Ta} are the evaporation times of Ge and Ta respectively and x is the atomic fraction of Ta in the superconducting layer. The Ge evaporation time represents the entire evaporation including the deposition of the protective top and bottom Ge layers, whereas the Ta evaporation time includes only the time during which the samples were exposed to both sources (see Chapter 2).

An estimation may be made of the superconducting layer thicknesses if the Ge thickness is taken from either the MBI measurements or the deposition parameters. Where available the RBS measurement of the Ge thickness generally agrees very well with both the MBI results and the intended thickness, so determining the Ge thickness from either of the latter two methods is probably quite accurate. The superconducting layer thickness is then given by

$$d_{Ta_xGe_{1-x}} = d_{Ge}\frac{T_{Ta}}{T_{Ge}}\left[1 + \frac{\rho_{Ta}}{\rho_{Ge}}\left(\frac{x}{1-x}\right)\right] \tag{3.6}$$

where the Ta concentration x has been determined above.

The best estimates for the layer thicknesses and the alloy concentrations are summarised in Table 3.2 along with an indication of the source of the estimate.

For the single layer alloy the thickness was estimated from the evaporation rates measured by the quartz crystal rate monitors during the evaporation.

Sample	d_{Ta} (Å)	$d_{\mathrm{Ta}_x\mathrm{Ge}_{1-x}}$ (Å)	d_{Ge} (Å)	%Ta (x)
29/2G4	17±1†	-	161±9†	100
30/3G4	103±6†	-	138±9†	100
32/2G1	19±1†	-	83±5†	100
33/1G4	25±2†	-	46±2†	100
36/2G1	53±2†	-	51±2†	100
60/3G1	25±2†	-	24±2†	100
60/3G4	25±2†	-	24±2†	100
2/G6	-	670±70§	-	27±2‡
5/G1	-	60±10‡	170±9¶	38±3‡
5/G2	-	60±10‡	170±9¶	38±3‡
6/G2	-	210±40‡	180±10¶	45±3‡
7/G1	-	40±10‡	30±5§	25±2‡

Table 3.2: Best estimates for the individual layer thicknesses and alloy layer composition for each of the samples. A † denotes the data is from RBS, a ‡ denotes XRF data, a ¶ denotes MBI data and a § indicates the data is taken from the evaporation parameters.

3.4 Transmission Electron Microscopy

When fabricating the pure Ta multilayers additional samples were deposited onto mylar substrates to be investigated by Transmission Electron Microscopy (TEM). After deposition the mylar substrates were sliced as thinly as possibly with a razor blade and embedded into resin so that they could be microtomed to a suitable thickness for study in the TEM. The resulting sections of the multilayers displayed well defined layering indicating that the deposited films maintain their

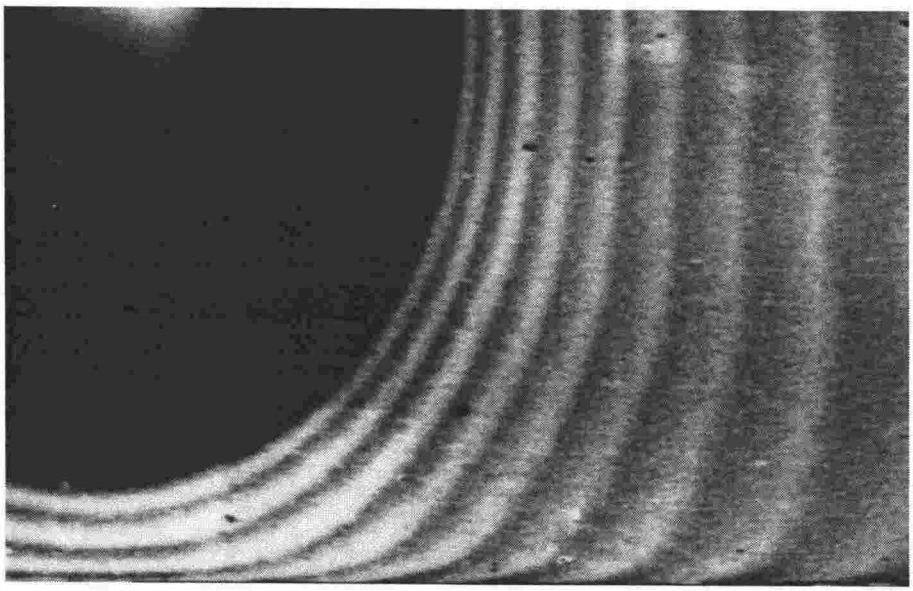

Figure 3.2: An SEM photograph of an ion beam thinned multilayer sample. The individual Ta and Ge layers are clearly visible. The dark rings represent Ge and the lighter rings represent Ta. The large dark region is an area where the film has been completely thinned away. Photograph courtesy of Neil Kemp.

structure. The different layers tended to give different image intensities which made a measurement of the individual layer thicknesses difficult, but the overall thickness of several layer pairs agreed well with the results quoted above.

Electron diffraction patterns showed no evidence of any crystallinity, indicating that both the superconducting and insulating layers are amorphous in nature. This is in agreement with the Raman spectroscopy results of Kumar and Trodahl [45] who saw only broad phonon peaks in several multilayer samples characteristic of an amorphous structure. In Chapter 6 it will be shown that the resistivities of all of the samples used in this study are of the order of several hundred $\mu\Omega$-cm, once again implying a very high degree of disorder. Further discussion of TEM results as well as TEM images corresponding to samples 30/3G4 and 32/2G1 have been given by Johnson [17,36].

3.5 Ion Beam Thinning

Another method which was successfully used to verify the layered structure of the multilayer samples was ion beam thinning. In this technique the samples were placed in an ion beam thinner which bombarded the centre of the film with Ar ions for a period of several hours. This caused a large pit (≈ 5 mm radius) to be etched away from the surface extending downwards throughout most or all of the film and thus exposing the layered structure. Because the edges of the pit

were at such a shallow angle the individual layers could be imaged using either optical or electron microscopy. Figure 3.2 shows a typical image from a pure Ta multilayer sample taken with a Scanning Electron Microscope (SEM). For this sample the Ta layer thickness was 77Å and the Ge layer thickness was 95Å (the transport properties of this sample were not investigated in this study). The individual layers are quite sharply defined despite the finite penetration depth of the electrons, indicating that there is little mixing at the interface. This is in agreement with the results of a previous investigation of the superconducting proximity effect in pure Ta/Ge multilayers in which the interface mixing was estimated to cover a distance of less than 10Å [40]. The layers also appear to be highly uniform, but unfortunately it was not possible to measure the actual layer thicknesses with this method because the exact shape of the pit was unknown. The thinning rate of the two materials is likely to be quite different so the actual profile of the pit will not be smooth but instead will be steepest in the preferentially thinned layer, thus distorting the apparent thickness.

3.6 Summary

A range of techniques have been used to characterise the samples used in this study. These have enabled an accurate determination of the individual layer thicknesses as well as confirming the stability of the layered structure. TEM results along with Raman spectroscopy show no signs of crystallinity in either of the layers.

Chapter 4

Experimental Details

The superconducting properties of the multilayers and alloys have been investigated by measuring their resistive transport properties in an applied magnetic field. For all samples T_c was less than 3 K necessitating measurement below liquid helium temperatures. $H_{c2}(T = 0)$ varied from less than 3 Tesla with the field perpendicular to the thinnest superconducting layers to greater than 15 Tesla when the field was oriented parallel to the thickest Ge layers. In order to achieve these experimental conditions four different cryogenic systems have been used. Details of the four different systems and the experimental techniques are given below.

4.1 Resistive Transport Measurement

Each of the samples investigated was deposited on a glass substrate of 13 or 18 mm diameter and patterned into the four-point geometry using a scriber, as described in Ref. [17]. The current paths thus created were large (typically 1 mm wide by 5 mm long) compared to the relevant superconducting lengths thereby avoiding effects due to the sample edges. Contact was made to the samples by way of pressed indium pads which were attached on top of scratches in the films ensuring contact to each of the individual layers. The contact resistance of these connections was estimated to be of the order of 1 Ω. Even at the highest currents used there was no evidence of the effects of heating of the contacts.

Depending on the system in use either AC or DC techniques were employed to perform the measurements. While lock-in techniques on AC signals generally give lower noise levels, it is shown in Sections 4.5 and 4.6 below that very low noise level measurements can also be made using conventional DC techniques if careful attention is paid to the design of the measurement apparatus. In either

case the measurement results should be equivalent due to the low AC frequencies used.

4.2 Sample Selection

In order to draw reasonable conclusions about the role of the layers in determining the superconducting properties it is necessary to use only the best samples. For the investigation it was desired that both the superconducting and the insulating layer thicknesses be varied. Thus several different samples were needed, each of which had to be uniform within the layer plane and have no variation between the different superconducting or insulating layers.

Initial sample selection was based upon the evaporation parameters which determined the layer thicknesses. When more than one sample was available in the desired thickness range preference was given to the sample with the best evaporation conditions e.g. the lowest evaporation pressure, the most layers etc. For details on the evaporation procedure see Chapter 2. In a similar manner the sample characterisation was also taken into account when selecting samples i.e. samples were chosen where the available characterisation indicated that the desired layer thicknesses had been achieved, and no problems had occurred during the film growth. Details of the sample characterisation are given in Chapter 3.

In addition to this the resistive transitions of the samples with T_c above 1.3 K were measured in zero field as described in Section 4.3, and the best samples selected for further measurement. In this case the best samples were taken to be those that showed smooth, stepless transitions indicating minimal variation in the layer thickness and composition across the sample. However measurements were also made on samples with T_c below the lowest temperature achievable in the glass cryostat. In some of these cases the superconducting transition had been measured in zero field using a ^{3}He refrigerator [17, 40] and where available these data were used to select samples for further measurement in the same way that the transitions measured in the glass cryostat were used to select the samples with higher T_c.

4.3 Glass ^{4}He Cryostat

As a first step towards obtaining a complete set of experimental data the resistive transitions of the samples with T_c above 1.3 K were measured in a glass cryostat in the absence of any applied magnetic field. This system had the advantage

of being able to accommodate three samples at once so that the quality of the superconducting transition could be examined for a larger number of samples and the best ones selected for further measurement. This system has been described extensively elsewhere [17] so only the main features are reproduced here.

The apparatus consisted of a double walled glass cryostat with an outer liquid nitrogen jacket (77 K) and an inner liquid helium jacket surrounding the stainless steel sample space. The liquid helium jacket was attached to a helium recovery system as well as a single stage Edwards rotary pump which was used to lower the temperature of the helium bath below 4.2 K. Up to three samples could be placed inside the vacuum tight stainless steel sample space which was coupled to the helium bath via helium exchange gas. To promote temperature stability the samples were secured to a large copper block and shielded by a copper can. The basic operating procedure was to pre-cool the system to near liquid nitrogen temperatures and then transfer the liquid helium to bring the samples to 4.2 K. The liquid helium was then pumped and data was taken both as the samples cooled to approximately 1.3 K and also as the samples warmed up again. The cooling rate was adjusted by varying the pumping speed through a valve and was maintained at a rate that gave a dense data set around the superconducting transition. Typical cooling rates below 4.2 K were 20 mK/min. This rate also ensured that the samples and thermometer all remained in thermal equilibrium.

The temperature was measured using a 20 Ω rhodium-0.5% iron thermometer calibrated by Cryogenic Calibrations Ltd. The overall temperature measurement was accurate to within ±3 mK for temperatures between 1.3 and 4 K. Complete details of the temperature measurement process including the calibration are contained in [17].

The resistance was determined by passing a current through each of the samples in series and measuring the corresponding voltages. The current was measured by passing it through a standard 1000 Ω resistor and was typically 100 μA. In some cases this was in the non-linear current region of the samples meaning that the low temperature end of the resistive transition was affected by the finite current (see Chapter 6), but nevertheless it provided a reasonable determination of the quality of the transitions. The voltages were measured with either a Keithley 181 digital nanovoltmeter, a Keithley 195A digital multimeter or a Keithley 196 System DMM. The overall precision of the resistance measurement was better than 1 part in 10^5, and the absolute accuracy better than 75 parts in 10^6 [17]. All data were recorded automatically by computer.

This system was adequate for initial measurements on the samples and for investigating their normal state properties. However as the glass cryostat was

not equipped with a magnet it was neccessary to use different systems to study the vortex state of the samples. The three systems used to do this are detailed in Sections 4.4, 4.5 and 4.6 below.

4.4 Dilution Refrigerator

A dilution refrigerator was used to measure the superconducting properties of the samples with T_c below 1.3 K, and also to measure the low temperature part of the magnetic phase diagram for some of the samples with T_c above 1.3 K. The dilution refrigerator was made by Oxford Instruments and owned by the National Pulsed Magnet Laboratory at the University of New South Wales in Sydney, Australia. This type of dilution refrigerator is capable of reaching temperatures below 20 mK, but for these experiments it was not used below 50 mK. The system also included an 18 Tesla superconducting solenoid powered by a Cryomagnetics Inc. power supply providing a high uniformity over the sample volume. The operation of the dilution refrigerator relies on the heat absorbed during the transfer of ^{3}He from a bath of pure ^{3}He into a mixture of ^{3}He/^{4}He where the ratio of the two species in the mixture remains a constant at equilibrium. The transfer is forced by pumping ^{3}He away from the mixture thereby tending to upset the constant ratio. To begin the experiments the refrigerator unit was inserted into the cryostat containing the magnet and left to cool to 4.2 K before the ^{3}He/^{4}He mixture was allowed to circulate. With the mixture circulating inside the refrigeration unit cooling rapidly took place to temperatures below 1 K. Thereafter the temperature could be varied by controlling the amount of heat applied to the mixing chamber where the ^{3}He/^{4}He mixture resides.

The samples were mounted at the end of a cold finger attached to the refrigeration unit which sat in the centre of the magnet bore. The attachment was made using blocks of non-magnetic plastic in such a way that two samples could be mounted with the layers parallel to the field or one sample mounted with the layers perpendicular to the field. The Lakeshore RuO_2 thermometer was also mounted on the cold finger close to the sample(s) to ensure an accurate measurement of the temperature at the sample(s). A set of shielded measurement leads ran from the sample(s) and the thermometer to a junction box outside the refrigeration unit, and BNC cables were used to connect this to the measurement equipment.

4.4.1 Measurements

Three types of measurement were performed in the dilution refrigerator. These were:

1. Temperature sweeps at constant field and current with AC measurement.
2. Field sweeps at constant temperature and current with AC measurement.
3. DC current sweeps (IV) at constant field and temperature.

Data was acquired using an IBM-PC computer equipped with an IEEE-488 interface. This recorded the voltage across either the two samples or across one sample and the thermometer as a function of time.

Temperature sweeps were performed by setting the field and recording the temperature and resistance of the sample(s) at regular intervals as the temperature was varied. Data were recorded with the temperature being swept both upwards and downwards. The temperature was swept downwards simply by increasing the circulation rate of the ^{3}He/^{4}He mixture in the refrigerator to increase the cooling power. Upward temperature sweeps were generally performed by gradually increasing the amount of power supplied to a heater on the mixing chamber, but at high temperatures it was sometimes neccessary to turn off the circulation of the mixture to reach the desired temperatures. Care was taken to avoid excessively large heating or cooling rates as these could lead to thermal lag between the sample and the thermometer. If two samples were being measured the resistance of the thermometer had to be recorded manually due to limited computer automation.

Field sweeps were performed in a similar manner to the temperature sweeps in that the field and resistance of the sample(s) were measured at regular intervals. Because the power supply to the magnet could be swept at a uniform preset rate the field could be determined accurately from the computer measurement of the time as long as the start of the sweep and the start of the data acquisition were synchronised. This meant a separate measurement of the field was not required. The temperature was held constant during field sweeps by fixing the amount of heating on the mixing chamber and then waiting for the entire system to reach thermal equilibrium. Typically the temperature varied by less than 20 mK during the course of each field sweep.

For both temperature and field sweeps the sample voltage(s) and the thermometer voltage were measured using one of two Stanford Research Instruments SR 830 lock-in amplifiers (with IEEE capability) or a Princeton Applied Research 5210 lock-in amplifier (with no IEEE capability). The sample(s) were

biased with a constant AC current of approximately 1μA and the thermometer was biased with an AC current of approximately 10nA provided by one of two purpose built sources. The currents were determined accurately using a standard resistor and the lock-in amplifiers. This was done at the start of each day and at the end of each day and the drift was found to be negligible. Very low frequencies were used (typically either 13, 23 or 31 Hz), selected to avoid any pickup from the 50 Hz mains supply. The resulting uncertainty in the determination of the sample resistance was about $\pm 0.03\,\Omega$ in typical resistances up to $400\,\Omega$.

The thermometer manufacturer provided a detailed set of measurements of the thermometer resistance versus temperature calibrated against a known standard. This calibration curve was fitted with a cubic spline which was then used to determine the temperature from the thermometer resistances recorded in the data files. The resulting temperature measurement was accurate to within about 5 mK as long as the whole system was in thermal equilibrium.

A slightly different experimental setup was used to perform the IV sweeps. The IV measurements were performed on the samples individually by setting the field and temperature to constant values as described above, and then measuring the sample voltage as the current was swept. The temperature stability was similar to that in the field sweeps. The current was supplied by a Hioki 7051 programmable current amplifier which was driven through a constant high resistance load (typically about $10\,\mathrm{k}\Omega$) and then through the sample. The voltage across the constant resistance was measured with a Fluke 8842A voltmeter to give the total sample current, and the sample voltage was measured with a separate Fluke 8842A voltmeter with an amplifier set to $5000\times$ gain connected across the front inputs. The amplifier also acted to filter some of the AC noise from the signal. The resulting noise level on the voltage measurement was about 500 nV as determined from the point where the IV curves emerge from the background. It was noted that there was some heating of the sample space when large currents were applied to the samples, a feature which should be kept in mind when examining the experimental data.

The dilution refrigerator proved to be an excellent system for making measurements at extremely high fields and low temperatures using small applied currents. This allowed mapping of the entire magnetic phase diagram of the samples. Some difficulties arose when applying large currents to the samples due to heating effects, and also when trying to maintain long term temperature stability. To overcome these problems two other systems were employed operating at temperatures above 1 K as described below.

4.5 MD4 ^{4}He Cryostat With Electromagnet

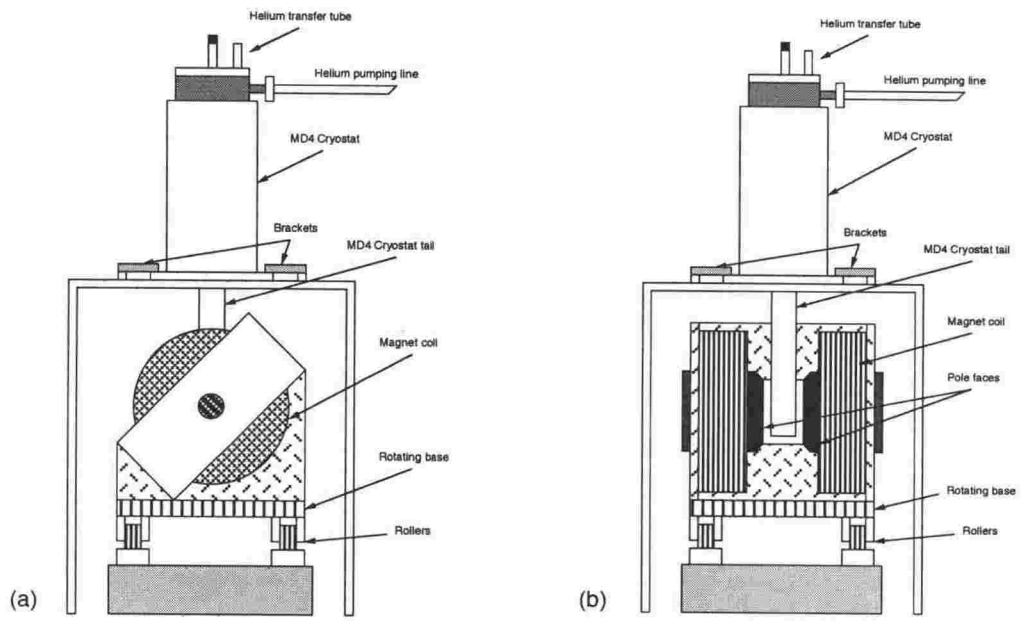

Figure 4.1: Schematic views of the Oxford Instruments MD4 cryostat with the tail inserted into the electromagnet. (a) The magnetic field directed along the rails of the magnet track. (b) The magnetic field rotated through 90°.

To make precise measurements of the resistive characteristics of the samples at temperatures above 1.3 K and in fields of up to 1 Tesla an Oxford Instruments MD4 cryostat was fitted with a 40 cm long tail suitable for mounting into an external electromagnet (see Figure 4.1). The tail had an inner diameter of approximately 18 mm which allowed the insertion of a sample holder capable of accommodating one 13 mm sample. This tail was suspended in an ANAC Model 3473 6 inch water cooled electromagnet with tapered pole caps of 150 mm maximum diameter and 100 mm minimum diameter. The separation of the pole faces with the cryostat tail inserted was about 40 mm which allowed a maximum field of approximately 1.1 Tesla and a stability of the order of a few Gauss over a period of half an hour. The field was controlled by a 2 kW, 50 A Redfern power supply in a feedback loop with a Group III Technology hall effect teslameter which was mounted between the pole faces. The magnet was mounted on a rotating base with 360° capability allowing the magnetic field to be aligned parallel or perpendicular to the layers with a resolution in field angle of less than 0.5°.

The MD4 Cryostat has a common vacuum jacket for both the liquid nitrogen and liquid helium which was pumped out to about 2×10^{-2} torr prior to use. Liquid helium was added to the system using a similar method to that described in Section 4.3 above. The liquid helium was pumped through three different

sized valves in parallel, with each valve providing a different level of control over the pumping speed. The base temperature was about about 1.3 K. The liquid helium capacity of the cryostat was 2.8 litres which lasted for about 18 hours under experimental conditions.

4.5.1 Sample Holder

A sample holder was designed specifically for use in the MD4 Cryostat with the tail. Several characteristics were desired of the insert, namely low noise on the voltage measurements of the sample and thermometer, good thermal stability and high thermal conductivity between the sample and the heat sink for temperatures below 4.2 K.

A schematic view of the sample holder is shown in Figure 4.2. Of note is the lack of a vacuum can around the sample. This means that the sample was immersed directly in the liquid helium bath which has several advantages for measurement below 4.2 K. Direct immersion significantly increases the heat transport away from the sample, a factor which is important at high measurement currents. The soldered contacts connecting the sample leads to the voltage leads on the sample holder were also immersed in liquid helium, thereby minimising any thermal noise in the measured voltage. In a further attempt to minimise the voltage noise in the system the twisted pairs of copper voltage leads from the sample and thermometer were made continuous from the soldered contact in the liquid helium to the front of the measurement instruments. This was achieved by passing each of the leads out of the cryostat through a sealed thermocouple feed-through. Contacts were made to the input of the voltmeters using copper clips attached to a small piece of copper foil folded around the ends of the wires. Thus all of the connections outside of the liquid helium were mechanical connections from copper to copper, eliminating the large thermal voltages which may occur at soldered contacts.

To improve the temperature stability the sample was attached to a copper block, although the helium bath provided the main thermal reservoir to absorb variations in the sample temperature. Two radiation baffles were added and the stem was made of thin walled stainless steel tube to reduce heat leakage into the helium space. A Lakeshore carbon-glass thermometer (CGR-1-1000, serial number C16322) was inserted into the copper block directly behind the sample, and secured with Ge 7031 varnish to provide good thermal coupling between the sample and the thermometer. This type was chosen as carbon-glass thermometers have very little magnetoresistance making them ideal for use in a magnetic field.

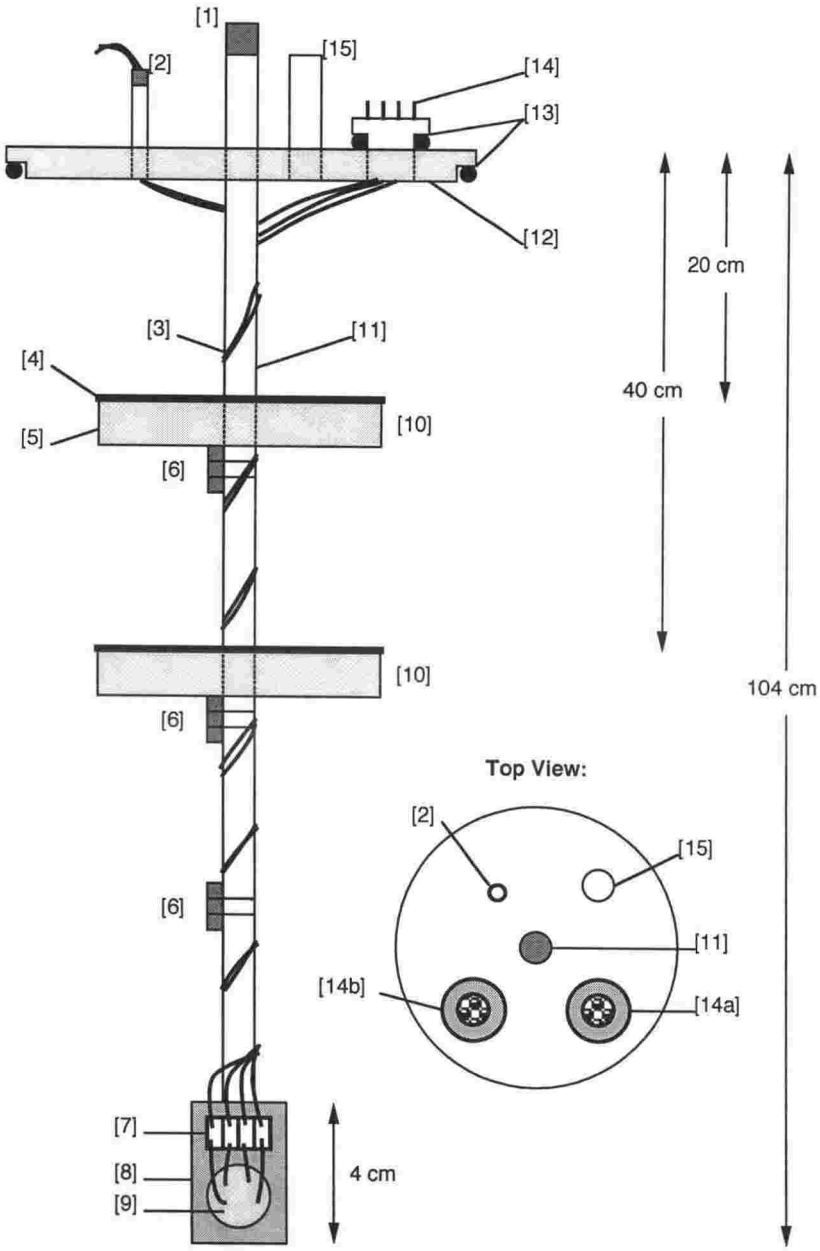

Figure 4.2: The sample holder used with the MD4 cryostat. [1] Rubber stopper; [2] 4 pin continuous feed-through for voltage leads; [3] Twisted pairs of copper wires; [4] Copper plate; [5] Polystyrene; [6] Level sensors; [7] Solder contact pads; [8] Copper block; [9] Sample; [10] Baffles; [11] Stainless steel stem; [12] Brass top; [13] O-ring seals; [14a] 10 pin feed-through for sample and thermometer currents; [14b] 10 pin feed-through for level sensors; [15] Helium fill port.

The pressure above the liquid helium was also monitored during the experiments to provide an auxilliary temperature estimate.

The sample holder was also equipped with level sensors to measure the level of the liquid helium during filling and throughout the duration of the experiment. These consisted of three 680 Ω carbon resistors attached at regular intervals down the stem. The resistance of these sensors was monitored and was found to rise to around 20 kΩ at 4.2 K and remained stable as long as the sensor was below the liquid level. The resistance decreased rapidly as the sensor came out of the liquid enabling the approximate level of the helium to be gauged.

4.5.2 Measurements

Three basic types of DC resistance measurements were performed using this experimental setup:

1. Temperature sweeps at constant field and current.

2. Field sweeps at constant temperature and current.

3. Current sweeps (IV) at constant field and temperature.

Software was written in Borland Turbo Pascal© to provide computer control over each of these types of measurements. The software covered the setup of the various meters including integration times and signal averaging, the reading of the meters, calibration of the temperature data, conversion of the sample voltages to resistance and storing of the data for future analysis. In all cases measurements were made with the sample current in both the forward and reverse direction and the average taken to remove any thermal voltages in the system.

Temperature sweeps were performed by simply ramping the temperature up or down and recording the temperature and resistance of the sample at constant time intervals. By controlling the pumping speed through the valves the temperature was ramped at a rate that ensured a dense data set was obtained with the system in good thermal equilibrium throughout. Before beginning the sweep it was necessary to set the sample measurement current, the field and the delay time between readings (usually zero so that as much data as possible was collected). A measurement of the field was also made after every ten resistance measurements. Due to the low noise levels in the voltage signal it was possible to obtain data using a DC current of only 1 μA which is well below the non-linear IV region of these samples.

Field sweeps were performed using a purpose built sweep unit to sweep the magnetic field up or down while measurements of the field and sample resistance were made. The field sweep rate and the start and finish field values were set on the sweep unit. During the sweep the temperature was measured after every ten resistance measurements and had to be adjusted with the valves if it began to drift. Once again the sample current and delay time between readings were set prior to beginning the sweep.

Performing a current sweep required setting and maintaining the temperature and field while the current was ramped either up or down and the sample voltage measured. The temperature and field were measured after every ten current steps and if necessary the sweep could be paused while the temperature was stabilised. The current was increased geometrically (giving constant spacing between measurements on a logarithmic plot of current) at a predefined rate. The current sweep direction could be reversed during the sweep if desired and a user defined delay between steps could also be used.

The carbon glass thermometer had a resistance of 826 Ω at 4.2 K, and a resistance of about 600 kΩ at 1.3 K. To avoid self heating at low temperatures the measurement had to be performed at low current which was achieved by placing the thermometer in parallel with a smaller shunt resistance. The thermometer current (delivered by a constant current supply) was then measured using a Keithley 195A Digital Multimeter, and the thermometer voltage measured using a Hewlett Packard 3478A Multimeter to give the thermometer resistance. To check for self heating the thermometer was placed in liquid helium and then successively lower currents (determined by the shunt resistance) were used until the measured resistance reached an asymptotic value indicating that no heating was taking place. Thus an upper limit was placed on the power level to be used in the temperature measurement. An advantage of using the shunt resistance was that the thermometer automatically drew more current at higher temperatures which helped to maintain the voltage signal size at measurable levels. The measurement was performed with the current in the forward and reverse directions and an average taken to remove any thermal voltages. The calibration was supplied with the thermometer by Lakeshore in the form of four polynomials covering the range from room temperature to below 1.3 K. Overall the temperature was measured with an accuracy of better than ±10 mK, although changes in the temperature of less than 0.5 mK were readily detectable.

The sample current was provided by a Keithley 224 Programmable Current Source which could supply currents from 10 nA to 100 mA with a resolution of 5 nA. The current steps during the sweeps were programmed over the IEEE in-

terface. The sample voltage was measured with a Keithley 182 Digital Voltmeter which is capable of measuring with nanovolt resolution. The front input was wrapped in insulation to prevent temperature fluctuations which give rise to thermal noise.

The ultimate temperature stability and voltage noise levels were determined during the experiments. It was discovered that at temperatures below 2.17 K (the lambda point of liquid helium) the temperature could be held constant to better than ± 1 mK over the course of multiple field or current sweeps. Above 2.17 K the stability was not as good but the temperature was still stable to better than ± 3 mK. The voltage noise level was determined during current sweeps. When the sample voltage is plotted versus current the smooth IV curve emerges from the thermal noise at about 50 nV. This high sensitivity using DC techniques is a result of the careful design of the cryostat insert and allows a complete investigation of the samples in the low current regime.

The magnetic field was measured by reading the Hall effect teslameter over the RS-232 port on the IBM PC computer. The Hall probe attached to the meter was placed as near to the centre of the pole faces as the cryostat would permit. The magnet pole faces have small holes drilled down their axes for the purpose of optical measurements and these holes tend to limit the homogeneity of the field to slightly less than the value of 1 part in 10^3 over the sample volume given for the cylindrical pole faces without holes. It was estimated that the field at the sample could be measured with an overall accuracy of around 5% [46], but the sensitivity was much better at about ± 1 Gauss. The method used to orient the sample with respect to the field is described in Section 6.1.

4.6 ^{4}He Superconducting Magnet System

The system detailed in Section 4.5 was used very successfully to obtain precise data at low fields and high temperatures from the samples with thin insulating layers and T_c above 1.3 K. However for some of the samples with thick insulating layers the upper critical fields parallel to the layers were much higher than the 1.1 Tesla that the electromagnet could provide, even for temperatures above 1.3 K. To perform a similar investigation of these samples it was neccessary to use a superconducting magnet system. The system used was a Janis Research Company 14CNDT *Supervaritemp* cryostat fitted with a fixed Cryomagnetics Inc. NbTi superconducting magnet, belonging to Lewis & Clark College in Portland, Oregon. The main features of the cryostat are shown schematically in Figure 4.3.

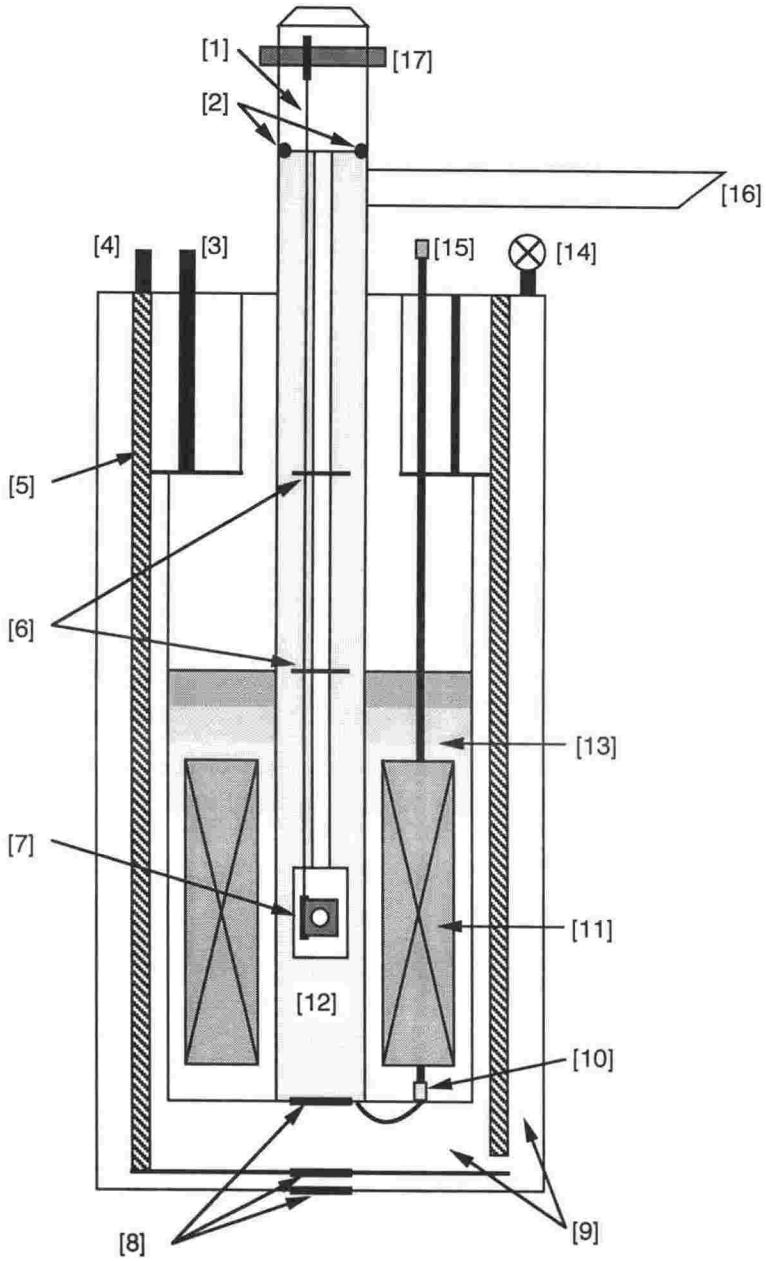

Figure 4.3: A schematic view of the Janis cryostat. [1] Sample rotation cable. [2] O-ring seals. [3] Helium reservoir fill port. [4] Liquid nitrogen fill port. [5] Liquid nitrogen jacket. [6] Radiation shields. [7] Rotating sample holder. [8] Optical windows. These were covered during the experiments. [9] Common vacuum space. [10] Needle valve. [11] Superconducting magnet coils. [12] Sample space. [13] Helium reservoir. [14] Pumping port. [15] Needle valve control. [16] Sample space helium pumping line. [17] Sample rotation axle.

The cryostat had a sample space diameter of 44.45 mm into which the sample holder was lowered, with a maximum achievable field at the centre of the bore equal to 9.3 Tesla and a uniformity of better than 20 ppm over the size of the sample. The field was controlled by a Cryomagnetics Inc. IPS-100 power supply which set the current in the magnet coils. If a constant field was required for a long duration the magnet could be set into a persistent mode where the current continually circulates in the superconducting coils.

To operate the system the vacuum jacket was pumped out to about 4×10^{-2} torr and the sample space and needle valve were flushed with helium gas. After this the magnet space and the nitrogen jacket were filled with liquid nitrogen to precool the system. Once the system had cooled to near 77 K the liquid nitrogen was blown out of the magnet space and liquid helium was added. At this point the sample space containing the sample holder was flushed again with helium gas and then the sample space was filled with liquid helium by fully opening the needle valve between the sample space and the magnet reservoir (see Figure 4.3). Once the sample space was full of liquid helium the needle valve was shut and the temperature was lowered by pumping on the helium through a set of three different sized valves in parallel. Each valve provided a different level of control over the pumping speed and thus over the temperature. A particularly large single stage Kinney rotary pump was used which enabled the system to reach a base temperature of about 1.2 K. The sample space holds about 1 litre of liquid helium which lasted for about 4 hours under experimental conditions, at which point refilling was achieved simply by opening the needle valve again.

4.6.1 Sample Holder

A new sample holder was designed specifically for these measurements, taking into account the same principles applied successfully to the design of the insert for the MD4 Cryostat. Once again the requirements were low noise on the voltage measurements of the sample and thermometer, good thermal stability of the sample and minimal sample heating for temperatures below 4.2 K. As it was not possible to rotate the superconducting magnet it was also required that it be possible to rotate the sample in the magnetic field, thus saving the difficulty of remounting the sample to investigate different field orientations.

Photographs of the sample holder are shown in Figures 4.4 and 4.5. The overall length of the holder is about 1230 mm. The stem of the sample holder was made of thin walled stainless steel tubing and the sample mount and top assembly were machined from brass. The very top of the sample holder was

removable and contained a helium filling port which could be used to fill the sample space should the needle valve to the helium reservoir become blocked. The level of the liquid helium could be gauged by monitoring four carbon resistor level sensors which were evenly spaced down the stem. These sensors worked in an identical fashion to those described in Section 4.5 above. Once again the sample was immersed directly in the liquid helium leading to reduced thermal noise and better thermal stability. To further minimise voltage noise the twisted pairs of copper voltage leads from the sample were continuous from the soldered connection near the sample mount all the way to the input to the measurement instrument. The wires were passed out of the sample space through sealed thermocouple feed-throughs. The connections to the voltmeter were made with copper clips attached to copper foil folded around the wire and were surrounded with insulation to prevent temperature fluctuations. Thus, as above, the only soldered connections were thermally stabilised by immersion in the liquid helium and all other connections were copper to copper, minimising the overall thermal noise in the system.

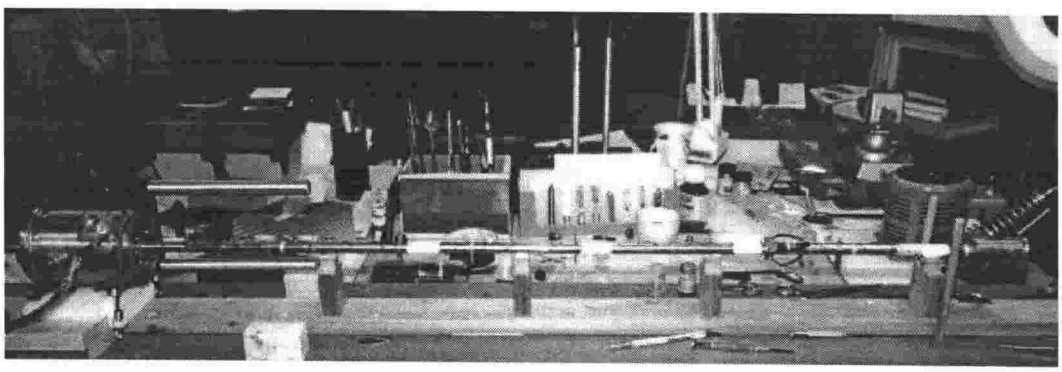

Figure 4.4: The sample holder for the Janis cryostat. At the right hand end is the sample mount while the left hand end holds the rotation assembly and the feed-throughs for the wiring. The total length is about 1230 mm.

The low temperature end of the insert was isolated from the room temperature top end by the low thermal conductivity of the stainless steel stem. Small holes were drilled at regular intervals down the length of the stem to prevent thermal vibrations from being set up in the gas inside the tube. These vibrations must be avoided as they provide an efficient means of energy transfer from the outside into the liquid helium. Further isolation was achieved by wrapping the thin measurement wires around the stem numerous times to increase the thermal path and thermally anchoring them with Ge 7031 varnish. Two heat baffles were attached to the stem to coincide with the levels of the top of the helium and nitrogen spaces in the cryostat. This reduced heat leakage into the helium bath, increasing the lifetime of the liquid helium and promoting thermal stability. The

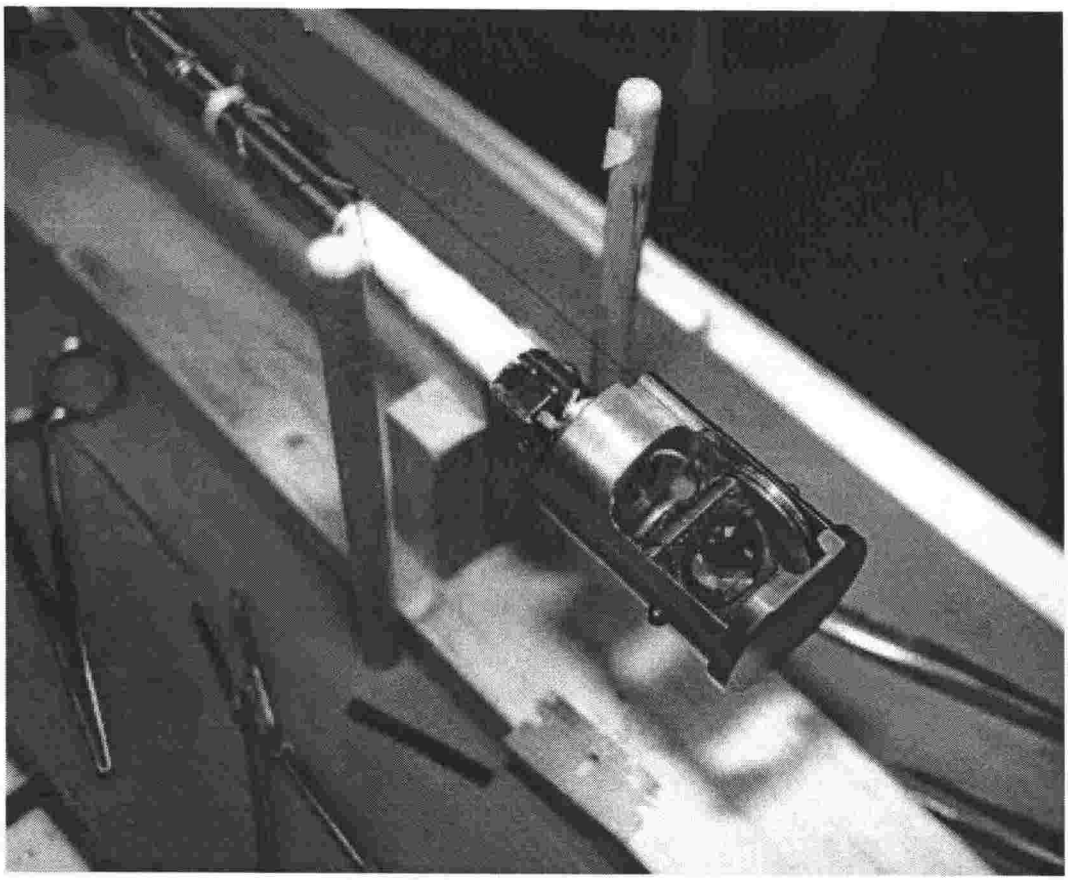

Figure 4.5: A close up view of the bottom end of the insert used with the Janis cryostat. A sample can be seen on the rotating mount.

sample temperature in the helium bath was further stabilised through the use of a large brass block as the sample mount. The Lakeshore carbon-glass thermometer (CGR-250 serial number 11057) was mounted in the back of the block directly behind the sample ensuring thermal equilibrium between the sample and thermometer. This thermometer was specifically chosen for its low resistance (250 Ω at 4.2 K and 56 kΩ at 1.2 K) which lessened the self heating of the thermometer at low temperatures, and for its low magnetoresistance which made it suitable for use in a large magnetic field. As a further means of monitoring the temperature in the cryostat the pressure above the liquid helium was measured during the experiments.

The main difference between this sample holder and the one used with the MD4 cryostat was that for the superconducting magnet system it had to be possible to rotate the sample. The sample rotator can be seen at the left of Figure 4.4. It consists of a cable connecting a pulley wheel on the sample mount (see Figure 4.5) to a pulley wheel attached to an axle which goes through the top of the sample holder. The pulley cable was made of strained stainless steel wire chosen for its low thermal conductivity to reduce heat leakage into the helium

bath. The top axle was rotated with a goniometer which allowed the sample orientation to be adjusted in increments as small as 0.1°. The leads from the sample and the thermometer had to be taken from the rotating sample mount to the main body of the sample holder. Because of the need to avoid stressing or breaking these wires it was only possible to rotate the sample through about 270°, but this proved to be more than adequate for all applications.

4.6.2 Measurements

The software for controlling the measurements was written using LabVIEW® Version IV. Most of the different possible experimental configurations could be selected from within the software, making data acquisition almost fully automatic. Once again the three basic types of experiment were current, temperature and field sweeps. For each of these the sample voltage, field and temperature measurements and the field alignment were the same and will be described first. Other elements, such as setting the current, varied depending on the experiment being performed and will be described separately for each of the three types of experiment.

For each of the experiments the sample voltage was measured using a Keithley 181 Nanovoltmeter. The integration times and signal averaging of the Nanovoltmeter were set by software. The current was supplied by a Keithley 220 *Programmable Current Supply* which provided currents between 1 nA and 100 mA with a resolution of 0.5 nA. To remove thermal offsets the sample voltage was measured with the current in both the forward and reverse directions and the average taken. The overall noise level was about ±30 nV, slightly lower than the corresponding value for the MD4 cryostat, a result of the attention paid to the design of the sample holder. When the magnet was in the non-persistent mode the field could be read remotely by measuring the voltage across two terminals on the back of the power supply which produce a voltage directly proportional to the power supply output current. This voltage was measured with a Keithley 195A *Digital Multimeter* and calibrated by software to give the applied field. The same method was used to orient the sample with respect to the field as in the MD4 cryostat (see Section 6.1 for details).

The temperature was controlled by setting the pumping speed over the liquid helium using three valves in parallel, while the thermometer was read with a DRC 91C Lakeshore Temperature Controller. The temperature controller supplied an AC current to the thermometer and measured the resulting AC voltage using a lock-in amplifier to give the thermometer resistance to a high degree of

accuracy. This resistance was then converted to the temperature using a set of pre-programmed calibration curves (supplied by Lakeshore) stored in the memory of the temperature controller. The low resistance of the CGR-250 and the low AC current ensured that there was no self heating of the thermometer. When performing current or field sweeps the temperature had to be maintained constant over long periods of time. It was found that while the liquid helium bath was kept below the lambda point (2.17 K) the temperature could be held constant to better than ± 1 mK over the course of several sweeps. Above the lambda point the temperature was less stable but the temperature could still be held constant to better than ± 3 mK.

During current sweeps the current was increased in a geometric fashion at a predetermined rate. Both the field and temperature were measured after a set number of current steps. If the temperature drifted the sweep was paused and the temperature monitored both numerically and graphically by the software until the drift had been corrected. This option was typically used at the start of each sweep to determine when the temperature was stable and data collection could begin. The current and voltage were displayed numerically throughout the experiment and the entire data set was displayed graphically on completion of the sweep. A maximum power limit was also set in the software to ensure that the current was turned off if the sample was driven normal to prevent excess heating of the helium bath.

The procedures for doing field and temperature sweeps were very similar. In both cases a constant sample current was set which typically varied between 1 μA, which was in the linear resistance region of the samples, and around 10 mA which placed the samples in the strongly non-linear resistance region (see Chapter 6). The data acquisition could be paused at any stage while the field or temperature were adjusted to the desired value. During field sweeps the temperature was measured after a set number of resistance measurements; similarly during temperature sweeps the field was measured after a set number of resistance measurements to check for any drift. The measured resistance of the sample was displayed on the screen throughout the sweep as well as the most recent temperature and field measurements. On completion of the sweep the entire data set was plotted on the screen.

When performing a temperature sweep the temperature was varied simply by adjusting the pumping speed in order to maintain a relatively constant cooling or heating rate. The cooling rate was generally about 20 mK/min near the superconducting transition which enabled a dense data set to be taken. Using these rates no thermal lag was observed between the downward and upward sweeps

indicating that the sample and thermometer were in good thermal equilibrium. During field sweeps the sweep rate was determined through the controls on the Cryogenics power supply. The sweep rate was also set at a value that ensured a dense data set was obtained around the superconducting transition. Field sweep rates were typically 0.2–0.5 T/min.

4.7 Summary

These four cryogenic systems allowed the superconducting behaviour of the samples to be traced over a wide region of the Field-Temperature-Current phase diagram. Large data sets were obtained for each of the samples which are analysed in the following chapters.

Chapter 5

Theoretical Predictions

Perhaps the most striking thing about the study of superconductivity in layered materials such as high-T_c superconductors and multilayers is the large range of variable parameters. There are several variable sample characteristics such as the critical temperature, coherence length, penetration depth, anisotropy and pinning strength, and several different experimental regimes such as high and low magnetic field, high and low temperature and high and low current. The behaviour is also critically dependent on the orientation of the field with respect to the layers. This leads to a highly complex superconducting phase diagram and a very large associated body of theoretical predictions regarding the nature of the vortex state [6]. This section gives a review of the relevant theoretical models starting with the most simple predictions relating to the form of the upper critical field in layered superconductors and the derivation of some of the characteristic superconducting lengths. From there the melting transition is considered in clean samples in both two and three dimensions. A discussion is given of the transport properties expected both above and below the melting line and finally the expected properties of the vortex state driven by a large applied current are examined.

5.1 Upper Critical Field

Early studies of the properties of thin film and layered superconductors concentrated on the role of the reduced dimensionality in determining T_c [47]. At low temperature there is a competition between the tendency for conduction electrons to form extended pairs in the superconducting state [2] and the tendency for electrons to become localised [47, 48]. In bulk superconductors the pairing mechanism generally dominates and superconductivity is achieved, how-

ever when the dimensionality is reduced the effects of disorder become stronger favouring localisation. This leads to a reduced T_c followed by a crossover from superconducting to insulating behaviour as the film or layer thickness of the superconductor is reduced [47]. However in layered samples with small spacing between the superconducting layers the effect on the dimensionality of reducing the layer thickness is lessened due to the interlayer coupling. This prevents the depression of T_c and the sample is then best described as being either quasi-2D or quasi-3D depending on the exact level of coupling.

An extensive investigation of the dependence of T_c on the layer thicknesses in pure Ta/Ge multilayers has been performed previously [40]. In multilayers with decoupled superconducting layers T_c decreased approximately linearly with the sheet resistance, going to zero when the resistivity approached the quantum resistance $R_Q = h/(2e)^2 \approx 6.45k\Omega/\Box$. For multilayers with thinner insulating layers the interlayer coupling tended to enhance T_c above the value expected for the same superconducting layer thickness in isolation. The exact value of T_c in this system is influenced by an alloyed region of higher T_c which forms at the layer interfaces.

The natural progression of this work on the determination of T_c in layered superconductors is the determination of the upper critical field $H_{c2}(T)$. $H_{c2}(T)$ defines the boundary between the superconducting and normal state on the magnetic phase diagram and thus sets the scale of field and temperature to be considered. The approaches to the determination of H_{c2} considered here are the anisotropic Ginzburg–Landau theory [4] and the Lawrence-Doniach model [49] and also the model of Werthamer, Helfand and Hohenberg [50] which relates the critical field to the microscopic properties of the sample.

5.1.1 Ginzburg–Landau Theory

The Ginzburg–Landau (GL) theory was first developed as a phenomenological model although it was later shown that the GL formulation is in fact a limiting case of the BCS theory [51]. The theory has been employed to explain many aspects of superconductivity, but this section will concentrate on the determination of the upper critical field. In the GL theory the free energy of the superconductor is expanded in terms of a two component order parameter (the magnitude of which can be shown to be proportional to the density of the superconducting condensate) including terms relating to applied fields and to gradients in the order parameter. The expansion is valid only near T_c, so application of the results of the GL theory should be restricted to this range. Minimisation of the free

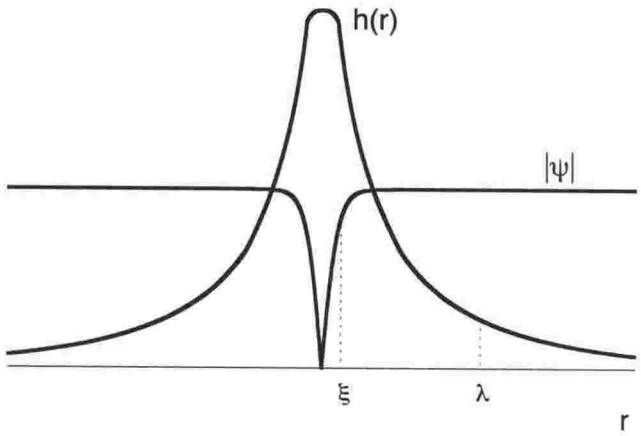

Figure 5.1: Cross section of a single vortex in an isotropic three-dimensional superconductor. There is a core of radius ξ in which the superconductivity is supressed, while the magnetic flux extends out to a radius equal to the penetration depth λ. The vertical axis represents both the magnetic field and the magnitude of the order parameter $|\Psi|$.

energy with respect to the order parameter leads to a set of differential equations which in turn imply a characteristic minimum length scale ξ over which the order parameter can vary. For clean superconductors this Ginzburg–Landau coherence length is given by

$$\xi(T) = \frac{\Phi_0}{2\sqrt{2}\pi B_c(T)\lambda_L(T)} \propto \frac{1}{(1-t)^{1/2}} \tag{5.1}$$

where $t = T/T_c$, $H_c(T)$ is the thermodynamic critical field, $\Phi_0 = 2.07 \times 10^{-15}$ Wb is the magnetic flux quantum and $\lambda_L(T)$ is the London penetration depth which determines the screening length for the magnetic field in the clean limit. In dirty superconductors at temperatures close to T_c the effective coherence length ξ_{eff} is given approximately by $0.855(\xi_0\ell)^{1/2}/(1-t)^{1/2}$ where ℓ is the electronic mean free path and ξ_0 is the Pippard coherence length[1] [2]. In amorphous superconductors, where ℓ is of the order of the atomic spacing, the effective coherence length may be considerably less than the value in the corresponding clean material. Similarly, close to T_c the effective penetration depth λ_{eff} is given by $\lambda_L(T)[\xi_0/1.33\ell]^{1/2}$, which can be considerably greater than the clean limit value. Hereafter references to the penetration depth λ and the coherence length ξ refer to the dirty limit values λ_{eff} and ξ_{eff}. The ratio of the magnetic screening length to the su-

[1]Originally the Pippard coherence length was introduced to describe the size of the smallest electron pair wave functions, but at $T = 0$ the Pippard coherence length is approximately equal to the clean limit GL coherence length $\xi(0)$ (Equation 5.1).

perconducting coherence length $\kappa = \lambda/\xi$ is referred to as the Ginzburg–Landau parameter.

For type-II superconductors where κ is greater than $1/\sqrt{2}$ the GL equations can be used to derive H_{c2}, the highest field at which superconductivity can nucleate[2]. For a bulk isotropic superconductor the expression is

$$H_{c2}(T) = \frac{\Phi_0}{2\pi\xi^2(T)} \propto 1 - t. \tag{5.2}$$

Below H_{c2} the field penetrates the sample in the form of quantised vortices[3] each carrying a unit of magnetic flux equal to Φ_0. Each vortex consists of a core of radius ξ where the superconductivity is supressed, while the field penetrates out to a distance λ from the centre of the vortex (see Figure 5.1). This vortex phase, referred to as the mixed or Schubnikov state, persists down to the lower critical field H_{c1} below which the field is completely screened from the interior of the superconductor. The existence of the mixed state in type-II superconductors is the result of the negative domain wall energy between the normal and superconducting states in the presence of a magnetic field. This makes it energetically advantageous for the field to penetrate the sample in minimum units, thereby maximising the boundary area between the field carrying vortices and the surrounding superconducting region.

By enforcing a periodicity in the known solutions to the GL equations at H_{c2} Abrikosov [52] showed that in the mixed state it is energetically favourable for the vortices to arrange themselves into a regular array known as the Abrikosov lattice. This is essentially the result of the repulsive interaction between the vortices, where the interaction energy has a logarithmic dependence on the intervortex spacing at small distances and crosses over into an exponentially decreasing dependence at large distance [2]. The lowest energy state turns out to be a triangular lattice with the spacing between adjacent vortices given by

$$a_0 = \left(\frac{4}{3}\right)^{1/4} \left(\frac{\Phi_0}{B}\right)^{1/2}. \tag{5.3}$$

It is worth noting that the upper critical field can be interpreted as the point at which the spacing between the vortices is so small that the normal cores of the

[2]For the case where the field is directed parallel to a thin film superconductor there is a solution to the GL equations which yields a higher critical field H_{c3} [2]. This solution is valid only for sharp interfaces and is likely to be destroyed by the diffusion of superconducting electrons into the Ge layers in the Ta_xGe_{1-x}/Ge multilayer system.

[3]The quantisation of the field in the vortices is a result of the requirement that the order parameter be single valued. The phase of the order parameter must therefore change by an integral multiple of 2π after a complete circulation of the vortex which leads to the quantisation.

vortices overlap, meaning that there is no longer a continuous superconducting path through the sample.

The anisotropic Ginzburg–Landau model [2, 48] extends the isotropic GL model to include an effective mass tensor in the free energy formulation. In superconductor/insulator multilayers and in naturally layered superconductors such as the high-T_c cuprates the effective mass tensor captures the anisotropy in the electronic effective mass caused by the non-superconducting layers. This model describes only samples with strongly coupled superconducting layers where the description in terms of a continuous medium with an anisotropic effective mass is valid, but much progress can still be made within this limitation. In this model the coherence length is proportional to $1/\sqrt{m_i}$ where m_i is the effective mass in the ith direction, leading to

$$H_{c2\parallel} = \frac{\Phi_0}{2\pi\xi_{ab}\xi_c} \tag{5.4}$$

and

$$H_{c2\perp} = \frac{\Phi_0}{2\pi\xi_{ab}^2} \tag{5.5}$$

where the subscripts $\parallel$ and $\perp$ refer to the cases where the field is directed parallel or perpendicular to the layers and the subscripts ab and c have been borrowed from the high-T_c notation to represent directions in the layer plane or perpendicular to the layer plane respectively (see Figure 1.1). Typically the out-of-plane coherence length ξ_c decreases considerably below the in-plane value ξ_{ab} as the anisotropy increases. The effective mass anisotropy also introduces anisotropy into the penetration depth. A magnetic field directed perpendicular to the layers is screened by currents flowing in the layer plane, whereas to screen a field directed parallel to the layers the currents must cross the planes in the c direction. The large effective mass in the c direction means that $\lambda_c \gg \lambda_{ab}$. Vortices directed parallel to the planes will be elliptical in shape with the core radius in the c direction (given by ξ_c) smaller than the core radius in the ab direction (given by ξ_{ab}) as shown in Figure 5.2. It can be seen that $H_{c2\parallel}$ must be larger than $H_{c2\perp}$ as the condition that the normal cores overlap will be satisfied at higher fields in the parallel case than in the perpendicular case.

Blatter, Geshkenbein and Larkin [53] have developed a simple method for transforming results from the isotropic GL theory to the anisotropic case which includes the generalisation to arbitrary angles θ between the field and the superconducting planes (see Figure 1.1). This saves the effort of solving each

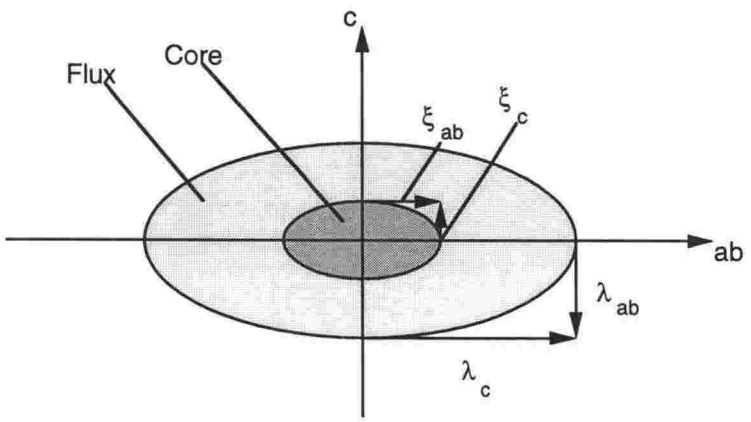

Figure 5.2: A schematic view of a vortex directed parallel to the layers of an anisotropic layered superconductor. See the text for an explanation of the symbols.

anisotropic case separately if the isotropic result is already known. The method is valid when the anisotropic GL theory is valid i.e. when the anisotropy is not too great, with the further requirement that the vortices overlap i.e. $B \gg H_{c1}$. The isotropic parameters $H, T, \xi, \lambda, \gamma$ and f are transformed according to the prescription

$$Q(\theta, H, T, \xi, \lambda, \gamma, f) = s_Q \tilde{Q}(\epsilon_\theta H, \gamma T, \xi, \lambda, \gamma f) \tag{5.6}$$

where Q represents any function of the above variables for which the isotropic result $\tilde{Q}$ is known. The variable f is a measure of the pinning strength (which will be discussed below in Section 5.3.1), $\epsilon_\theta^2 = \gamma^{-2}\cos^2\theta + \sin^2\theta$ and $s_Q = 1/\epsilon_\theta$ for the magnetic field and $s_Q = 1/\gamma$ for all other variables. The values of ξ and λ appearing in the isotropic results can be replaced by the in-plane values ξ_{ab} and λ_{ab} in the anisotropic case. The parameter γ determines the degree of anisotropy and is defined by

$$\gamma \equiv \left(\frac{m_c}{m_{ab}}\right)^{1/2} = \frac{\lambda_c}{\lambda_{ab}} = \frac{\xi_{ab}}{\xi_c} = \frac{H_{c2\|}}{H_{c2\perp}}. \tag{5.7}$$

Application of this method to the isotropic result for H_{c2} (Equation 5.2) using $\xi = \xi_{ab}$ yields the angle-dependent upper critical field for an anisotropic superconductor

$$H_{c2}(\theta) = \frac{1}{\epsilon_\theta}\frac{\Phi_0}{2\pi\xi_{ab}^2} \tag{5.8}$$

$$= \frac{H_{c2\|}}{(\cos^2\theta + \gamma^2\sin^2\theta)^{1/2}} \tag{5.9}$$

where $H_{c2\|}$ is given by Equation 5.4.

The anisotropic GL theory works well only for the case where the anisotropy is not too large. Tinkham [2] has calculated the parallel upper critical field within the ordinary GL framework for the opposite case where the anisotropy is so large that the superconducting layers can be considered as isolated thin films. If the thickness of the isolated superconducting layers $d_s \ll \xi_{ab}$ then the GL equations can be solved to give

$$H_{c2\|} = \frac{\sqrt{12}\Phi_0}{2\pi d_s \xi_{ab}} \propto (1-t)^{1/2}. \tag{5.10}$$

The proportionality to $(1-t)^{1/2}$ is qualitatively different to the $(1-t)$ behaviour found for the perpendicular field case above, demonstrating the importance of the reduced dimensionality. A more complete description of the parallel critical field of strongly layered superconductors can be obtained from the Lawrence-Doniach model described below.

5.1.2 Lawrence-Doniach Model

In strongly layered systems the temperature dependent coherence length may become less than the interplanar distance so that the anisotropic GL theory is no longer valid. In this case the system is better described by the Lawrence-Doniach (LD) model [49]. The formulation of the LD model is similar to the GL theory in that the free energy is expanded in terms of an order parameter, however the individual two-dimensional layers are now treated as discrete entities coupled by Josephson tunneling[4]. Near T_c the LD model returns the same results as the anisotropic GL model in the limit of strong interlayer coupling, but a particular advantage of this model is that its formulation is valid for all temperatures below T_c.

In a similar manner to the GL approach the free energy is minimised to give the Lawrence-Doniach equation which may be solved for a field applied parallel to the layers to give

$$H_{c2\|}(T) = \frac{(\Phi_0/2\pi d_i^2)}{\gamma[1 - d_i^2/2\xi_c^2(T)]^{1/2}} \tag{5.11}$$

where d_i is the spacing between the superconducting layers. This equation for $H_{c2\|}$ diverges at $\xi_c = d_i/\sqrt{2}$ meaning that the sample is then completely trans-

[4]Josephson coupling results from the tunneling of superconducting pairs between the layers in response to differences in the phase of the order parameter. The lowest energy state in this case is where the phase is the same in each layer.

parent to the parallel field, although this divergence would in reality be cut off by Pauli paramagnetism. Furthermore Deutcher and Entin-Wohlman [54] have shown that when the finite thickness of the real layers is taken into account the divergence is removed and the parallel critical field is given in the low field limit ($T \rightarrow T_c$) by

$$H_{c2\|}(T) = \frac{\Phi_0}{2\pi\xi_{ab}\xi_c(d_i + d_s)/d_s} \propto (1-t) \tag{5.12}$$

where once again d_s is the superconducting layer thickness and d_i is the insulating layer thickness. In the strong field limit Equation 5.10 for an isolated thin superconducting slab is recovered. Comparison of Equations 5.10 and 5.12 shows that as the temperature is increased a 2D–3D dimensional crossover should occur signified by a change in the temperature dependence of $H_{c2\|}$ from $(1-t)$ to $(1-t)^{1/2}$. This crossover is expected to occur when the temperature dependent coherence length ξ_c becomes greater than the interlayer spacing d_i, leading to coupling between the superconducting layers. A similar dimensional crossover, but this time from 3D–2D, can occur when ξ_c becomes greater than the total thickness of the sample.

These dimensional crossovers have been investigated in the Nb/Ge multilayer system by Ruggiero *et al.* [18,19] who studied the behaviour of $H_{c2\|}$ as a function of the Ge layer thickness. They observed a change from anisotropic 3D ($H_{c2\|} \propto (1-t)$) to 2D ($H_{c2\|} \propto (1-t)^{1/2}$) behaviour as the Ge layer thickness was increased, with a crossover region at intermediate layer thickness where the behaviour was 3D-like close to T_c and changed to 2D-like at lower temperatures. Similar results showing dimensional crossovers have been obtained on Al/Ge [32] and Nb/Si [33] multilayer systems, demonstrating the validity of the models described above.

5.1.3 Werthamer-Helfand-Hohenberg Theory

A far more detailed approach to the determination of H_{c2} for an isotropic superconductor has been undertaken by Werthamer, Helfand and Hohenberg [50]. They calculate H_{c2} from a much more microscopic point of view and include the effects of material dependent parameters like the finite electron mean free path, Pauli spin paramagnetism and spin-orbit impurity scattering. Their results, which extend the work of several previous authors (most notably Gor'kov [51,55]), are valid at all temperatures and include the Ginzburg–Landau results as a limiting case. At temperatures well below T_c they demonstrate a deviation from the behaviour of H_{c2} predicted by GL theory in an isotropic superconductor,

and instead find that H_{c2} lies below the extrapolated linear behaviour observed near T_c. At zero temperature the actual critical field is predicted to lie below the extrapolated high temperature value by a factor of 0.69. The real value of this model lies in the incorporation of the microscopic properties of the material, and the subsequent ability of the model to correctly predict the low temperature behaviour of H_{c2}.

5.1.4 Summary

The preceeding section has considered the determination of H_{c2} for several different regimes. Most notably a dimensional crossover from 2D to 3D behaviour is expected in layered samples when the perpendicular coherence length becomes greater than the interlayer spacing. A similar crossover from 3D to 2D behaviour may occur close to T_c in thin samples when the perpendicular coherence length becomes greater than the total thickness of the sample.

5.2 Thermal Fluctuations and Vortex Lattice Melting

All of the theoretical models of the upper critical field discussed above predict an exact position of the thermodynamic phase transition which occurs at H_{c2}. Based on these models there should be a well defined boundary between the normal state and the superconducting mixed state at the transition point, however for any system at finite temperature thermal fluctuations allow the system to sample configurations away from the lowest energy state. Fluctuations in the electronic degrees of freedom (or equivalently fluctuations in the magnitude of the GL order parameter) lead to some superconducting pair formation at temperatures[5] above $T_{c2}(H)$ and some pair breaking below $T_{c2}(H)$. Below $T_{c2}(H)$ where type-II superconductors enter the mixed state the vortices themselves (or equivalently the phase of the order parameter) are the thermodynamic objects subject to thermal fluctuations. In either case the minimum fluctuation energy is determined by the coherence length (which sets the minimum size of the fluctuation volume) which means that fluctuation effects are more noticeable in strongly type-II materials like high-T_c superconductors and amorphous multilayers where the coherence length is small. In layered materials the two-dimensional nature serves to enhance

[5] $T_{c2}(H)$ is used here to represent the superconducting transition temperature in an applied field H.

the importance of fluctuations even further. The effects of these fluctuations are discussed in the following sections.

5.2.1 Fluctuation Conductivity

One of the first treatments of the effects of thermal fluctuations on the zero field conductivity above T_c was performed by Aslamasov and Larkin [56] who calculated the enhancement of the conductivity above the normal state value caused by fluctuations of the system into the superconducting state. Their results, which can be derived within the Ginzburg–Landau framework by assuming non-interacting Gaussian type fluctuations of the order parameter, depend on the dimensionality of the sample and are given in the isotropic case by

$$\sigma' = \frac{e^2}{16\hbar d_s}\frac{T}{T-T_c} \qquad (2D) \qquad (5.13)$$

$$\sigma' = \frac{e^2}{32\hbar\xi(0)}\left(\frac{T}{T-T_c}\right)^{1/2} \qquad (3D) \qquad (5.14)$$

where the fluctuation conductivity σ' is equal to the difference between the experimentally measured conductivity σ and the normal state conductivity σ_n. The dimensionality here is again defined by the relative sizes of the perpendicular coherence length ξ_c and the superconducting layer thickness d_s. Several corrections to these forms for the fluctuation conductivity have been discovered [57], although these terms are generally of importance only in very clean materials and can be neglected in the amorphous limit.

Recently the theory of the fluctuation conductivity has been extended by Ullah and Dorsey [58, 59] to include the effects of a finite applied magnetic field. They include non-Gaussian fluctuations in their theory and also the possibility of interactions amongst the fluctuations by including in the free energy expression higher order terms in the order parameter. At high fields, where only the lowest Landau levels are occupied, they obtain a scaling relation between the fluctuation conductivity and the applied field and temperature. The scaling forms, which depend on the dimensionality, are given in terms of unknown but universal functions of the field and temperature as

$$\sigma'(H) = \left(\frac{T}{H}\right)^{1/2} F_{2D}\left(a\frac{T-T_c(H)}{(TH)^{1/2}}\right) \qquad (2D) \qquad (5.15)$$

$$\sigma'(H) = \left(\frac{T^2}{H}\right)^{1/3} F_{3D}\left(b\frac{T-T_c(H)}{(TH)^{2/3}}\right) \qquad (3D) \qquad (5.16)$$

where a and b are constants characterising the materials and F_{2D} and F_{3D} are the universal functions. These forms show that if $\sigma'(H/T)^{1/2}$ is plotted against $[T-T_c(H)]/(TH)^{1/3}$ for a two-dimensional sample the data should collapse onto a single curve which represents F_{2D}. Similarly, a plot of $\sigma'(H/T^2)^{1/3}$ versus $[T-T_c(H)]/(TH)^{2/3}$ for a three-dimensional sample should collapse the data onto a single curve representing F_{3D}. Within the Ginzburg–Landau theory the upper critical field perpendicular to the layers is linear in the temperature, and can thus be specified in terms of its intercept $T_c(0)$ and the slope $S = -dH_{c2}/dT|_{T=T_c}$ on the magnetic phase diagram. Using S as a free parameter the scaling behaviour can be optimised to determine the upper critical field $H_{c2}(T)$ from the fluctuation conductivity. This provides a more accurate determination of the upper critical field from resistance measurements than ordinary criteria such as using the midpoint of the transition.

The scaling method has been used to determine H_{c2} for a wide range of samples including $YBa_2Cu_3O_{7-\delta}$ crystals [60] and films [61] which display a three-dimensional scaling, $Tl_2Ba_2CaCu_2O_x$ films [61] which display two-dimensional scaling behaviour and also thin films of a-Nb_3Ge and a-MoGe [62] where the dimensionality depends on the thickness of the films.

It should be noted that fluctuations are not the only possible cause of a rounding off of the superconducting transition. Inhomogeneities can lead to a spatially dependent T_c which will also tend to broaden the transition as some parts of the sample go superconducting at higher temperatures than other parts. However it can been shown [63] that if the variations in T_c are small ($\sim 5\%$) then the effects of the disorder on the fluctuation conductivity will only be noticeable very close to T_c.

5.2.2 Zero Field Berezinskii-Kosterlitz-Thouless Transition

The above discussion concentrated on the role of fluctuations in the density of superconducting pairs in rounding off the resistive transition at $T_{c2}(H)$. For very thin superconductors in the two-dimensional limit or for highly decoupled multilayers with thin superconducting layers there is another type of fluctuation in zero applied magnetic field that actually changes the point at which the transition to zero resistance takes place. The fluctuation in question is the thermal excitation of a vortex-antivortex pair[6] which creates a loop of magnetic flux threading the superconducting layer as shown in Figure 5.3. Because they are opposite in sign these vortex-antivortex pairs experience an attractive interaction with the previously noted logarithmic dependence on the separation for small loop radius. In two dimensions the logarithmic interaction between vortices has been shown [64] to extend out to a distance $\lambda_\perp = \lambda_{ab}^2/d_s$ which is considerably larger than the usual screening length λ which gives the range of the interaction in three dimensions. Due to the logarithmic interaction the vortex-antivortex pairs are bound together at low temperature in a so called Berezinskii phase [65, 66], but Kosterlitz and Thouless [67, 68] have shown that at a critical temperature determined implicitly by

$$T_{BKT} = \frac{\Phi_0^2}{8\pi k_B \mu_0 \lambda_\perp(T_{BKT})} \tag{5.17}$$

the vortex pairs with the greatest separation overcome the attractive interaction and unbind, leaving pairs of free vortices. As the temperature is raised further vortex pairs with smaller and smaller separation unbind and the density of free vortices rises exponentially.

The response of the superconductor to an applied current depends on whether the vortex-antivortex pairs are bound or unbound. The Lorentz force is directed oppositely on the two vortices, and if they are unbound then they are free to move in opposite directions even when driven by an arbitrarily small current. It will be shown below in Section 5.3 that when vortices move freely under the influence of an applied current a linear resistivity results and superconductivity is destroyed. For $T < T_{BKT}$ the vortices are bound so the net Lorentz force is zero, but the combination of the Lorentz force and the thermal energy can overcome the binding forces between the vortex pairs, thus leaving a finite density of free

[6]These pairs occur as a vortex and an antivortex of the opposite sign thus leaving the magnetisation unchanged. The creation of a single vortex requires much greater energy and is thus insignificant here.

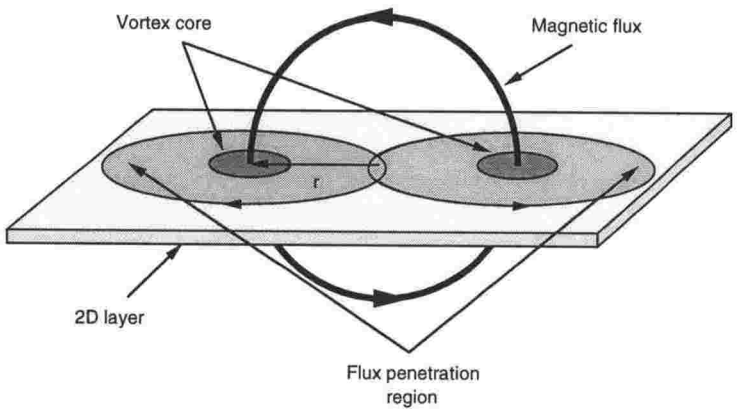

Figure 5.3: A thermally created vortex-antivortex pair bound together to form a vortex loop of radius r threading through the superconducting layer.

vortices. The rate at which this occurs is proportional to $\exp(-U/k_BT)$, where the activation energy U decreases with the separation between the vortex pairs and also decreases as the current is increased. This leads to a power law form for the current-voltage (IV) characteristic

$$V \propto I^{\alpha} \tag{5.18}$$

where the value of α is equal to 3 at T_{BKT}. For $T \gtrsim T_{BKT}$ there is a small but finite density of unbound vortex-antivortex pairs. At low currents the motion of these free vortices leads to a linear resistance ($\alpha = 1$ in Equation 5.18), which crosses over into a power law form again at high currents where the current assisted thermally activated unbinding process becomes the main contributor to the density of free vortices. As the temperature is raised further above T_{BKT} the density of unbound vortices rises and the linear IV characteristic dominates to higher currents. The BKT transition occurs at a temperature which can be well below the mean field transition temperature T_c, so even in zero field a two-dimensional superconductor will show a linear low current resistance below T_c.

In the purely 2D case considered above screening of the logarithmic potential at long length scales changes the interaction between the vortex-antivortex pairs into a much weaker form, leading to the unbinding of the most widely separated vortex-antivortex pairs at all temperatures [6]. This results in a linear resistance at the lowest currents even for temperatures below T_{BKT}. The situation is modified somewhat in layered superconductors with a finite degree of coupling. When the magnetic coupling between the layers is added the interlayer interaction prevents the screening and causes the attraction between the vortices to remain logarithmic at all length scales, so a true BKT transition is restored [6,69]. When the effect of Josephson coupling between the layers is also added the picture is

more complicated. The Josephson coupling further modifies the interaction between the vortices and instead of the BKT transition there is a three-dimensional bulk transition into a true superconducting state at a temperature intermediate between T_c and T_{BKT} [6,69].

Several experimental studies of the zero field BKT transition have been performed on both thin film and layered superconductors. BKT transitions have been observed in Hg-Xe alloy films by Kadin *et al.* [70], and also in In/In-O films by Fiory *et al.* [71]. More recently Norton and Lowndes [28] have measured the resistive transition and IV characteristics of very thin layers of $YBa_2Cu_3O_{7-\delta}$ and also multilayer structures of $YBa_2Cu_3O_{7-\delta}$ with insulating $Pr_{0.5}Ca_{0.5}Ba_2Cu_3O_{7-\delta}$. For the single layers they find good agreement with the BKT transition theory. For the multilayers they observe a deviation from the BKT theory at a temperature above the expected T_{BKT} for a single layer of the same thickness. The temperature where the deviation sets in depends on the insulating layer thickness, demonstrating the importance of the interlayer coupling. Studies of a similar system have been performed by Vadlamannati *et al.* [29] who also find evidence for the existence of the BKT transition in decoupled multilayers. They find that the parameter $(T_c - T_{BKT})/T_c$ takes on values as high as 0.17 in the most two-dimensional samples. Finally, evidence for a BKT transition in a bulk single crystal of the highly anisotropic high-T_c superconductor $Bi_2Sr_2CaCu_2O_8$ has been observed by Martin *et al.* [72] where the BKT transition occurs in each individual superconducting CuO_2 plane. These results demonstrate the applicability of the BKT theory to layered superconductors.

5.2.3 Vortex Lattice Melting

The importance of the zero field fluctuation effects discussed above on the superconducting transition have been appreciated for a considerable length of time. More recently, especially with the discovery of the high-T_c superconductors, the effects of thermal fluctuations well below H_{c2} have also been considered where the fluctuations involve the vortices moving about their equilibrium lattice positions. As mentioned above, if the fluctuations in position of the vortices are large enough then the vortex lattice may actually melt into a vortex liquid with no translational order. In this section the vortex lattice melting transition is examined in the absence of disorder induced pinning forces. To begin with the field will be assumed to lie along the c-axis perpendicular to the layers while the parallel field case will be considered later.

On general theoretical grounds the melting transition is expected to occur

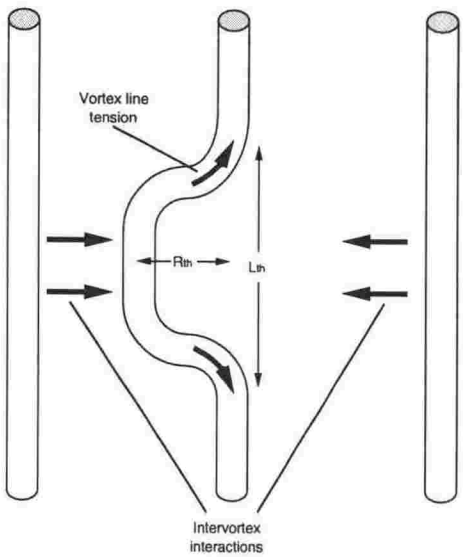

Figure 5.4: A thermally created kink in a vortex line. Both the length of the kinked section L_{th} and the amplitude of the displacement R_{th} depend on the elastic energy of the vortex.

due to the difference in entropy between the highly disordered vortex liquid state and the ordered Abrikosov lattice. The Helmholtz free energy of the vortex configuration is given by $H = U - TS$ where U is the internal energy and S is the entropy of the vortices. At some temperature the liquid state should thus have a lower free energy than the vortex solid and the melting transition will occur. The approach then should be to determine the form of the free energy in both the vortex liquid and solid phases (for example using the Ginzburg–Landau formulation) and then to determine the position of the phase transition, but at this stage a detailed calculation of this type has not been performed. In practice a Lindemann criterion is used to predict the position of the melting line on the magnetic phase diagram by setting the average thermal displacement of the vortices from their equilibrium lattice positions equal to some fraction of the vortex lattice spacing. When the average displacement exceeds this fraction the vortices are assumed to escape from the potential minima at the lattice sites and the vortex solid melts into a liquid.

The average displacement of any given vortex segment from its lattice site is determined by the interplay between the elastic energy and the thermal energy of the vortex. The elastic energy is actually dependent on the configuration of the entire vortex system, a point which will be returned to later in this section, but to begin with it is instructive to use a simple model of vortex thermal motion to estimate the position of the melting transition [2]. Figure 5.4 shows a single vortex containing a thermally induced kink existing in a lattice of unperturbed vortices. In this case there are two contributions to the elastic energy. The first

contribution comes from the line tension of the vortex and tends to favour longer deformations. The tension is equivalent to the free energy per unit length of an isolated vortex and includes contributions from the field, supercurrent and core energies. The second contribution comes from the interaction between the displaced vortex segment and all of the other vortices in the Abrikosov lattice. The intervortex interaction between parallel vortices of the same sign is repulsive and thus tends to favour shorter deformations. By minimising the sum of these two energies the optimal length L_{th} of the kink in the vortex line can be determined, and by then equating the total elastic energy of the kink to the thermal energy k_BT the amplitude R_{th} of the thermally created vortex deformation can be deduced. According to the Lindemann criterion when this amplitude reaches a fraction c_L of the vortex lattice spacing melting takes place. This simple estimate yields for the melting line [2]

$$B_m = \frac{c_L^4 \Phi_0^5}{4\pi^3 \mu_0 (k_B T)^2 \lambda_{ab}^4}. \tag{5.19}$$

Below the melting line the vortex solid can be described in terms of three elastic moduli, the bulk modulus c_{11}, the tilt modulus c_{44}, and the shear modulus c_{66}, which determine the stiffness of the vortex lattice under compression, tilting and shear forces respectively.

The simple model used above considered displacement of only a single section of a single vortex line against the background of a stationary lattice, however in general the modes of vortex motion are similar to phonons in a solid, involving many vortices and multiple fluctuations in each vortex. Each mode of oscillation can be assigned a wavelength, or equivalently a wave vector[7] k. Typical modes of vortex oscillation are shown Figure 5.5. As the different elastic moduli are wavelength dependent, the stiffness of the vortex lattice in response to displacements of the vortices depends on the wavelength of the displacements. It has been shown by Brandt [73] that for superconductors with a large Ginzburg–Landau parameter ($\kappa \approx 200$) a precise treatment of these so called non-local effects leads to a much lower value of c_{66} than that given by the static lattice model used above, or, equivalently, leads to a much softer lattice. The softer lattice enhances the thermally induced displacements of the vortices at all fields which, according to the Lindemann criteria, lowers the melting temperature.

Houghton, Pelcovits and Sudbø [74] have developed these ideas of Brandt to include the anisotropy present in the high-T_c superconductors and in artificial

[7] k is actually split into $k_\parallel$ and $k_\perp$ to describe the tilt modes along the vortex direction and the compressional modes perpendicular to the vortices.

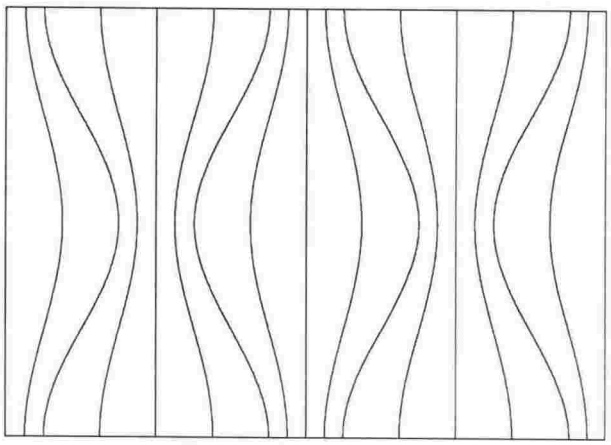

Figure 5.5: An example of thermally induced vortex oscillation modes involving the entire vortex lattice. There is a mode parallel and a mode perpendicular to the field. Figure from Brandt [73].

multilayers. They arrive at a melting line given by

$$[t/(1-t)^{1/2}][b_m(t)^{1/2}/(1-b_m(t))][4(\sqrt{2}-1)/(1-b_m(t))^{1/2}+1] = 2\pi\frac{c_L^2}{G_i^{1/2}} \quad (5.20)$$

where $t = T/T_c$, γ is the anisotropy parameter described above, G_i is the Ginzburg parameter (Equation 1.2) and $b = B/B_{c2} \approx H/H_{c2}$ with the subscript m referring to the value of b at the melting transition. In deriving this result it was assumed that $H_{c2}(T) = H_{c2}(0)(1-t)$ which is equivalent to the Ginzburg–Landau result for an anisotropic superconductor near T_c. Close to T_c where $b_m \ll 1$ the melting line may be approximated by

$$B_m(T) \approx 5.6\frac{c_L^4}{G_i}B_{c2}(0)(1-t)^2. \quad (5.21)$$

At higher fields the temperature dependence weakens and the melting line is approximately parallel to the upper critical field line. As the anisotropic GL result is only valid for moderate (or zero) anisotropy Equation 5.20 for the melting line does not apply to very strongly layered systems, but nevertheless this form for the melting line is a considerable improvement on the simple derivation involving a single kink.

5.2.4 Berezinski-Kosterlitz-Thouless Melting

So far the discussion of the vortex lattice melting transition has focussed on the three-dimensional regime where the vortices behave as elastic line objects for which thermal fluctuations allow bending of the vortex over a part of the total

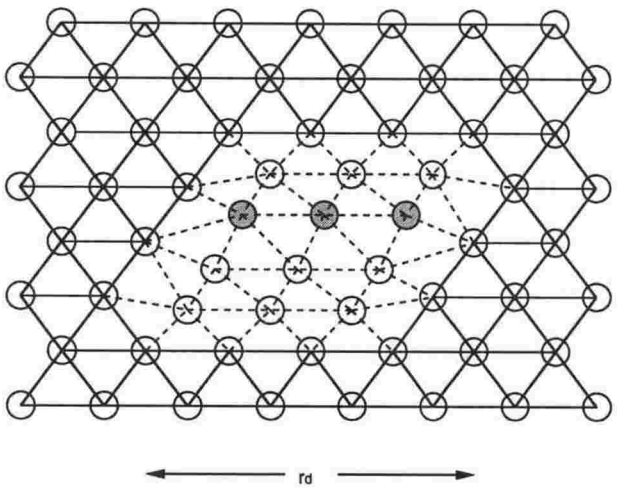

Figure 5.6: A dislocation-antidislocation pair of separation r_d in a two-dimensional vortex lattice. The dislocation-antidislocation pairs consist of two dislocations with oppositely directed Burgers vectors [76]. The dashed lines connect displaced vortices, while the coloured vortices represent the extra flux added to the lattice by the dislocation-antidislocation pair.

length. The model of Houghton *et al.* includes the effects of anisotropy, but is not applicable when the anisotropy is very strong. In the case where the anisotropy is so strong that the individual superconducting layers can be considered as isolated 2D superconductors the melting transition can be better described in terms of a Berezinskii-Kosterlitz-Thouless transition involving the unbinding of thermally created dislocation-antidislocation pairs in the two-dimensional vortex lattice [65–68, 75].

Thermal fluctuations in a two-dimensional vortex lattice can lead to the formation of dislocation-antidislocation pairs[8] as shown in Figure 5.6. In a layer of thickness d_s the interaction energy between these pairs of defects is attractive with a logarithmic dependence on the separation r given by [69]

$$\epsilon_d(r) = \frac{c_{66} d_s a_0^2}{\pi} \ln(r/a_0). \tag{5.22}$$

The interaction comes from the elastic energy due to the deformation of the lattice by the dislocations. The term $c_{66}d_s$ can be identified as the two-dimensional form of the three-dimensional shear modulus c_{66}. For low fields where $a_0 \gg \lambda$ the isotropic three-dimensional shear stiffness is given by

$$c_{66} = \frac{\Phi_0 B}{16\pi\mu_0\lambda^2}. \tag{5.23}$$

[8]In a three-dimensional sample such dislocation-antidislocation pairs are forbidden unless they are also bound to another dislocation-antidislocation pair which contains flux of the same magnitude but opposite sign. These "quartets" do not contribute to flux motion and resistivity (see Section 5.3.5).

This has been generalised by Brandt [77] to include the effects of intervortex interactions at higher fields leading to[9]

$$\begin{aligned} c_{66} &= \frac{\Phi_0 B}{16\pi\mu_0\lambda^2}(1-b)^2\left[1-\frac{1}{2\kappa^2}\right](1-0.58b+0.29b^2) \\ &= \frac{B_{c2}^2(t)}{\mu_0}\frac{b(1-b)^2}{8\kappa^2}\left[1-\frac{1}{2\kappa^2}\right](1-0.58b+0.29b^2) \end{aligned} \tag{5.24}$$

where once again $t = T/T_c$, $b = B/B_{c2} \approx H/H_{c2}$ and κ is the Ginzburg–Landau parameter.

At this point the similarity between this and the zero field BKT model is obvious, with the only difference being that the logarithmically interacting particles are now thermally induced pairs of defects in the lattice rather than thermally created vortex pairs. In the same manner as the zero field BKT transition the logarithmic interaction leads to an unbinding of the most widely separated dislocation-antidislocation pairs at a critical temperature T_m^{2D}, thus forming free dislocations in the lattice. As the temperature is increased above T_m^{2D} dislocation-antidislocation pairs with smaller and smaller separation unbind and the density of free dislocations rises exponentially. The presence of these free dislocations drives the shear modulus to zero, resulting in the melting of the two-dimensional vortex lattice into a vortex liquid[10]. The temperature at which the dislocation mediated melting takes place is given by

$$T_m^{2D} \approx \frac{Ac_{66}a_0^2 d_s}{4\pi k_B} \tag{5.25}$$

where the constant A renormalises the shear modulus c_{66} (Equation 5.24) to the new value Ac_{66}. The renormalisation accounts for the softening of the lattice before melting due to both non-linear lattice vibrations and the existence of the bound defect pairs. It is expected that $0.4 < A < 0.75$ [78], and good agreement has been found between Equation 5.25 and exerimental results in low-T_c films and multilayers [20, 22, 26] using values of A within this range. The interaction between the dislocation-antidislocation pairs (Equation 5.22) is approximately an order of magnitude smaller than the corresponding interaction between a pair

[9]The shear modulus c_{66} is dispersionless so there is no dependence on the wave vector of the lattice displacements, although this is not true of the other two elastic moduli, $c_{11}(k_\perp)$ and $c_{44}(k_\parallel)$.

[10]The long range positional correlation between the vortices is destroyed at T_m^{2D}, but in fact the resulting liquid retains *orientational* order amongst the bond angles between nearest neighbour vortices until a temperature [redacted] above T_m^{2D}. This

of oppositely charged two-dimensional vortices. This means that the dislocation mediated melting temperature is significantly lower than the zero field BKT transition temperature T_{BKT}. Using Equations 5.17 and 5.25 the two can be related approximately by

$$T_m^{2D} \simeq \frac{A}{4\sqrt{3}\pi}\left(\frac{T_{BKT}}{1 - T_{BKT}/T_c}\right) \tag{5.26}$$

where the term in parenthesis accounts for the different temperatures at which the penetration depth enters Equations 5.17 and 5.25.

The resistive properties of the two-dimensional superconducting layers in a magnetic field are also similar to the zero field case with a power law form for the IV characteristic at temperatures below T_m^{2D} and a linear IV characterstic at low currents above T_m^{2D}. The finite resistivity is the result of the motion of unbound dislocations which experience a Lorentz force in a similar manner to ordinary vortices. This particular form for the IV characteristic assumes that the underlying vortex lattice is pinned by impurities (see Section 5.3) otherwise the entire lattice would move under the influence of the Lorentz force giving a linear resistance at all temperatures. Furthermore the possibility of dissipative motion of the bound dislocation pairs has been ignored at this stage, but will be dealt with in Section 5.3.3 below.

Just as in the zero field case finite interlayer coupling can modify the nature of the BKT transition in the two-dimensional vortex lattice. The next section deals with the criteria under which the system may be considered two-dimensional, and discusses the effects of finite coupling and the transition to three-dimensional melting.

5.2.5 Layer Decoupling and Dimensional Crossover

In weakly anisotropic superconductors the structure of the vortices is basically the same as in the isotropic case. As the anisotropy increases, however, the vortices can be better described in terms of pancake vortices which exist within the superconducting layers coupled together into a string by their magnetic and Josephson interactions [79]. The magnetic coupling comes from the interaction between the fields of the pancake vortices in different layers, while the Josephson coupling is due to the phase differences across the layers that result when vortex segments in neighbouring layers are misaligned. It can be shown that the Josephson term dominates the magnetic coupling for all but the most weakly coupled layered samples [6]. Depending on the strength of the coupling relative to the

intraplane interactions the vortices may behave as either three-dimensional line objects or as independent two-dimensional pancake vortices.

In terms of the melting transition the requirement for 2D behaviour is that the Josephson coupling energy be much less than the energy needed to melt the 2D lattice, thus ensuring that the interaction between the dislocation-antidislocation pairs has the required logarithmic form. Equating the Josephson term to the the 2D melting temperature yields the crossover field [69] separating 2D and 3D behaviour

$$B_{2D} = \frac{4\Phi_0}{d_s^2\gamma^2} \tag{5.27}$$

where γ is the anisotropy defined in Equation 5.7. A similar method for calculating the 3D-2D crossover field is to compare the energy of the most significant tilt modes to the energy of the most significant shear modes. The most significant modes are defined as the thermal fluctuations which give rise to the largest displacements of the vortices from their equilibrium positions. Below the 3D-2D crossover field the tilt energy is greater than the shear energy and the vortices in neighbouring layers are strongly coupled, whereas above the crossover field the tilt energy is much lower and is in fact dominated by tilt modes with wavelength less than the interlayer spacing. This method leads to the expression for the crossover field [6]

$$B_{2D} = \frac{\pi\Phi_0}{d_s^2\gamma^2} \ln\left(\frac{d_s\gamma}{\xi_{ab}}\right). \tag{5.28}$$

The vortex structure above and below the decoupling field is illustrated in Figure 5.7.

The field B_{2D} marks the crossover in the behaviour of the melting transition. For fields above B_{2D} an associated decoupling type transition can be induced by the finite thermal energy of the vortices. Above B_{2D} the thermal motion of the vortices causes a large average difference between the positions of the pancake vortices in one layer and the positions of the corresponding pancake vortices in the neighbouring layers. This tends to randomise the difference in the phase of the order parameter between the layers, and therefore the interlayer Josephson coupling is reduced [6]. In addition thermal fluctuations can excite defects in the vortex lattice in the form of dislocation-antidislocation pairs. Individual dislocation-antidislocation pairs introduce net flux into the layer in which they exist (see Figure 5.6), however in the presence of interlayer coupling this extra flux has an infinite Josephson coupling energy to the other layers [69]. The

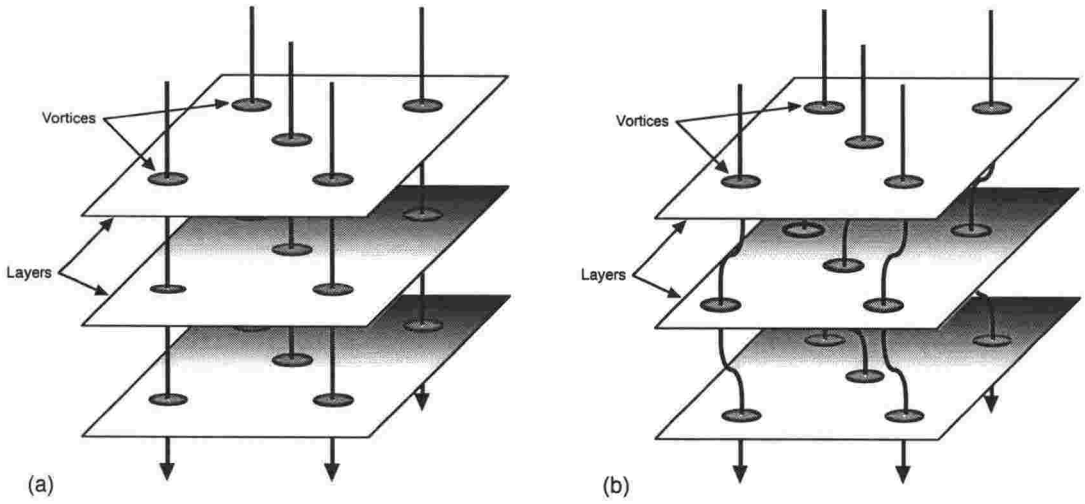

Figure 5.7: (a) A three-dimensional ($B < B_{2D}$) vortex configuration in a layered superconductor. The pancake vortex positions are correlated over several layers. (b) A two-dimensional ($B > B_{2D}$) vortex configuration in a layered superconductor. The tilt modes have wavelength less than the interlayer spacing. The vortices are shown as continuous lines for clarity, but in reality they are not correlated across the layers.

dislocation pairs must therefore be bound to other pairs which introduce the opposite flux into the layer (forming "quartets") so that the net added flux is zero. However entropy considerations mean that above a certain temperature T_{dc} the quartets can unbind leading to a proliferation of free dislocation pairs which tend to destroy the vortex correlations between layers. Overall the thermal motion of the vortices and the proliferation of defects upset the Josephson coupling between the layers and lead to a decoupling transition.

The behaviour can be summarised as follows. For fields above B_{2D} the transition to the 2D melted liquid occurs in two steps, the first a decoupling transition driven by the unbinding of the quartets into free dislocation pairs, followed by the BKT melting transition where the dislocation pairs themselves unbind. At fields below B_{2D} the layer decoupling transition occurs above the 3D melting line, so the melting transition is three-dimensional in nature. The phase above the decoupling transition is known as an entangled vortex state due to the wandering nature of the vortex lines threading through the layers [80]. Just above B_{2D} the finite interlayer coupling alters the logarithmic form of the interaction between the dislocation-antidislocation pairs leading to an increase in the melting temperature above T_m^{2D}, and thus the 2D melting line merges smoothly with the 3D melting line as the field is lowered to B_{2D}.

Finally, in samples with both a small anisotropy and a small total thickness there is also the possibility of a further crossover from 3D to 2D behaviour as the field is reduced well below B_{2D}. At very low fields the energy of the most

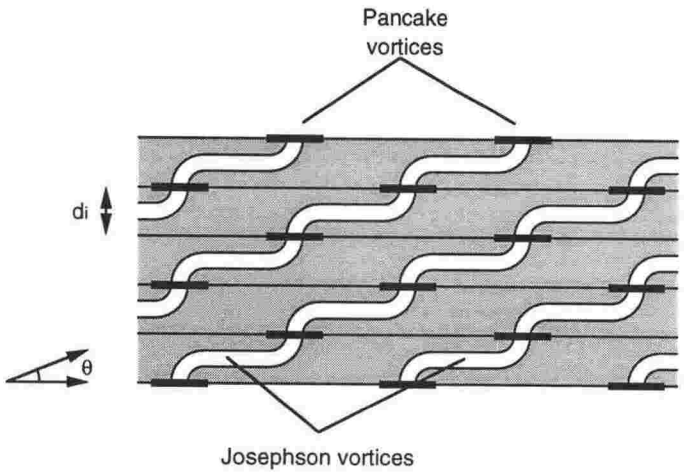

Figure 5.8: A lattice of stepwise vortices threading a strongly layered superconductor at an angle θ to the layer plane. The vortices consist of pancake vortices in the layer planes connected by Josephson vortices lying between the layer planes.

favourable tilt deformation may become greater than the two-dimensional melting temperature for the whole sample. In this case the tilt modes cannot be excited in such a thin sample and the vortices are straight over the total sample thickness, so the melting is again of the BKT type.

5.2.6 Non-Perpendicular Fields

So far the applied field has been assumed to lie along the c-axis of the layered superconductor, in which case the role of the layers is to enhance the tilt modes of the vortex lattice and ultimately to lead to a crossover in the dimensionality of the melting transition. It is of course interesting to ask whether the vortex state and the melting transition are different in nature when the field is instead applied along the ab direction, or at any arbitrary angle in between.

If the anisotropy is weak then the melting transition in a parallel field will be similar in nature to the perpendicular field case, although with the field applied parallel to the layers the tilt modes will not be enhanced by the layering as they were in the perpendicular situation. The 3D melting line (Equation 5.20) can be generalised to arbitrary angles between the field and the layers by using the prescription of Blatter, Geshkenbein and Larkin described in Section 5.1. This yields an angle dependent melting line given by

$$B_m(T,\theta) = \frac{B_m(T,\pi/2)}{(\gamma^{-2}\cos^2\theta + \sin^2\theta)^{1/2}} \tag{5.29}$$

where $B_m(T,\pi/2)$ is the melting line with the field applied perpendicular to the layers ($\theta = \pi/2$).

For the case where the anisotropy is strong so that the anisotropic GL theory does not apply the actual structure of the vortices is altered. Solution of the Lawrence-Doniach equations for a parallel field shows that instead of the usual Abrikosov vortex structure discussed in Section 5.1 the field penetrates in the form of so called Josephson vortices [6,81]. The Josephson vortices are centred between the superconducting layers and differ from Abrikosov vortices in that there is no longer complete suppression of the superconducting order parameter in the layers immediatley adjacent to the vortex core. The core now has dimensions γd_i and d_i along the ab or c directions respectively, in contrast to the core dimensions ξ_{ab} and ξ_c of an Abrikosov vortex. On the other hand the screening currents and magnetic field patterns are still somewhat similar to those in the Abrikosov vortices where the field extends a distance $\gamma\lambda$ along the ab direction and a distance λ along the c direction. If the field is tilted away from the parallel orientation then the field penetrates as a series of stepwise vortices [81,82] consisting of pancake vortices in the superconducting layers connected by Josephson vortices lying between the layers as shown in Figure 5.8. The existence of these stepwise vortices has been elegantly demonstrated using numerical simulations by Machida and Kaburaki [83] who observed relatively straight vortex lines in simulations involving weakly layered samples and stepwise vortices in strongly layered samples.

When the free energy of the vortex lines is calculated as a function of the angle θ between the applied field and the layer planes the structure of the stepwise vortices leads to a term linear in θ. This linear term causes a lock-in transition where the flux lines align themselves perfectly with the layers for angles close to $\theta = 0°$, thereby minimising the disturbance of the superconducting order parameter in the superconducting layers. Within this angular regime the overall energy of the lattice structure is minimised when the lattice constant is such that all of the vortex cores lie between the superconducting layers, which can lead to interesting commensurability effects as the field (and hence the lattice constant) is changed [84].

Finally, it has been suggested that at sufficiently high parallel fields there may be a field driven decoupling transition, which can be accompanied by vortex lattice melting [6]. Whether or not this transition actually exists in real layered superconductors in a parallel field currently remains unknown.

5.2.7 Experimental Evidence for Melting

To conclude the discussion on vortex lattice melting it is appropriate to give a brief review of the current experimental evidence for the existence of the melting transition in clean systems. A hysteretic jump in both the resistance [85,86] and the magnetisation [87,88] has been observed to occur at the same temperature in very clean bulk single crystals of $YBa_2Cu_3O_{7-\delta}$, which provides evidence for the existence of the melting transition (the drop in resistance is due to the rise in the effectiveness of pinning in the vortex solid as described in Section 5.3 below). The position of the transition on the magnetic phase diagram is well described by the model of Houghton *et al.* described above (Equation 5.20). However the best evidence for the melting transition has been discovered more recently by Schilling *et al.* [89] who have measured the latent heat ($\sim 0.5k_BT$ per vortex per layer) at the melting transition of very pure $YBa_2Cu_3O_{7-\delta}$ samples. The latent heat has been observed with the field applied both parallel and perpendicular to the superconducting layers [90,91] and the melting line thus determined scales according to Equation 5.6 as would be expected for $YBa_2Cu_3O_{7-\delta}$ where the anisotropy is not too strong. These experiments along with muon spin rotation and neutron diffraction work (see references in [89]) provide clear evidence for the existence of a first order melting transition in the vortex lattice in clean three-dimensional systems. The first order nature of the melting transition is also in agreement with theoretical predictions [92].

Hysteretic steps in the resistance [93,94] and magnetisation [95,96] of the much more highly anisotropic $Bi_2Sr_2CaCu_2O_{8+\delta}$ have also been observed, providing evidence for a first order melting transition similar to that in $YBa_2Cu_3O_{7-\delta}$, but so far no calorimetric measurements are available to support this. These transitions are only observed in low fields which is consistent with the field induced decoupling picture presented in Section 5.2.5 above.

When disorder is added to the system the three-dimensional first order melting transition is smoothed into a continuous second order transition [6,97]. In this case the freezing is into a vortex glass rather than a vortex lattice as will be described below.

5.3 Flux Pinning and Vortex Dynamics

In the above discussion it was stated that a linear resistance results from the free motion of vortices under the influence of an applied current. This is a surprising result as it would appear that the current should avoid the normal

cores of the vortices and propagate solely through the superconducting region outside the cores, thus giving rise to no dissipation at all. This is indeed what happens if the vortices are prevented from moving by some pinning force, however Maxwell's equations imply that a moving magnetic vortex has an associated electric field. Inside the vortex core this electric field turns out to be directed perpendicular to the vortex motion but parallel to the applied current which causes the current to flow continuously through the normal cores, thus leading to the linear dissipation [2]. According to Bardeen and Stephen [98] the resulting flux flow resistivity is given by

$$\rho_{ff} = \rho_n \frac{B}{H_{c2}} \tag{5.30}$$

where ρ_n is the normal state resistivity. This form for the resistivity was determined by equating the Lorentz force with the viscous drag force on the vortex. In the absence of any pinning the viscous drag results from the finite rate at which the material can be converted from the superconducting to the normal state at the leading edge of the moving vortex and from the normal to superconducting state at the trailing edge.

This discussion of the flux flow resistivity makes it clear that in order to exploit the benefits of dissipation free current propogation in superconductors the magnetic vortices must be prevented from moving. This can be achieved through the introduction of pinning centres - inhomogeneities in the sample - which attractively interact with the vortex cores. Almost all superconductors contain inhomogeneities on a microscopic scale, whether they be due to crystalline defects or the inclusion of impurities. These inhomogeneities locally decrease the condensation energy of the superconducting state, and as such they have an attractive interaction with the normal core of the vortices where superconductivity is already suppressed. It is this attraction to the defects in the underlying superconductor which pins the vortices and opposes the Lorentz force due to an applied current.

In the following sections the inhomogeneities will be assumed to represent point pinning sites, where the pinning centres are much smaller than the vortices themselves. The range of the interaction between the pinning sites and the vortices is thus determined by the coherence length ξ which sets the minimum scale which the vortex core can resolve. The strength of the pinning is critically dependent on the sample characteristics such as the dimensionality and the density of pinning sites and also on the temperature and the strength of the applied field. This section gives a discussion of the effects of pinning forces on the vortex

structure and then, more importantly, explores the different dynamic regimes which result under different strengths of the applied current.

5.3.1 Collective Pinning Theory

One of the most successful approaches to understanding the effect of disorder on the vortex lattice is the collective pinning theory of Larkin and Ovchinnikov [99] who considered the combined action of a random distribution of point pins. To begin the discussion of the collective pinning theory the vortices will be assumed to exist in an isotropic three-dimensional superconductor, although the isotropic results can be generalised to the more complicated anisotropic case through the use of the scaling rule presented in Equation 5.6. Later in the present section the collective pinning results for a decoupled two-dimensional layered system will be presented.

The main ideas of the collective pinning theory can be illustrated by first considering an isolated vortex interacting with the pinning sites. Because of the random placement of the point pins with respect to the vortex core the pinning forces on a rigid flux line of length L will add up only as in a random walk, leading to a net pinning force which grows as $L^{1/2}$. On the other hand the Lorentz force due to an applied current grows linearly with the length of the flux line, so the current density at which the Lorentz force equals the pinning force must scale as $L^{-1/2}$, and vanish as the sample size increases.

This conclusion does not hold for an elastic flux line however, because, as shown in Figure 5.9, an elastic flux line can alter its shape in order to accommodate itself in the most favourable fashion to the random distribution of pinning sites. By so doing the vortex minimises the loss of condensation energy in the core, but this is at the expense of the extra elastic energy of the vortex line. The deformed vortex can be considered to be broken up into individual segments of characteristic length L_c, where L_c is the minimum vertical scale over which the transverse deformation of the vortex line becomes larger than the range ξ of the pinning forces. Beyond this length the vortex deforms to match the pinning potential so that the pinning centres no longer combine as in a random walk, thereby cutting off the sublinear growth in the net pinning force. Each of the individually pinned segments feels a pinning force proportional to $L_c^{1/2}$, and at small values of L_c this pinning force can compete favourably with the Lorentz force on the segment. The net pinning force is thus enhanced by the elasticity of the vortex line in such a way that a finite critical current is required before free flux motion occurs.

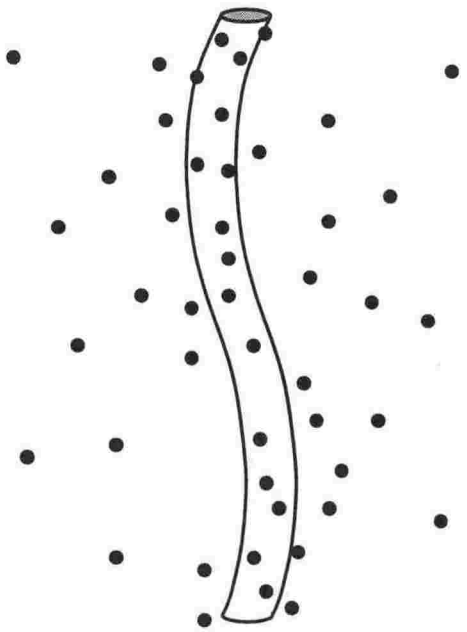

Figure 5.9: A single vortex line which is pinned by the collective action of a random distribution of point pinning centres.

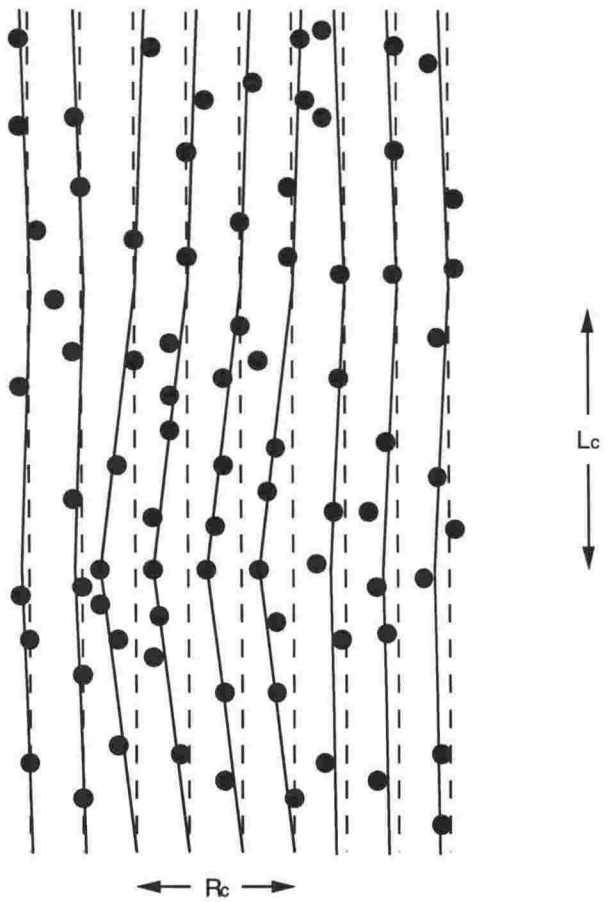

Figure 5.10: A schematic representation of the correlation volume V_c. The periodicity in the flux lattice is upset by the pinning forces only over the lengths R_c and L_c which define the correlation volume. The dashed lines show the positions of the vortices in the unperturbed lattice.

Larkin and Ovchinnikov not only considered isolated vortices but also developed these ideas of collective pinning to cover the entire vortex lattice, where the distortion in the vortices is now taken up over a so called correlation volume V_c of length L_c and transverse dimension R_c. Within the correlation volume the periodicity of the vortex lattice is relatively undisturbed, but at lengths longer than R_c or L_c the lattice structure is upset by either shear or tilt deformations respectively. This is illustrated in Figure 5.10, where it can be seen that the whole correlation volume distorts to take advantage of the pinning sites. The expression for the free energy $\mathcal{F}[\mathbf{u}]$ of a flux line lattice in which the vortices are deformed by a distance $\mathbf{u}$ from their equilibrium sites is defined through the shear and tilt moduli considered previously in the discussion of the melting transition. Because $c_{11} \gg c_{66} \approx c_{44}$ the lattice accommodates itself to the pinning potential through shear and tilt deformations only, so that

$$\mathcal{F}[\mathbf{u}] = \int d^3r \left[\frac{c_{66}}{2}(\nabla_\perp.\mathbf{u})^2 + \frac{c_{44}(k_\parallel)}{2}(\partial_z \mathbf{u})^2 + E_{pin}(\mathbf{r},\mathbf{u}) \right] \tag{5.31}$$

where E_{pin} is the pinning energy ($\propto n^{1/2}$ due to the random walk process, where n is the density of pinning sites[11]), $\nabla_\perp.\mathbf{u}$ is the fractional distortion in the direction perpendicular to the applied field (shear), $\partial_z \mathbf{u}$ is the fractional distortion of the lattice in the direction parallel to the field (tilt) and the dispersion in the tilt modulus $c_{44}(k_\parallel)$ has been included. As the lengths R_c and L_c are defined to be the distances in the lattice over which the flux lines are distorted from their equilibrium positions by a distance equal to the range ξ of the point pinning forces the fractional distortions can be approximated by

$$\nabla_\perp.\mathbf{u} \approx \frac{\xi}{R_c}, \quad \partial_z \mathbf{u} \approx \frac{\xi}{L_c}. \tag{5.32}$$

Larkin and Ovchinnikov used the expression for the free energy (Equation 5.31) to find the collective pinning lengths. Several different collective pinning regimes emerge from the analysis, depending on the size of the collective pinning lengths relative to λ, the interaction length of the vortices. At the lowest fields the interaction between the vortices is unimportant and the sample is in the single vortex regime. Here, where the vortices behave independently of each other, the length R_c has no relevance so the collective pinning may be characterised by the single length L_c which is determined directly by minimising the free energy per unit

[11] n is the *local* density of pinning sites per unit volume in the region where the deformed vortex is situated. Fluctuations away from the average pinning site density are required in order to pin the vortices effectively because if the density of pinning sites was entirely homogeneous the vortices would not be able to lower their energy by finding the optimal position.

length with respect to the length L of the vortex segments.

At higher fields, where the intervortex interactions cannot be ignored, both of the lengths R_c and L_c are needed to characterise the collective pinning of the lattice. A slightly different approach than that used in the single vortex case is needed. Firstly the free energy is used to determine the so called positional correlator given by $\langle u^2(\mathbf{r})\rangle^{1/2} \equiv \langle[\mathbf{u}(\mathbf{r}) - \mathbf{u}(\mathbf{0})]^2\rangle^{1/2}$ where the angular brackets represent the average over all of the disorder in the sample. This correlator gives a measure of the relative distortion from their equilibrium sites of two vortices separated by a distance $\mathbf{r}$. The lengths R_c and L_c are then defined in terms of the positional correlator by $\langle u^2(R_c)\rangle \simeq \xi^2$ and $\langle u^2(L_c)\rangle \simeq \xi^2$. The calculation of the positional correlator identifies two different regimes of vortex bundle collective pinning. At fields slightly above the single vortex limit the small bundle pinning regime is entered, characterised by a correlation length R_c which extends over a few vortices only. In this regime the positional correlator is strongly affected by the dispersion in c_{44} due to the small length scales of the tilt deformations. At higher fields the large bundle regime is entered where the distortions are over long length scales and the dispersion is no longer important. The collective pinning lengths may be summarised as

$$
\begin{aligned}
\textit{Single vortex}: \quad L_c^{sv} &\simeq \left(\frac{\Phi_0^4}{256\pi^4\lambda^4 n f^2}\right)^{1/3}, \quad L_c^{sv} < a_0 \\
\textit{Small bundles}: \quad R_c &\simeq a_0 \exp\left[\tilde{c}\left(\frac{L_c^{sv}}{a_0}\right)^3\right], \quad a_0 < R_c < \lambda \\
L_c &\simeq \frac{R_c^2}{a_0}, \quad a_0 < L_c < \frac{\lambda^2}{a_0} \\
\textit{Large bundles}: \quad R_c &\simeq \lambda\left(\frac{L_c^{sv}}{a_0}\right)^3, \quad \lambda < R_c \\
L_c &\simeq \frac{\lambda}{a_0} R_c, \quad \frac{\lambda^2}{a_0} < L_c \\
\textit{Pinned volume}: \quad V_c &\simeq R_c^2 L_c
\end{aligned}
\tag{5.33}
$$

where f is a parameter which measures the strength of the pinning force due to each of the pinning sites[12], $\tilde{c}$ is a constant of order unity and L_c^{sv} is the collective pinning correlation length along the field in the single vortex pinning regime.

[12]The size of f is determined by the degree of suppression of the condensation energy at the pinning site.

Note that due to the lack of interaction R_c is not defined for single vortices, in which case the collective pinning volume is instead equal to $\xi^2 L_c$.

The total energy associated with the pinning of a single vortex segment can be defined in terms of the pinning strength f. The random walk argument showed that the net pinning force is given by $fN^{1/2}$ where N is the total number of randomly positioned pinning sites which interact with the vortex over the correlation length. The pinning force extends to a distance ξ only, so the pinning energy is approximately equal to $fN^{1/2}\xi$. In terms of the pinning site density n the total number of pinning sites can be written as $N = nV = nL_c\xi^2$ which yields the collective pinning energy

$$U_c \simeq f(n\xi^4 L_c)^{1/2}. \tag{5.34}$$

For a vortex bundle the collective pinning energy can be cast into a simple form by noting that the vortices will continue to relax into the pinning sites until the energy gain from doing so is balanced by the cost in elastic energy of further deformation. Thus, at equilibrium, the elastic and pinning energies are equal, so for vortex bundles the collective pinning energy can be written in terms of the shear distortions as

$$U_c \simeq c_{66}\left(\frac{\xi}{R_c}\right)^2 V_c. \tag{5.35}$$

This can be evaluated further by insertion of the correlation lengths given in Equations 5.33.

One of the most important applications of the collective pinning theory is the calculation of the critical current density j_c neccessary to overcome the pinning forces and induce motion in the vortices. Below j_c the pinning dominates and the vortices are prevented from moving, whereas above j_c the vortices are driven over the pinning barriers and a finite resistivity results from the vortex motion. According to the collective pinning model the pinning force on the correlation volume as a whole competes with the Lorentz force. The Lorentz energy needed to move the correlation volume a distance equal to the range ξ of the pinning potential is equal to $jBV_c\xi$, and equating this with the collective pinning energy yields the critical current density as

$$j_c = \frac{1}{B}\frac{U_c}{V_c\xi}. \tag{5.36}$$

Equation 5.36 implies that the critical current depends on the size of the correlation volume. The correlation volume decreases either as the pinning forces

become stronger, or as the lattice softens (smaller c_{66} or c_{44}) and is more able to accommodate itself to the pinning potential. Thus, as would be expected, either increased pinning or a more easily deformed lattice results in an increase in the critical current density.

A further result of the collective pinning theory regards the loss of long range order in the vortex lattice. At distances greater than a characteristic length R_a ($\gg R_c$) the disorder induced displacements of the vortices away from their equilibrium positions (given by the positional correlator $\langle u^2(\mathbf{r})\rangle^{1/2}$) become larger than the lattice constant a_0, so the periodicity of the vortex lattice is no longer maintained. At these lengths the above description in terms of the small elastic distortions is no longer valid for describing the pinning[13]. In fact it has been argued [44] that at these length scales the optimal distortions are caused by the appearance of either dislocation loops[14] in three dimensions or dislocation-antidislocation pairs in two dimensions, rather than the elastic distortions considered above. The dislocation loops or pairs are similar to the defects discussed in terms of the melting transition, but in this case the defects are a feature of the quenched disorder in the underlying superconductor rather than being thermally induced.

Another important question which arises from the analysis of the collective pinning theory relates to the effect of the disorder in the vortex lattice on the elastic properties themselves. At distances greater than R_a the long range order of the vortex lattice is lost, so it could be expected that the lattice is actually driven into a disordered liquid phase by the pinning. However it turns out that although the disorder can significantly lessen the shear modulus it is never sufficient to drive it all the way to zero [6]. Thus the disorder does not destroy the elastic properties of the vortex lattice, and the discussion of the collective pinning theory in terms of elastic distortions is self consistent.

These results can be generalised to the weakly anisotropic case through use of the scaling Equation 5.6. It should be noted however that in the uniaxially anisotropic case relevant for layered superconductors the presence of the layers leads to the splitting of the tilt and shear modes into two orthogonal components. This is most easily seen by considering the case of a field applied parallel to the layers. Clearly shear and tilt modes involving deformations out of the layer

[13]Nattermann [100] has shown that at this scale the pinning is like that of charge density waves.

[14]The dislocation loops are similar to the dislocation-antidislocation pairs which can exist in two-dimensional superconductors, but unlike a dislocation-antidislocation pair a three-dimensional dislocation loop does not add any net flux to the vortex lattice. For a picture of a dislocation loop see [101].

plane require a greater energy than modes involving deformations in the layer planes. For a field applied perpendicular to the layer planes the tilt modes are enhanced relative to the isotropic case, with a corresponding decrease in the length L_c. Apart from these differences the overall results are much the same as the isotropic case in terms of the concepts involved. A complete description of the anisotropic generalisation of the collective pinning theory can be found in Ref. [6].

In the strongly anisotropic limit where the layers are effectively decoupled the collective pinning theory has been analysed by Vinokur, Kes and Koshelev [102]. For a field applied perpendicular to the layers the crossover to two-dimensional collective pinning occurs if the correlation length L_c becomes limited by the interlayer spacing d_i. Clearly this becomes more likely as the interlayer coupling is reduced so that the disorder induced tilt deformations can occur over shorter distances. If the field is small enough that the intervortex interactions within the layers can be ignored then the correlation length L_c appearing in the single vortex collective pinning energy (Equation 5.34) can be replaced with the layer spacing d_i to give the two-dimensional collective pinning energy of a single pancake vortex $U_c^0 \simeq (nf^2\xi^4 d_i)^{1/2}$. The corresponding critical current j_c^0 is given by

$$j_c^0 = j_0 \left(\frac{4\pi\lambda}{\Phi_0}\right)^2 \frac{U_c^0}{d_i} \tag{5.37}$$

where j_0 is the depairing critical current defined in Equation 1.1. If the field is increased then the intervortex interactions within the plane become important. In this case the collective pinning radius can be obtained by balancing the pinning energy in the area R_c^2 against the elastic interaction energy within the same area. This leads to

$$R_c^{2D} = \frac{d_i}{U_c^0} \left(\frac{4\pi\lambda}{\Phi_0}\right)^2 \frac{\xi^2}{4a_0} \tag{5.38}$$

and the corresponding critical current is

$$j_c^{2D} = j_c^0 \frac{a_0}{R_c^{2D}}. \tag{5.39}$$

Note that in Equations 5.37 and 5.39 the superscripts refer to the fact that the correlation volumes are effectively zero- and two-dimensional respectively.

As discussed above the pinning forces result from the attraction of the vortex cores to the region surrounding the pinning sites where the order parameter is suppressed. In layered superconductors the order parameter is also suppressed in the region between the superconducting layers, giving rise to the possibility of

intrinsic pinning of vortices when the field is applied parallel to the layer planes. This problem has been analysed using the Lawrence-Doniach formulation in the weak field limit by Barone, Larkin and Ovchinnikov [103] and in the strong field limit by Ivlev and Kopnin [104,105]. The results for the intrinsic critical current density j_c^{in} needed to induce vortex motion between the layers (i.e. perpendicular to the planes) can be summarised as follows

$$\begin{aligned}
\textit{Low field}: \quad j_c^{in} &\approx 4\times 10^3 j_0 \left(\frac{\xi}{\gamma d}\right)^{7/2} e^{-5.02\pi\xi/\gamma d}, \quad \gamma d \ll \xi \\
j_c^{in} &\approx j_0\left[1-\left(\frac{\xi}{\gamma d}\right)^{1/3}\right], \quad \gamma d \gg \xi \\
\textit{High field}: \quad j_c^{in} &\approx j_0\left(\frac{8\xi}{\gamma d}\right)^2\left(1-\frac{B}{H_{c2}}\right)e^{(-8(\xi/\gamma d)^2)}, \quad \gamma d \ll \xi \\
j_c^{in} &= \frac{8j_0}{1.16}\left(\frac{\xi}{\gamma d}\right)^9\left(1-\frac{\gamma^2 d^2}{2\xi^2}\right)^{3/2}\left(1-\frac{B}{H_{c2}}\right)^{3/2}, \quad \gamma d \lesssim \xi.
\end{aligned} \tag{5.40}$$

5.3.2 Thermal Depinning

Before considering the interaction between the Lorentz and pinning forces it is first worth noting the effects of finite temperature on the size of the pinning force. As discussed in Section 5.2.3 at any finite temperature the vortices will undergo thermal motion about their equilibrium sites, where the equilibrium sites in the presence of pinning forces are those determined by the collective pinning theory. As the range of the point pinning forces is only equal to the coherence length ξ the thermal motion will tend to average out the pinning force by sampling the area around the pinning site. This in effect increases the range of the pinning potential from ξ to a new value r_p given by [106]

$$r_p^2(T) \simeq \xi^2(1+\langle u^2\rangle_T/\xi^2) \tag{5.41}$$

where $\langle u^2\rangle_T$ is the amplitude of the thermal fluctuations of the vortex lines. The pinning force (proportional to the gradient of the pinning potential) is thus reduced leading to correspondingly longer values for the correlation lengths R_c and L_c, and smaller values for j_c in the various regimes. At a high enough temperature T_{dp} the vortices are effectively free of the pinning forces altogether [106] at which point the collective pinning theory breaks down and the critical current is

zero.

5.3.3 Thermally Assisted Flux Motion

The theory of flux motion in type-II superconductors is made considerably complex due to the large number of ways in which the motion can occur. The discussion of flux motion will proceed as follows. Firstly the theory of elastic flux creep will be introduced for single vortices, including the important distinction between creep at low driving currents and creep at currents close to the critical current. Following this the collective pinning results will be used to generalise the single vortex case to include the interactions between the vortices in the vortex solid. This leads naturally to the vortex glass model which describes the melting of the vortex solid into the vortex liquid in the presence of disorder. The section will be concluded with a discussion of plastic vortex motion in both the vortex solid and the vortex liquid.

The collective pinning theory showed that the elastic properties of the vortices allow them to take advantage of pinning forces so that a non-zero critical current is needed to prompt motion of the vortices away from the optimal pinning sites. This immediately identifies two different regimes in the presence of an applied current. For currents above j_c the Lorentz force is strong enough to overcome the pinning forces and dissipative flux motion results. For currents below j_c the pinning forces dominate the Lorentz force, but there is still the possibility of vortex motion due to a process known as thermally activated flux flow (or thermally activated flux creep), where the vortices gain the energy to jump from one pinning site to another from the thermal energy in the superconductor. The current exerts a Lorentz force on the vortices so that jumps in one particular direction are favoured, resulting in a non-zero net vortex velocity due to the thermally activated processes. This net vortex velocity is typically much lower than that experienced in the absence of pinning forces, but nevertheless any flux motion still leads to a finite resistance and the destruction of true superconductivity.

The original theory of flux creep was developed by Anderson and Kim [107] who took the following approach. In the absence of an applied current the vortices take advantage of the pinning forces and arrange themselves into the lowest energy state. If a current is then applied the Lorentz force adds a term to the free energy which increases linearly with the displacement of the vortices. This leads to the existence of new low lying states to which the vortices can move, where the energy gain from the Lorentz force outweighs the deformation and pinning energies which must be overcome. Therefore, in the presence of

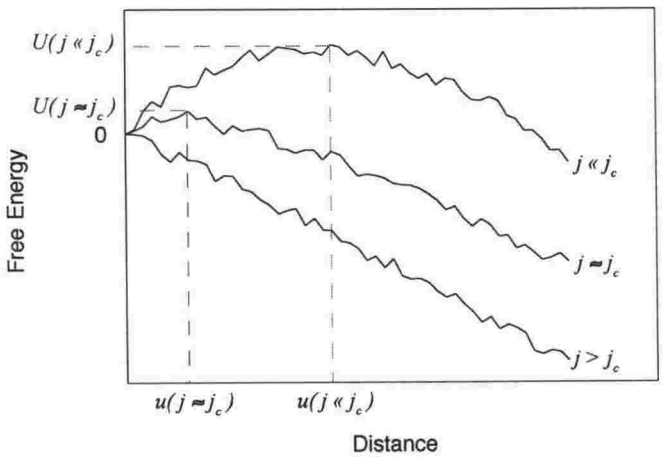

Figure 5.11: A schematic representation of the free energy of a vortex as a function of the distance from the zero current equilibrium pinning site. The three curves represent three different values of the applied current, where the potential barrier U between the metastable states goes to zero when $j = j_c$. The minimum size of the activated hop neccessary to overcome the barrier is labelled u.

an applied current, the original vortex configuration is only *meta*stable in that other lower energy states exist which are separated from the present state by finite energy barriers provided by the pinning and elastic forces. The activation energy U needed to excite the vortices into a new metastable state is equal to the maximum height of the potential barrier between the pinning sites. The form of the potential thus experienced by each of the vortices is shown schematically as a function of position in Figure 5.11 for three different values of the applied current. It can be seen that both the size of the activation energy and the distance between neighbouring metastable states decrease as the current increases, with the activation energy going to zero when $j = j_c$.

To be more specific the actual thermally activated motion proceeds via a nucleation process where a segment of a single vortex or several vortices distorts in such a way that the segment moves over the potential barrier and into a new metastable state. This process is illustrated in Figure 5.12. The size of the activated bundle, the distance over which it is translated and the activation energy required are determined by the forces acting on the vortices in a similar manner to the collective pinning theory, except now there is an extra term due to the Lorentz force as well as the pinning and elastic forces. It is worth noting that the distortion in the vortices which nucleates the hopping process can be thought of as the addition of a loop of flux bound to each vortex line as shown by the dashed lines in Figure 5.12.

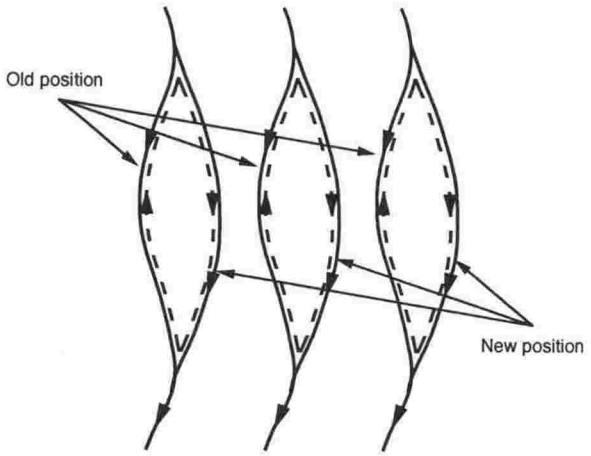

Figure 5.12: A thermally activated kink in a vortex bundle which provides the nucleus for activated flux motion. The kink can be thought of as the addition of a flux loop to each vortex line, as shown by the dashed curves.

Anderson and Kim noted that the flux motion is most likely to proceed via the hopping of vortex bundles rather than via the hopping of a single vortex, because the gain in energy from the Lorentz force depends on the bundle volume, whereas, to a good approximation, the cost in elastic energy depends only on the surface area of the displaced vortex bundle. They also noted that the thermally activated jumps occur at a rate proportional to $\exp(-U/k_BT)$ where $U = U(B,T,j)$ is the activation energy [108]. The total creep rate is the sum of the creep rate in the direction of the Lorentz force and in the direction opposite to the Lorentz force. If the hopping processes are assumed to consist of a flux bundle of volume V being translated a constant distance u then the Anderson-Kim flux creep resistivity is given by

$$\begin{aligned} \rho &= \frac{B\nu_0}{j} e^{-U(B,T)/k_BT} \left(e^{jBVu/k_BT} - e^{-jBVu/k_BT} \right) \\ &= \frac{2B\nu_0}{j} e^{-U(B,T)/k_BT} \sinh\left(\frac{jBVu}{k_BT} \right) \end{aligned} \tag{5.42}$$

where ν_0 is the creep velocity which would exist if there were no barriers. The above formula assumes an activation energy for flux motion in the direction of the Lorentz force with a simple dependence on the current given by $U(B,T,j) = U(B,T)(1-j/j_c)$, and a corresponding activation energy for flux motion opposite to the Lorentz force given by $U(B,T,j) = U(B,T)(1+j/j_c)$. This form satisfies the requirement that the activation barrier for forward flux motion must go to

zero at the critical current j_c. For small applied currents the sinh term can be expanded to first order in j resulting in a linear resistivity independent of the current.

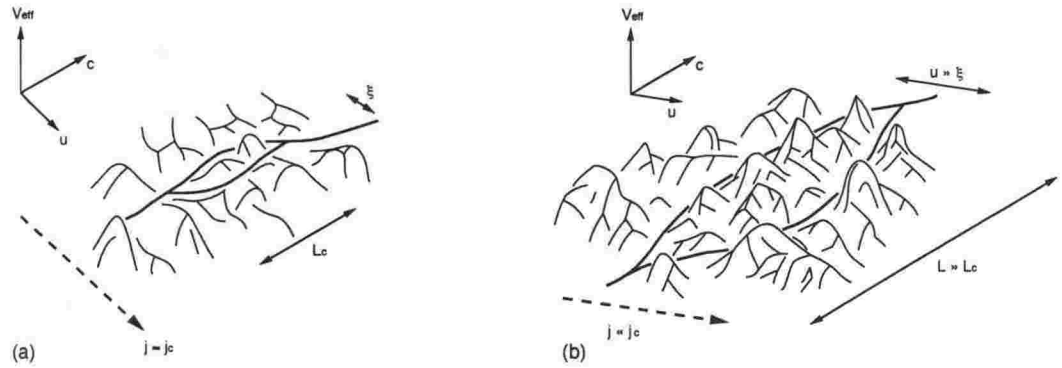

Figure 5.13: A three dimensional representation of the pinning potential V_{eff} experienced by an isolated vortex. The dashed line shows the slope of the effective potential caused by the Lorentz force. (a) The most probable hopping process between neighbouring metastable states in the presence of a large applied current. The hopping unit consists of an elementary deformation. (b) The most probable hopping process in the presence of a small applied current. A much larger hopping unit is required to find a new metastable state.

The Anderson-Kim theory introduces the basic ideas of thermally assisted flux flow, but does not provide a detailed determination of the size of the activation barriers, and nor is there any rigorous justification for the use of the linear current dependence of $U(j)$. A better understanding of the flux creep process can be gained by first considering in detail the activated motion of a single flux line. As discussed above the vortex hops from one metastable state to another in such a manner that the gain in energy from the Lorentz force is enough to compensate both the loss of pinning energy and the extra elastic energy of the vortex. If the applied current is large ($j \approx j_c$) then the Lorentz term in the free energy will dominate the elastic term and only a minimal sized jump will be neccessary for the vortex to find a new metastable state. This minimal length scale is equal to the range ξ of the pinning forces, and the length of the vortex segment which undergoes the hopping process will also be of the minimal size L_c determined by the collective pinning theory. Figure 5.13(a) illustrates a thermally activated process of this nature. The thermal activation energy which must be supplied to facilitate such a jump is equivalent to the single vortex collective pinning energy U_c (Equation 5.35) modified due to the assistance of the current. This can be written in a general form as

$$U(j) = U_c(1 - j/j_c)^{\alpha} \tag{5.43}$$

where α describes the behaviour of the activation energy near $j = j_c$. This

high current hopping picture is equivalent to the Anderson-Kim theory for a flux bundle containing a single vortex if $\alpha = 1$ and the identifications $U(B,T) = U_c$, $u = \xi$ are made in Equation 5.42.

In the other case where the current is small ($j \ll j_c$) the distance between the metastable states will be much larger, as a larger hop will be required to achieve a big enough gain from the Lorentz energy to balance the cost in terms of pinning and elastic energy[15]. Thus, unlike the high current case considered above, the hopping distance will be larger than ξ and the length L of the activated segment will be longer than the minimum length L_c, as shown in Figure 5.13(b). It has been shown [6] that for $L > L_c$ the distance u between metastable states (see Figure 5.13) scales with the length of the activated segment according to

$$u \sim \xi \left(\frac{L}{L_c}\right)^{\zeta} \tag{5.44}$$

and the corresponding energy barrier which must be overcome is

$$U(L) \sim U_c \left(\frac{L}{L_c}\right)^{2\zeta-1} \tag{5.45}$$

where $\zeta \approx 3/5$ [109] is a wandering exponent[16] characterising the behaviour of the vortex in the presence of random pinning and thermal disorder. Combining these expressions into the free energy formulation (including the elastic, pinning and Lorentz terms) and minimising the size of the barrier yields the optimal length of the activated portion

$$L_{opt} \simeq L_c \left(\frac{j_c}{j}\right)^{1/(2-\zeta)}. \tag{5.46}$$

Finally, the current dependence of the activation energy can be obtained by inserting this value for L_{opt} back into the expression for the size of the barriers (Equation 5.45) leading to

$$U(j) = U_c \left(\frac{j_c}{j}\right)^{\mu}, \quad \mu = \frac{2\zeta - 1}{2 - \zeta} \approx \frac{1}{7}. \tag{5.47}$$

Equation 5.47 displays the surprising result that in this single vortex regime

[15]The Lorentz energy grows linearly with the distance whereas the elastic energy tends to grow sublinearly with u and the pinning energy is approximately independent of u, so for a large enough hop the Lorentz term must always dominate.

[16]The fact that the value of ζ is greater than that expected in a random walk demonstrates the importance of pinning. If only thermal disorder was present the random walk value $\zeta = 1/2$ would result and the activation energy (Equation 5.45) would reduce to U_c as in the Anderson-Kim theory at low current.

consideration of the different sizes possible for the hopping nucleus has led to an activation energy which tends to infinity as the current tends to zero. This is in contrast to the Anderson-Kim expression for the activation energy which tends to the constant value U_c as the current tends to zero. The divergence in the activation energy is the hallmark of the vortex glass state[17], and is mainly a result of the elastic nature of the vortex in the random pinning potential rather than the random nature of the pinning forces themselves. The vortex glass state is of particular interest because the diverging activation energy provides the possibility of a truly superconducting state with zero linear resistance existing in the mixed state of type-II superconductors.

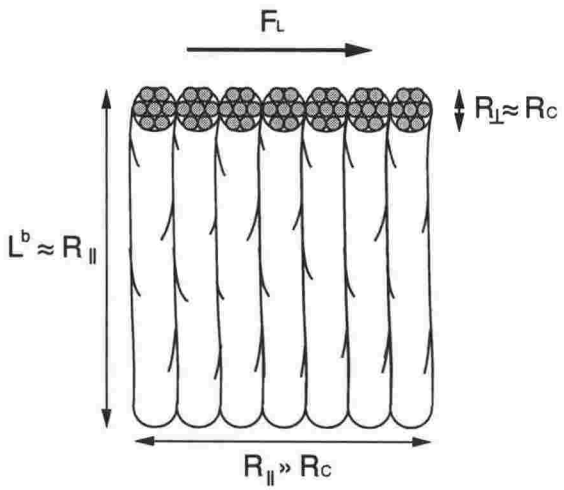

Figure 5.14: A superbundle consisting of several collectively pinned vortex bundles. The direction of the Lorentz force is shown by the arrow.

The above results apply for the case of a single vortex, where the elastic energy comes only from the vortex line energy. At large fields where the intervortex spacing is small, or at very small currents where the optimal hopping lengths become comparable to the intervortex spacing, the intervortex interactions must also be considered. As noted by Anderson and Kim the vortices will thus tend to hop in bundles rather than individually, thereby minimising the size of the elastic energy of the distortion in relation to the Lorentz energy. Unlike the collective pinning theory where the deformations were due to shear and tilt only, when the vortices hop to new pinning sites the compressional energy is also important, so all of the elastic energies must be considered when determining the optimal hopping sizes.

At high currents ($j \approx j_c$) the minimum possible hopping unit is again determined by the collective pinning theory (including intervortex interactions) as a

[17]The name "vortex glass" actually comes from the resemblance of the model to spin glasses rather than from the disordered nature of the vortex solid.

bundle of size R_c and length L_c. This represents the minimum size over which the vortex lattice can deform in response to pinning forces, and within this volume all of the vortices are pinned in a single metastable state. The compressional energy, however, makes it favourable for several such bundles to hop at once so that the overall bundle size is elongated along the direction of the jump (i.e. transverse to the applied current) into a so called superbundle (see Figure 5.14). To understand this it should be noted that the compressional energy comes only from the vortices at the ends of the hopping region, whereas the energy gain due to the hopping process is experienced by all of the bundles. The exact dimensions of the superbundle have been determined by Koshelev [6] who equated the shear, tilt and compressional energies created by the hopping process, including the effects of the dispersive nature of the elastic moduli. The results show that the dimensions of the superbundle depend on the magnitude of the field via the collective pinning lengths, and are given by

$$\begin{aligned}
R_{\|} &\simeq L^b \simeq \frac{R_\perp^3}{a_0^2}, && R_\perp < R_{\|} \simeq L^b < \lambda \\
R_{\|} &\simeq L^b \simeq \left(\frac{R_\perp^3 \lambda}{a_0^2}\right)^{1/2}, && R_\perp < \lambda < R_{\|} \simeq L^b \\
R_{\|} &\simeq L^b \simeq \frac{\lambda R_\perp}{a_0}, && \lambda < R_\perp < R_{\|} \simeq L^b
\end{aligned} \tag{5.48}$$

where $R_\perp \simeq R_c$ is the dimension of the superbundle in the direction perpendicular to the hop, $R_{\|}$ is the dimension in the direction of the hop and L^b ($> L_c$) is the dimension parallel to the field. The different regimes specified by the inequalities mark the crossovers between small, intermediate and large superbundles respectively, determined by the relative sizes of the vortex superbundle and the screening length λ. Within the small superbundle regime where the distortions are over short length scales the dispersive nature of the elastic moduli is important, whereas in the large superbundle regime all of the length scales are greater than λ and the dispersive nature of the elastic moduli no longer matters.

The vortex glass behaviour derived above in the single vortex case was observed to occur only in the low current region, but at the same time it was shown that at low enough currents the intervortex interactions become important. Therefore the intervortex interactions must be considered before it can be concluded that the low current regime truly is a vortex glass. The interactions can be included by combining the relationships between the length scales of the superbundles (Equations 5.48) with the scaling arguments used above to derive

the glassy behaviour in the single vortex limit. It turns out that the results are similar to the single vortex case in that the activation energy diverges as the current is reduced towards zero [6] i.e. the phase is indeed a vortex glass. The most important difference is that the relationships between the bundle dimensions alter the value of the glassy exponent μ in Equation 5.47 leading to

$$\mu = \begin{cases} \frac{1}{7}, & \text{single vortex} \\ \frac{5}{2}, & \text{small bundles} \\ 1, & \text{intermediate bundles} \\ \frac{7}{9}, & \text{large bundles} \end{cases} \tag{5.49}$$

where the single vortex result has been included for comparison. These results are applicable when the hopping length is less than the flux line lattice constant a_0. When the current is very low the optimal hopping length can grow to be greater than a_0 which results in a value $\mu = 1/2$ [100]. Other results have been obtained for μ in the various regimes using slightly different approaches, but in every case μ is greater than zero so it can be concluded that the elastic vortex lattice in the presence of disorder is always in a glassy state.

So far all of the results in this section describing the activated vortex motion have been for the isotropic three-dimensional case. Once again these results can be carried over into the weakly anisotropic regime by transforming the elastic and pinning energies according to the scaling laws of Blatter *et al.* (Equation 5.6). As in the collective pinning theory it should be remembered that the uniaxial nature of the anisotropy separates the shear and tilt modes into components parallel and perpendicular to the layers, but overall the results are not qualitatively different to the isotropic case. On the other hand the strongly anisotropic case where the layers are effectively two-dimensional turns out to be considerably more complicated, and will be treated separately in Section 5.3.5.

5.3.4 Vortex Glass

The vortex glass behaviour discussed above applies only to the case of a vortex solid with well defined elastic properties. In Section 5.3.1 it was stated that the elastic properties of the vortex solid are preserved in the presence of disorder even if the long range order is destroyed, a result which is clearly crucial to the existence of the vortex glass state. On the other hand it has also been shown

that the vortex solid can melt into a vortex liquid over a substantial portion of its phase diagram, and in this case the elastic properties of the lattice are destroyed. A description of the way in which the vortex liquid freezes into the vortex glass was first provided by Fisher [43] and subsequently by Fisher, Fisher and Huse [44]. The vortex glass freezing transition is described in terms of two exponents, ν and z. The exponent ν describes the divergence of the vortex glass correlation length ξ_{vg} as the freezing temperature T_g is approached according to

$$\xi_{vg} \propto |T - T_g|^{-\nu} . \tag{5.50}$$

At lengths greater than ξ_{vg} thermal fluctuations upset the scaling behaviour in the activation energy which gives rise to the glassy behaviour. Therefore, at temperatures above T_g where this length remains finite, the activation energy does not diverge at small currents where large distances are probed. The second exponent z characterises the dynamic response of the system according to

$$\tau_{vg} \propto \xi_{vg}^{z} \tag{5.51}$$

where τ_{vg} is the relaxation time of the vortex system which describes the time scale needed for the vortices to search out new metastable states. Combining these two equations with a simple dimensional argument [2, 44] shows that the electric field E should depend on the current according to

$$E \propto \xi_{vg}^{-(z+1)} e_{\pm}(j\xi_{vg}^{D-1}) \tag{5.52}$$

where D is the dimensionality of the system and $e_{+}(j\xi_{vg}^{D-1})$ and $e_{-}(j\xi_{vg}^{D-1})$ are two universal scaling functions relevant for temperatures above T_g and below T_g respectively. At low currents the transition temperature T_g marks the crossover between linear resistivity in the vortex liquid given by $\rho(T) \propto (T - T_g)^{\nu(z+2-D)}$, and non-linear resistivity in the vortex glass given by $\rho(T) \propto \exp^{-c(j_c/j)^{\mu}}$ (c = constant)[18]. As the current is increased the length scale probed (i.e. the distance between the metastable pinning states) becomes smaller than the vortex glass coherence length, and then the electric field has a power law dependence on the applied current. Above T_g the crossover current density separating the linear and the power law behaviour is given by $j_x^{+} \propto (T - T_g)^{\nu(D-1)}$, whereas below T_g the crossover current separating the glassy and power law behaviour is given by $j_x^{-} \propto (T_g - T)^{\nu(D-1)}$. Exactly at $T = T_g$ the current-voltage characteristic shows

[18]Note that the divergence in the activation energy at vanishing current is the same as that derived earlier in the collective creep model (see Equation 5.47).

a power law behaviour at all currents given by $E \propto j^{(z+1)/(D-1)}$.

This approach describes a continuous vortex glass freezing transition in the presence of disorder which is in contrast to the first order melting transition observed in the clean limit. In both cases the melting transition is driven by the thermal fluctuations of the vortices, but in the vortex glass the sharp transition is effectively smoothed by the disorder into a second order transition [2]. A further issue to consider is the relationship between the positions of the clean limit melting line and the vortex glass transition line. As long as the disorder is not too strong, as is generally the case when the pinning is due to random point defects, then the effect on the vibrational modes of the vortex lattice will not be too great[19] [6]. In this case the vortex glass transition temperature will correspond fairly closely with the clean limit melting line. At temperatures close to T_c the vortex glass melting line is predicted to behave as $H_g \propto (T_c - T_g(H))^{2\nu_0}$ with $\nu_0 \simeq \frac{2}{3}$ [44].

The first experimental evidence for the existence of the vortex glass state came from Koch *et al.* [110] who measured the current-voltage characteristic of thin film $YBa_2Cu_3O_{7-\delta}$ samples at several different fields and temperatures. Each data set at constant field was plotted as a function of the coordinates

$$\begin{aligned} \overline{J} &= J\,|1-(T/T_g)|^{\nu(1-D)} \\ \overline{E} &= (E/J)\,|1-(T/T_g)|^{\nu(D-2-z)} \end{aligned} \tag{5.53}$$

to reflect the predicted scaling behaviour of the current and voltage (Equation 5.52). As predicted by the vortex glass theory the scaled curves collapsed neatly onto two functions e_+ and e_- when the values $\nu = 1.7$ and $z = 4.8$ were inserted. Since then similar scaling of the current-voltage curves has been observed in a number of samples including single crystals of $YBa_2Cu_3O_{7-\delta}$ [111] and $Bi_2Sr_2CaCu_2O_{8+\delta}$ [112], $Bi_2Sr_2CaCu_2O_{8+\delta}$ tapes [113], and also a-Mo_3Si films [114], but there is some spread in the values of ν and z used to obtain the scaling [115].

5.3.5 Plastic Deformations and Flux Motion

The above description of thermally assisted flux flow was based entirely on the consideration of elastic deformations of the vortex lattice. It is also possible for

[19] In the opposite case of strong pinning (e.g. by extended defects) the melting line may actually be shifted in position by a considerable amount. For a discussion of this situation see Ref. [6].

flux motion to occur via plastic[20] deformations where some parts of the vortex matter move with greater velocity than other parts so that the vortices actually change sites within the lattice. Several different types of plastic flux flow can be identified, such as "ice-like" and "river-like" motion. Ice-like flux flow occurs when the motion involves large flux bundles moving plastically through the relatively stationary vortex lattice, in a similar manner to which closely packed floating ice moves. River-like or filamentary flux flow is somewhat similar to ice-like flux flow, but it occurs when preferred paths for flux motion exist in the sample. This kind of flow may be caused by the existence of extended defects which channel some of the vortices along river-like paths through the surrounding stationary flux lattice.

These types of flux motion have been observed in several different systems such as two-dimensional a-$MoGe_3$ films [8,9], three-dimensional single crystals of the weakly layered superconductor $NbSe_2$ [11,12,117], and also $YBa_2Cu_3O_{7-\delta}$ crystals with twin boundaries [14]. At low currents the flux creep in these systems is elastic in nature, but at currents close to the critical current j_c the shear stresses induced by the Lorentz force can be great enough to cause weakly pinned regions to tear away from more strongly pinned regions of the flux line lattice. This type of motion is most likely to occur at fields or temperatures close to the melting line where the lattice softens considerably due to a decrease in the shear modulus[21] (see Equation 5.24). The crossover from activated motion to free flux flow which occurs around j_c is therefore not smooth, but instead takes place in an inhomogeneous fashion across the sample leading to steps in the resistance measured as a function of field, temperature or current. The resulting ice-like or river-like flux motion persists until suitably high currents are reached that the entire flux lattice is depinned (see Section 5.3.8 below). At fields or temperatures well below the melting line the flux lattice is much harder, so tearing of the lattice is inhibited and the flux motion remains elastic in nature.

Another more complex type of plastic flux motion may take place through the movement of dislocations in the vortex lattice. A dislocation in the flux lattice can be compelled to move by an applied current in a similar manner to which a dislocation in an atomic crystal can be compelled to move by a strain applied to the crystal [116] (see Figure 5.15). As will be discussed below the activation barriers for this kind of flux motion are relatively small, so thermally activated

[20] A plastic deformation is defined as one where the restoring elastic forces are overcome and a permanent and irreversible change in the lattice positions results [116].

[21] This can also allow the vortices to better accommodate themselves to the pinning potential which leads to an enhancement in the critical current, the so-called "peak effect" [11,12].

creep of dislocations can compete with the modes of elastic vortex motion even at low driving currents. The dislocations themselves may exist in the vortex solid either due to thermal fluctuations of the vortex lines or due to the distortion of the lattice by pinning forces. In both cases the dislocation structures which can exist depend strongly on the dimensionality of the sample, and this in turn affects the resistivity which results from their motion.

In the discussion of the decoupling transition in Section 5.2.5 it was noted that thermally created free dislocation pairs are not thermodynamic objects in strongly coupled layered superconductors i.e. their energy of creation is infinite in a bulk sample. Instead they must be bound in quartets which introduce no net flux into the system, so their motion is not expected to give rise to any dissipation. In a 3D sample the collective pinning theory predicted that disorder leads to the appearance of dislocation loops on length scales greater than R_a [44] (see Marchetti and Nelson [101] for a picture of a dislocation loop), where R_a is the length over which the disorder induced deformation of the vortices becomes greater than the intervortex spacing a_0. However such dislocation loops carry no net flux either, so like the quartets their motion cannot give rise to dissipation. On the other hand recent double sided decoration experiments [118] do provide evidence for the existence of free dislocations in 3D samples, which could presumably move and cause dissipation. It is thought, though, that these dislocations are only metastable remnants of the disordered liquid state which have been frozen in upon cooling below the melting line. An applied current may allow them to move to the edges of the sample, effectively annealing the vortex solid and removing the defects. Of more interest are the recent experiments of Abulafia *et al.* [119] in which magnetisation measurements on three-dimensional $YBa_2Cu_3O_{7-\delta}$ single crystals showed evidence for a crossover from elastic vortex motion at low fields and temperatures to plastic vortex motion involving dislocations at higher fields and temperatures. Interestingly both the elastic and the plastic activation barriers showed a glass-like current dependence.

The situation in two dimensions is somewhat different, because in two dimensions net flux can be introduced into the system by thermally created dislocation-antidislocation pairs (see Figure 5.6). In Section 5.2.4 it was shown that these pairs unbind above a critical temperature T_m^{2D} causing the vortex solid to melt into a vortex liquid. Below T_m^{2D} it is also possible for the bound dislocation pairs to move through the vortex lattice under the influence of an applied current leading to net flux transport and therefore dissipation. The activation barrier which must be overcome to create a dislocation-antidislocation pair can be written as

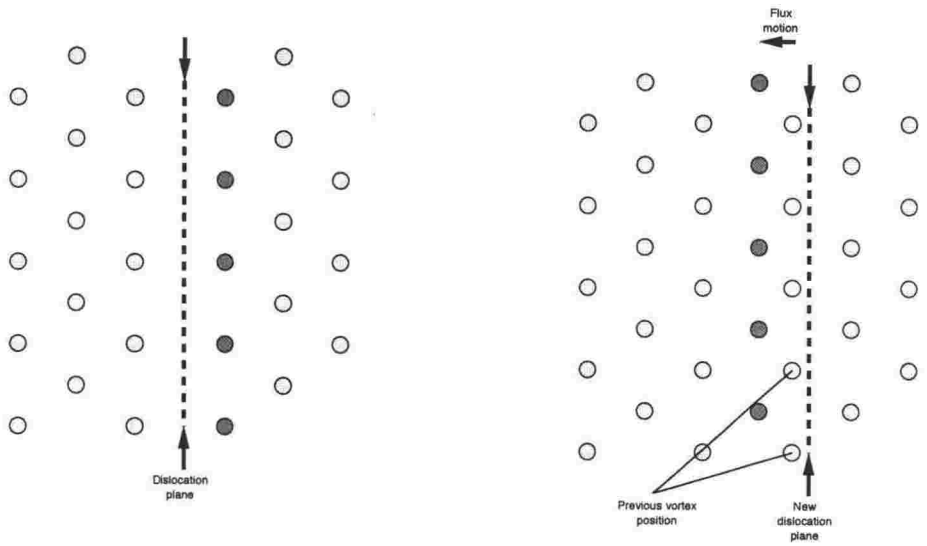

Figure 5.15: A depiction of the motion of a two-dimensional dislocation under the influence of a Lorentz force. In a three-dimensional sample such dislocations appear only as dislocation loops of finite size which carry no net flux.

$$U_p = 2\epsilon_d(r) + 2\mathcal{E}_c \tag{5.54}$$

where $2\epsilon_d(r)$ is the interaction energy of the two dislocations separated by a distance r (see Equation 5.22) and $2\mathcal{E}_c \simeq \Phi_0^2 d_s / 8\sqrt{3}\pi^2 \mu_0 \lambda_{ab}^2$ is the core energy [6, 69,102]. The interaction energy increases with the size of the dislocation pairs so the defect density is dominated by small pairs of approximate size a_0. Feigel'man *et al.* [69] have calculated the thermal concentration of such dislocation pairs and thereby determined the resistivity which results from their motion as

$$\rho(T) \simeq \alpha \rho_{ff} \frac{2T}{T_m^{2D} - T} e^{-2\mathcal{E}_c / k_B T} \tag{5.55}$$

where ρ_{ff} is the flux flow resistivity (Equation 5.30) and α is a numerical factor of the order of 10. The dislocation pairs may also experience a barrier against their motion from the Peierls relief [69] which results from the fact that the dislocation pairs propogate through the lattice in a hopping fashion rather than at a constant velocity (see Figure 5.15). This can be accounted for by adding a factor to the core energy such that $\mathcal{E}_c \rightarrow \mathcal{E}_c + \mathcal{E}_{Peierls}$, although this correction is relatively small and can reasonably be neglected.

In the presence of pinning forces the dislocation pairs will experience a further barrier against their motion on top of the creation and Peierls energies. The pinning barrier for a dislocation of size a_0 is of the order[22] of $\delta U \simeq U_c^0 (a_0/\xi)^{1/2}$ [69],

[22]This estimate is arrived at by considering the collective pinning energy of all of the vortices which must be displaced for the dislocation to move a characteristic distance a_0.

where U_c^0 is the collective pinning energy of a single pancake vortex (Equation 5.34), but generally this pinning barrier is much less than the formation energy $2\mathcal{E}_c$ and can also be neglected. A more important correction to Equation 5.55 comes from the fact that dislocation-antidislocation pairs are also created in finite numbers by the quenched disorder in the sample [120]. Balatskii and Vinokur [121] (see also [102]) have taken an average over the disorder in the vortex solid to determine the resistivity which results from the motion of disorder induced dislocation-antidislocation pairs, leading to

$$\rho_{dis}(T) \simeq \rho_{ff} e^{-8\mathcal{E}_c/\sigma^2 - \sigma/k_B T} \tag{5.56}$$

where $\sigma \simeq U_c^0 (a_0/\xi)^{1/2}$ is the variance of the random pinning potential experienced by the dislocation pair. At low enough temperatures the density of disorder induced defects will become equivalent to the thermally created density, at which point Equation 5.56 for the resistivity will take over from Equation 5.55.

Finally, in the presence of disorder there is also the possibility of the creation of unbound dislocations even below the BKT melting line [69]. A dislocation displaces the vortices around it by an amount which decreases with the distance from the dislocation. Beyond a distance $R_0 \simeq a_0^2/\xi$ the displacement of the vortices becomes less than the scale ξ of the pinning potential, so that the vortex positions are dominated by the quenched disorder rather than the thermally created dislocations. Thus, collectively pinned bundles at distances greater than R_0 from the dislocation are not affected by the dislocation, effectively cutting off the logarithmic interaction between dislocation pairs at a distance $R_0 + R_c^{2D}$ where R_c^{2D} is the two-dimensional collective pinning length. The cutoff means that the energy needed to create a free dislocation is now finite and given by

$$U_{dis} \simeq \frac{\Phi_0^2 d_s}{16\pi^2 \mu_0 \lambda_{ab}^2(T)} \ln\left(\frac{R_c^{2D}}{a_0} + \frac{a_0}{\xi}\right). \tag{5.57}$$

Dislocations separated by less than $R_0 + R_c^{2D}$ will still interact in the usual manner and remain bound below T_m^{2D}, but when the disorder is strong so that $R_c^{2D} \simeq a_0$ most of the dislocations will be unbound. In this case the substitution $(R_c^{2D}/a_0 + a_0/\xi) \approx a_0/\xi \propto \sqrt{(1/H)}$ can be made and the activation energy for the creation of a free dislocation is

$$U_{dis} \simeq \frac{\Phi_0^2 d_s}{32\pi^2 \mu_0 \lambda_{ab}^2(T)} \ln\left(\frac{H_0}{H}\right). \tag{5.58}$$

where $H_0 \simeq H_{c2}$ is a characteristic field at which U_{dis} goes to zero. An activation energy of this form has been observed in a variety of a-MoGe films with a

high degree of disorder in the vortex lattice [23,25], and also in very anisotropic multilayers of $YBa_2Cu_3O_7/PrBa_2Cu_3O_7$ [27].

The most important thing about plastic flux creep is the fact that it destroys the vortex glass behaviour in two dimensions [69,102]. While the barriers against elastic flux motion diverge at low currents in both two and three dimensions[23], the plastic barriers associated with dislocation mediated flux creep remain finite in two dimensions, leading to a non-zero linear restivity even at the lowest currents. These ideas have been developed into a two-dimensional vortex glass model [44] in which the vortex glass phase transition occurs only at $T = 0$. The two-dimensional vortex glass correlation length diverges as $T = 0$ is approached according to $\xi_{vg}^{2D} \propto 1/T^{\nu_{2D}}$ with the predicted value for the exponent ν_{2D} equal to 2 [44]. Plastic vortex motion gives rise to a linear restivity at low currents until the length scale probed by the current becomes smaller than ξ_{vg}^{2D}, or equivalently until the (current dependent) elastic activation energy becomes less than the plastic activation energy. The current density above which non-linear resistivity sets in is given by

$$J_{nl} \approx k_B T/\Phi_0 \xi_{vg}^{2D} \propto T^{1+\nu_{2D}}. \tag{5.59}$$

This differs from the corresponding prediction in the Anderson-Kim flux creep model where the non-linearity sets in when the argument of the sinh function in Equation 5.42 becomes of the order of unity, yielding $J_{nl} \propto T$. Below J_{nl} the resistivity associated with the motion of dislocation pairs varies with temperature according to

$$R \propto \exp\left[-(T_0/T)^p\right] \tag{5.60}$$

with T_0 a characteristic temperature and p a constant of the order of unity. In the two-dimensional vortex glass model the BKT melting transition still takes place (see Section 5.2.4), but unlike the transition in three dimensions the two-dimensional melting transition does not mark the boundary between the liquid and the glass. Instead the BKT melting line marks only a transition from the vortex liquid to a stronger pinning state in the vortex solid where the resistivity is due mainly to the motion of dislocation-antidislocation pairs. A crossover from three-dimensional to two-dimensional vortex glass behaviour has been observed by Dekker *et al.* [123] as the thickness of a series of $YBa_2Cu_3O_{7-\delta}$ films was

[23]The two-dimensional glassy exponents μ actually differ from the corresponding three-dimensional values (Equation 5.49) [122], but as the glassy behaviour is cut off by plastic vortex motion in two dimensions the exact values of the exponents are not experimentally accessible.

decreased from 3000 Å to 16 Å. The scaling form

$$\frac{E}{J}\exp\left[\left(\frac{T_0}{T}\right)^p\right] = \mathcal{G}\left(\frac{J}{T^{1+\nu_{2D}}}\right) \tag{5.61}$$

was used to collapse the data from the thinnest sample onto a single universal curve, thus demonstrating the growth of the two-dimensional vortex glass coherence as the temperature decreases towards zero. More recently Wen *et al.* [124] have observed similar behaviour at high fields in $Tl_2Ba_2CaCu_2O_8$ thin films.

5.3.6 Flux Motion in the Vortex Liquid

It was assumed above that in the vortex liquid the activation barriers go to zero and the resistivity is given simply by Equation 5.30 for free flux flow. The motivation for this assumption is the fact that in the liquid the thermal disorder of the vortices is expected to completely average out the pinning forces, however just above the melting line this assumption does not neccessarily hold. To see why this should be it is neccessary to consider in more detail the difference between the vortex liquid and the vortex solid.

The vortex solid has an inhomogeneous structure which interacts with the pinning forces to yield a non-zero critical current. In the vortex liquid, on the other hand, the shear modulus goes to zero so there is no long range order in the vortex structure. The thermal disorder in the liquid means that the vortices average out the pinning forces and the critical current for vortex motion is zero. Just above the melting line, however, where the thermal energy is only slightly greater than the elastic energy, the vortex liquid is very viscous in nature so that it preserves its structure on short time scales. As long as the time scale over which order persists is longer than the characteristic time scale over which the vortices interact with the pinning potential then the vortex liquid will not completely average out the pinning[24]. The effectiveness of pinning in the vortex liquid just above the melting line leads to a thermally activated resistivity rather than free flux flow [125].

A possible origin of the high viscosity lies in the barriers against plastic deformation which stem from the entangled nature of the 3D vortex liquid [80]. In the entangled vortex liquid the flux lines are effectively braided together such that in order to move a flux line must cut through other vortices. This leads to a finite shear viscosity which (at low frequencies) behaves in a similar manner to the shear modulus of the vortex solid [6, 126]. The plastic motion can be considered

[24]Note the similarity between this line of argument and the consideration of the divergence of the relaxation time (Equation 5.51) in the vortex glass model.

to occur through the addition of vortex loops to the flux lines of approximate size equal to the lattice constant a_0 (see Figure 5.12), thereby transferring the vortex segment to a new lattice site. The relevant plastic activation barrier U_{pl} has been calculated [125,127] to be

$$U_{pl} \simeq \frac{\Phi_0^2 a_0}{2\pi\mu_0\gamma\lambda_{ab}^2(T)} \propto \frac{T_c - T}{H^{1/2}}. \tag{5.62}$$

An alternate explanation for the plastic activation energy has been suggested by Tinkham [128] where the barrier is related to the energy required to slide a row of flux lines past an adjacent stationary row. The minimum number of flux lines which must be moved scales as a_0^2 leading to an activation energy of the form

$$U_{pl} \simeq \frac{\beta H_c^2(T)\xi_{ab}(T)\Phi_0}{B} \tag{5.63}$$

where β is a parameter of order unity. Note that the plastic activation barrier itself is not enough to ensure a thermally activated resistivity, but pinning must be involved to prevent the entire viscous liquid from moving at the flux flow velocity.

As the temperature increases the vortex liquid becomes less viscous so that the time scale over which the vortex structure persists is no longer greater than the characteristic pinning time. The thermal disorder then averages out the pinning forces and the usual flux flow resistivity results. In the two-dimensional case where the melting transition is mediated by the unbinding of dislocation pairs the activated motion in the vortex liquid corresponds to the plastic motion of the unbound dislocations.

5.3.7 Parallel Fields

It has already been shown in Section 5.3.1 that the critical currents can be strongly enhanced by the intrinsic pinning of the layered structure. In this section a brief discussion will be given of the manner in which the vortices move under the influence of an applied current when the field is directed parallel to the ab plane. Attention will be restricted to the case where the current also lies in the ab plane so that the Lorentz force on the vortices is along the c direction.

Ivlev and Kopnin [129,130] have examined the parallel field creep of vortices in the case of relatively weak anisotropy and have obtained the relevant activation barriers. At low current densities they find a glassy response (i.e. $U \propto (j_c/j)^{\mu}$) with the exponent μ equal to 1. At high currents the activation barrier is of the Anderson-Kim form described above with a linear current dependence.

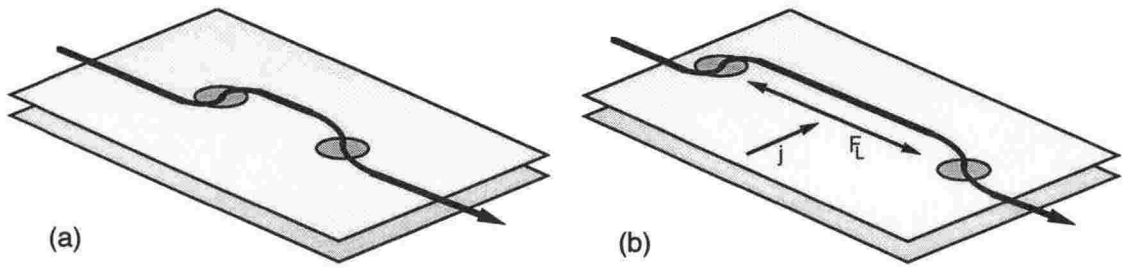

Figure 5.16: The parallel field thermally activated hopping process in a strongly layered superconductor. (a) A double kink structure which provides the hopping nucleus. The dark circles represent pancake vortices cutting through the superconducting layer. (b) The current forces the pancake vortices in the double kink apart causing the entire vortex line to be transferred to the next layer.

In the opposite case of strong anisotropy Chakravarty *et al.* [131, 132] have shown that rather than a vortex loop the optimal hopping unit is better described in terms of a double kink structure as shown in Figure 5.16(a). This can be thought of as a pair of oppositely charged pancake vortices connected by Josephson strings, somewhat similar to the vortex-antivortex pairs described in connection with the zero field BKT transition in Section 5.2.2. The addition of the double kink transfers part of a vortex or vortices into the next layer. Because motion of the vortices is easiest within the planes the current then acts on the portion of the vortex loop directed perpendicular to the layers, causing the loop to grow along the field direction until the entire flux line has been transferred to the next layer (see Figure 5.16(b)). Once again the current dependence is found to be glassy with an exponent $\mu = 2$.

5.3.8 High Current Regimes

The above sections have provided an extensive review of current driven vortex motion for all currents up to the critical current j_c. As the current approaches j_c the vortices approach the flux flow regime, although the pinning forces still give rise to some disorder in the moving vortex lattice. Koshelev and Vinokur [133] investigated the behaviour of these defects in two dimensions as the vortex velocity increases in response to higher and higher currents. They noted that, in a similar manner to the thermal depinning discussed above (Section 5.3.2), as the vortices move faster they tend to average out the pinning forces. The vortex velocity therefore acts like a finite "shaking temperature", and at a certain velocity the pinning forces are averaged out completely and the defects in the vortex lattice heal. Koshelev and Vinokur referred to this as a "crystallisation transition". Evidence for an increased ordering of the vortex lattice at high driv-

ing currents has been observed in thin films of Mo_3Ge [8,9] and also in single crystals of $NbSe_2$ [13,117].

5.3.9 Larkin-Ovchinnikov Instabilities

A much more dramatic transition in the rapidly moving vortex system has been predicted in both two and three dimensions by Larkin and Ovchinnikov (LO) [15, 16]. LO investigated the effects of the electric field produced by the moving vortices in the flux flow regime, where the vortex velocity is determined by the balance between the driving Lorentz force and the vortex viscosity[25]. They found that the electric field shifts the nonequilibrium distribution of quasiparticles in the vortex core to higher energies, causing some of the quasiparticles to escape into the surrounding superconductor. This in turn causes the vortex core to shrink and the viscuous drag coefficient η is reduced according to the formula

$$\eta(v) = \frac{\eta(0)}{1 + (v/v^*)^2} \tag{5.64}$$

where v is the vortex velocity, $\eta(0)$ is the damping coefficient at $v = 0$ and v^* is the critical vortex velocity at which the maximum damping force ηv^* occurs. Any increase in velocity past the critical value causes a reduction in the damping force, further perpetuating the velocity increase and thus the vortex system becomes unstable at the critical velocity. The critical velocity is determined by the formula

$$v^{*\,2} = \frac{D[14\zeta(3)]^{1/2}(1 - T/T_c)^{1/2}}{\pi \tau_{in}} \tag{5.65}$$

where $D = (v_f \ell)/3$ is the quasiparticle diffusion coefficient with v_f the Fermi velocity and ℓ the electron mean free path, τ_{in} is the inelastic-scattering time of the quasiparticles and $\zeta(3) = 1.202$ is the Riemann ζ function of 3. It should be noted that this critical vortex velocity and the current I^* where it occurs are expected to be independent of the applied field H. The voltage when the instability occurs is related to the critical vortex velocity by

$$V^* = \mu_0 v^* H L \tag{5.66}$$

where L is the length between the voltage probes.

The original LO instability theory predicted a field and current independent critical vortex velocity v^*, however finite heating effects in the vortex core at the high vortex velocities required to observe the instability have been predicted to

[25]The origin of the finite viscosity was discussed briefly at the start of Section 5.3.

cause a decrease in the observed value of v^* as the field is increased [134]. The degree to which the measured v^* is affected depends critically on the rate at which heat can be removed from the cores. A similar field dependence of v^* has also been predicted by Doettinger *et al.* [135], but in this case the prediction is related to the lack of spatial homogeneity in the quasiparticle distribution due to the discreteness of the vortex cores. At low fields H the field dependence of the critical vortex velocity is predicted to behave as $H^{-1/2}$. As the field increases the intervortex spacing a_0 becomes smaller than the distance travelled by the vortices over a time equal to the electron inelastic scattering time, so the quasiparticle distribution is effectively homogeneous and the critical vortex velocity is no longer field dependent.

LO instabilities have been observed in a variety of systems including highly disordered thin films of Al, In, and Sn [136, 137], $YBa_2Cu_3O_{7-\delta}$ films [135, 138, 139], $Bi_2Sr_2CaCu_2O_{8+\delta}$ films [140] and a-Mo_3Si films [35]. Qualitative agreement with the predictions of Equation 5.65 have been observed in one of the Ta/Ge multilayer samples studied here where the inelastic scattering time τ_{in} was determined independently from the normal state resistivity [141]. This sample is discussed in Section 6.4. In all cases the samples which exhibit LO instabilities have a high degree of electronic disorder and a short inelastic scattering time so that the critical vortex velocity is experimentally accessible.

5.4 Summary

This extensive discussion of the theoretical predictions relating to the behaviour of type-II superconductors in a magnetic field has highlighted the complexity of the vortex phases. In the next chapter these theoretical models will be applied to the data from the Ta_xGe_{1-x}/Ge multilayers in order to try to understand the relationships between the vortices and the various parameters characterising the multilayers.

Chapter 6

Results and Discussion

As mentioned in Chapter 1 amorphous Ta_xGe_{1-x}/Ge multilayers represent an ideal system in which to study the magnetic phase diagram of layered superconductors with variable anisotropy. In particular such a study gives considerable insight into the role of the layered structure in determining the superconducting properties of the high-T_c cuprates. This chapter presents the main results obtained from the investigation of the Ta_xGe_{1-x}/Ge multilayer system, starting with the determination of the upper critical fields of the samples and the relevant superconducting lengths. Following this the vortex states are investigated for samples with a wide range of layer thicknesses, and finally special attention is paid to the behaviour of the vortices in the presence of high driving currents.

6.1 Fluctuation Conductivity and Critical Fields

In this section a detailed analysis of the fluctuation conductivity is used to determine $H_{c2\perp}$, and from this the in-plane coherence length ξ_{ab} and the in-plane penetration depth λ_{ab} of each of the samples are obtained based on the theoretical models presented in Section 5.1. The out-of-plane values ξ_c and λ_c are similarly obtained from $H_{c2\parallel}$, and the ratio of the in-plane and out-of-plane coherence lengths is used to define the anisotropy γ.

Figure 6.1 shows plots of the zero field resistive transitions of some of the most carefully studied samples. The approximate fractional width of the transition[1] $\Delta T_c/T_c$ varies between 0.013 and 0.17, with the broadest transitions tending to correspond to the samples with the thinnest superconducting layers. This shows that an accurate determination of T_c cannot be made by inspection only, as the

[1] ΔT_c is measured between 10% and 90% of the normal state resistance, and an initial estimate of T_c is taken from the midpoint of the transition.

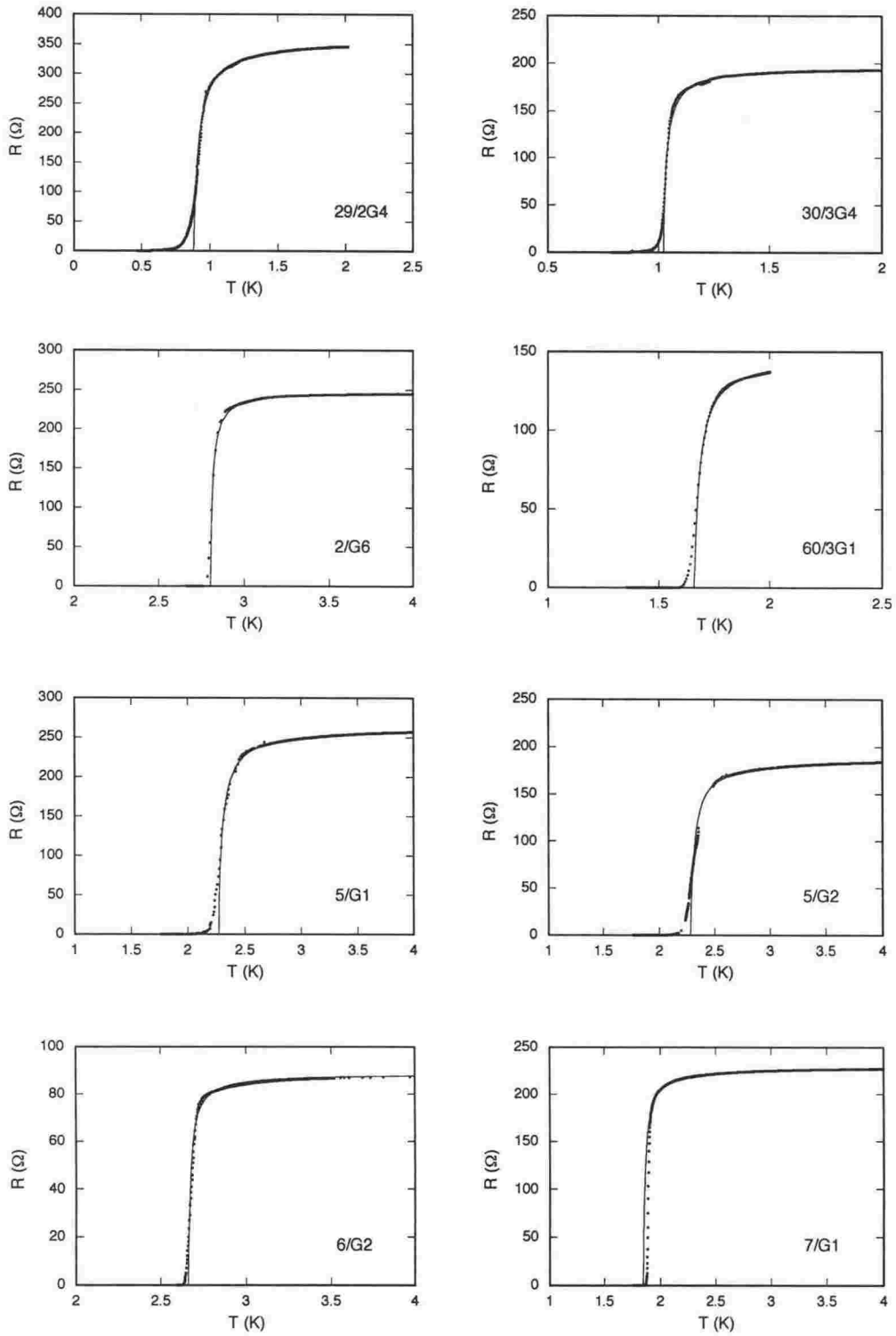

Figure 6.1: The resistive transition of a selection of the samples in zero applied magnetic field. The solid lines are fits to the two-dimensional zero field fluctuation conductivity.

results depend on the criteria used; for example the zero resistance point can differ from the top of the transition by more than 17%. To gain a better understanding of the transition the fluctuation conductivity of each of the experimental data sets has been fitted to the theoretical forms given in Equations 5.13 and 5.14, as shown by the solid curves in Figure 6.1. To obtain the normal state resistivity in the fluctuation regime the resistivity at higher temperatures has been extrapolated back towards zero. The temperature coefficient of the resistivity is very small for these highly disordered samples (between -0.1 and $-0.5\,\Omega/K$) [17], so the normal state resistivity actually changes very little around the transition region.

Both the 2D and 3D forms for the fluctuation conductivity were fitted to each curve, with T_c and the coefficient of the temperature dependence the free parameters (see Equations 5.13 and 5.14). At high temperatures there is little difference between the two fits, but in almost every case the 2D form fitted better at temperatures close to T_c so only the 2D fits have been included in Figure 6.1. This can be understood by noting that at zero temperature the length scale of the fluctuations ξ_{ab} is about the same size as the thickest superconducting layers (see below), and diverges as T_c is approached, so the samples are not three-dimensional with respect to the individual layers at these temperatures.

Figure 6.1 also shows that in most cases the measured resistivity deviates from the fitted curve as the resistivity approaches zero, with the measured value going to zero much more slowly than the fitted value. This behaviour is expected due to the Berezinskii-Kosterlitz-Thouless transition which occurs in two-dimensional samples (see Section 6.2 below). One notable exception to this rule is sample 7/G1 in which the 2D fluctuation conductivity form fits extremely well at temperatures above about 2 K, but the measured resistance actually goes to zero faster than the fitted curve. Sample 7/G1 has moderately coupled superconducting layers, so it is likely that the observed behaviour is due to a 2D to 3D crossover occurring as the perpendicular coherence length $\xi_c(T)$ increases beyond the interlayer spacing as the temperature approaches T_c. The 3D form for the fluctuation conductivity does indeed fit this sample well close to T_c, and although the data range is very small so that the fitted coefficient of the temperature dependence is highly uncertain, the 3D fit probably gives a better estimate of T_c than the 2D fit. The samples 60/3G1 and 60/3G4 which also have fairly strongly coupled superconducting layers do not show this behaviour, possibly because of their thinner superconducting layers, or perhaps due to the presence of a higher degree of inhomogeneity in these samples which broadens the transition slightly. The single layer alloy sample 2/G6 has a thickness of approximately 600 Å which is considerably greater than $\xi_{ab}(0)$, however it does not fit the 3D form close to

Sample	T_c (K)	Fitted Slope ($\times 10^{-5}\,\Omega^{-1}$)
29/2G4	0.882	3.0
30/3G4	1.021	6.3
32/2G1	-	-
33/1G4	1.162	0.8
36/2G1	1.440	0.3
60/3G1	1.661	1.8
60/3G4	1.825	0.6
2/G6	2.802	9.6
5/G1	2.267	2.0
5/G2	2.280	3.3
6/G2	2.662	3.0
7/G1	1.850 (1.886)	1.1

Table 6.1: Parameters derived from the fitting of the zero field fluctuation conductivity to the theoretical forms given in Equations 5.13 and 5.14. The T_c values are from the fit to the 2D form of the fluctuation conductivity except for sample 7/G1 where the 3D value has also been included in parenthesis. The fitted slopes, which are also all from the 2D fits, are all reasonably close to the theoretically predicted value of 1.5×10^{-5}.

T_c either. This is because close to T_c the coherence length grows rapidly so that it exceeds the total layer thickness, and the sample is only three-dimensional well above T_c where either form for the fluctuation conductivity fits fairly well.

The results from the fitting are displayed in Table 6.1. No values are recorded for sample 32/2G1 because it showed a clear double transition indicating a very strong degree of inhomogeneity in the sample. Only the T_c values from the fits to the 2D fluctuation conductivity are shown, except for sample 7/G1 where the value from the 3D fit is also shown in parenthesis. The fitted coefficient of the temperature dependence of the 2D fluctuation conductivity (the "slope") is also included, which can be compared with the value $e^2/16\hbar = 1.5 \times 10^{-5}\,\Omega^{-1}$ predicted[2] by Equation 5.13. Note that the fitted value of the slope has been modified to take account of the number of layers and the area of the conduction path. Considering the fact that the quality of the fit is not especially sensitive to the value of the slope the agreement is quite reasonable, with all of the fitted values falling within an order of magnitude of the expected result. Overall the fitting of the zero field fluctuation conductivity gives a consistent determination of the T_c of each of the samples, and shows that the simple Aslamasov-Larkin form for the fluctuation conductivity describes these highly disordered samples quite well.

Now that the T_c values of each of the samples have been determined from the zero field fluctuation conductivity the scaling forms presented in Equations 5.15 and 5.16 can be applied to the in-field data to determine the upper critical fields of the samples. In two-dimensional samples $H_{c2\perp}$ is predicted to be linear in temperature only for a field perpendicular to the layers (see Section 5.1), so the perpendicular upper critical field of each of the samples will be considered first followed by a separate treatment of the parallel upper critical fields. Figures 6.2(a) and 6.2(b) show the resistive transitions as a function of temperature for samples 6/G2 and 7/G1 respectively, with each curve corresponding to a different perpendicular applied field. The transitions for each of the other samples are qualitatively similar to the two shown, with the most striking feature being the field induced broadening of the resistive transition which results from vortex motion below $H_{c2\perp}$. The maximum amount of broadening tends to correspond to the samples with the thinnest and least strongly coupled superconducting layers. This broadening makes a determination of the upper critical field from the resistive transition even more difficult than in the zero field case, necessitating

[2]The expected value does not include the superconducting layer thickness d_s because in a thin film of finite thickness the experimentally measured quantity is $\sigma' d_s$ rather than the actual 2D conductivity σ' [2].

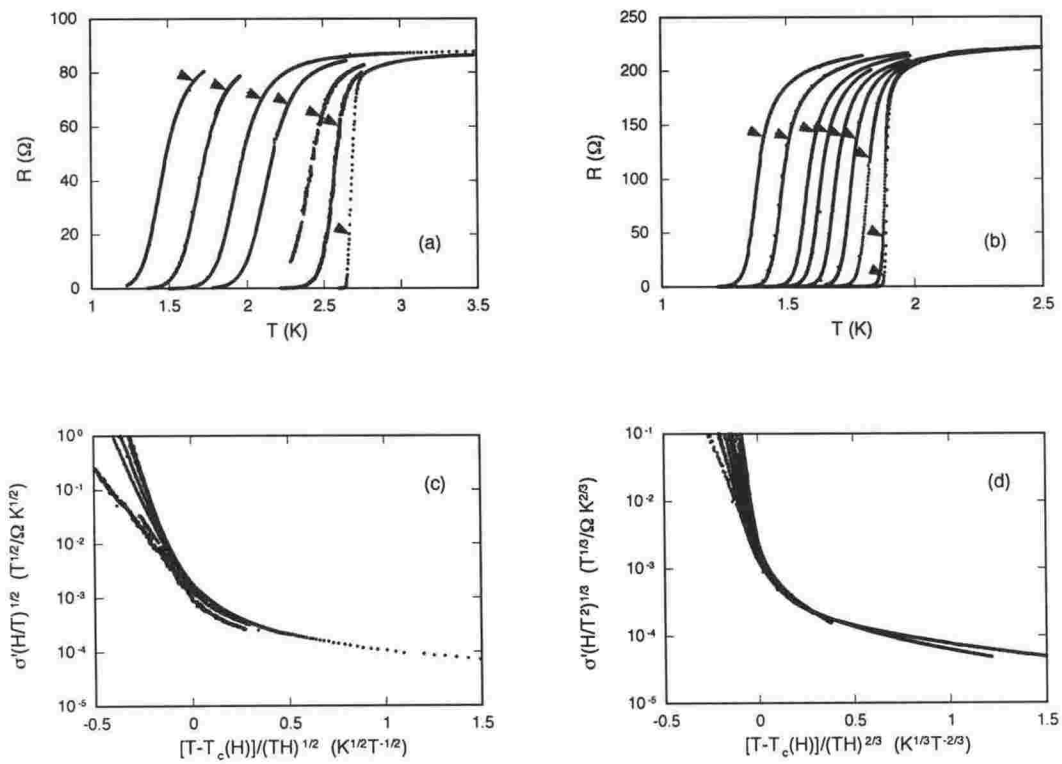

Figure 6.2: (a) Resistive transitions in a perpendicular applied field for sample 6/G2. From right to left the curves correspond to fields of 0, 0.1, 0.3, 0.7, 1.0, 1.4 and 1.8 T. (b) Resistive transitions in a perpendicular applied field for sample 7/G1. From right to left the curves correspond to fields of 0, 0.003, 0.1, 0.2, 0.3, 0.4, 0.5, 0.7 and 0.9 T. (c) The data from sample 6/G2 transformed according to the 2D fluctuation conductivity scaling laws. (d) The data from sample 7/G1 transformed according to the 3D fluctuation conductivity scaling laws. The arrows on (a) and (b) indicate the position of $H_{c2\perp}$ determined from the scaling parameters.

the fitting of the fluctuation conductivity to obtain meaningful results.

In a similar manner to the analysis of the zero field data both the 2D and 3D scaling forms for the in-field fluctuation conductivity (Equations 5.15 and 5.16) have been applied to resistance data obtained both by sweeping the field at constant temperature and by sweeping the temperature at constant field. The normal state resistivity was determined from the data at higher temperatures in the same manner as described above. Since T_c has already been determined the only free parameter in both the 2D and 3D scaling is $S_\perp$, the slope of the upper critical field at $T = T_c$. The 2D form of the scaled fluctuation conductivity of sample 6/G2 is displayed in Figure 6.2(c), and the 3D form of the scaled fluctuation conductivity of sample 7/G1 is displayed in Figure 6.2(d). In both cases the collapse of the data onto a single curve is quite convincing except at values below zero on the x-axis where the resistivity is affected more by vortex motion than by fluctuation effects. As was the case with the zero field results sample

7/G1 showed better agreement with the 3D scaling form than the 2D form. Samples 60/3G1 and 60/3G4 showed similar scaling behaviour under either scaling form with the same value for $S_\perp$, although in either case there was considerable spread in the scaled data. All of the other samples were better described as two-dimensional.

While the scaling theory seems to describe the fluctuation conductivity in a perpendicular field quite well some further comments are required regarding the validity of the analysis and the relationship between $H_{c2\perp}$ and the resistive transition. The theory is strictly valid only in the lowest Landau level approximation which holds only at high fields, however, as noted by Ullah and Dorsey, inclusion of the higher Landau levels will not greatly alter the scaling forms [58, 59]. The experimental results here show that the scaling is not significantly changed by exclusion of the data from the lowest fields, so the relaxation of the lowest Landau level requirement does not seem to affect the quality of the determination of $H_{c2\perp}$.

To determine the relationship between the resistive transitions and $H_{c2\perp}$ the position of the upper critical field has been marked as an arrow on each curve in Figures 6.2(a) and 6.2(b). At higher fields $H_{c2\perp}$ is seen to lie at a point close to the top of the transition where the resistance starts to turn downwards rapidly, a trend which is repeated in all of the samples. This shows that the in-field resistive transition is determined by motion of the magnetic vortices over most of its width. As the field approaches zero vortex motion no longer affects the shape of the transition, so the position of $H_{c2\perp}$ tends to correspond to a much lower resistance. In the samples with the highest T_c, and in the samples which were investigated in the dilution refrigerator so that temperatures well below T_c could be achieved, the scaling of the perpendicular field fluctuation conductivity is less convincing at the lowest temperatures. This is in agreement with the Werthammer, Helfand and Hohenberg theory (see Section 5.1.3) which showed that the upper critical field at low temperatures lies below the extrapolated high temperature behaviour, so the linear approximation to $H_{c2\perp}$ should not be used.

The degree to which the data collapse onto a single curve under the appropriate scaling law depends on the sample, with some samples showing a larger degree of scatter about the scaled curve than others. This is most likely due to the differing degrees of inhomogeneity, however in all cases it was possible to unambiguously determine the optimal scaling parameters to within a reasonable uncertainty. The results of the scaling fits to the perpendicular field fluctuation conductivity are summarised in Table 6.2, where the uncertainty in $S_\perp$ represents the range over which it could be varied without significantly upsetting the scal-

Sample	$S_\perp = -\frac{dH_{c2}}{dT}\Big\|_{T=T_c}$	$\xi_{ab}(0)$ (Å)	$\lambda_{ab}(0)$ (Å)	κ
29/2G4	2.1±0.2	133±6	17000±3000	80±20
30/3G4	1.9±0.1	130±3	16000±3000	70±10
32/2G1	-	-	-	-
33/1G4	-	-	20000±3000	-
36/2G1	-	-	19000±3000	-
60/3G1	1.9±0.1	102±3	12000±2000	70±10
60/3G4	1.8±0.1	100±3	11000±2000	70±10
2/G6	2.1±0.3	75±5	11000±2000	90±20
5/G1	2.1±0.3	83±6	11000±2000	80±20
5/G2	2.2±0.1	81±2	11000±2000	90±10
6/G2	1.8±0.1	83±2	11000±2000	80±10
7/G1	1.9±0.1	96±3	14000±2000	90±20

Table 6.2: Parameters derived from the scaling of the perpendicular field fluctuation conductivity.

ing behaviour. The values determined for $S_\perp$ can be compared to the theoretical prediction [142]

$$S_\perp = \frac{8k_B}{2\pi eD} \tag{6.1}$$

where D is the electron diffusion coefficient which has been determined for pure Ta/Ge multilayers to be about $10^{-4}\,\mathrm{m^2 s^{-1}}$ [17]. Insertion of the values yields $S_\perp \approx 1\,\mathrm{T/K}$, in reasonable agreement with the measured values considering the large uncertainty in D. $S_\perp$ has also been used to determine the in-plane coherence length $\xi_{ab}(0)$ by extrapolating $H_{c2\perp}$ back to $T = 0$ according to

$$\xi_{ab}^2(0) = \frac{\Phi_0}{2\pi T_c S_\perp}. \tag{6.2}$$

Finally the in-plane penetration depth λ_{ab} has been determined from the relationship [142]

$$\lambda_{ab}(0) = 1.05 \times 10^{-3} \left(\frac{\rho_0}{T_c}\right)^{1/2} \tag{6.3}$$

where ρ_0 is the normal state resistivity extrapolated back to $T = 0$. The values of $\xi_{ab}(0)$ and $\lambda_{ab}(0)$ are included in Table 6.2, along with the value of the Ginzburg–Landau parameter at temperatures close to T_c determined[3] from $\kappa = \lambda_{ab}(0)/1.63\xi_{ab}(0)$ [142].

The determination of $H_{c2\|}$ from the fluctuation conductivity is somewhat more complicated. For samples with strongly coupled superconducting layers $H_{c2\|}$ is still expected to be linear in temperature close to T_c and the scaling analysis can therefore be applied. For more anisotropic samples $H_{c2\|}$ is not linear but instead shows a square root dependence on the temperature (Equation 5.10), which at least necessitates a modification to the way in which the upper critical field is inserted into the scaling laws. Furthermore the scaling laws have been developed in such a way that the dimensionality is determined by the thickness of the superconducting layers in the direction of the applied field. In a parallel field, however, the superconducting layers may be extremely thin but still be extensive in the field direction, so the dimensionality of the fluctuations is not so simply related to the layer thickness. Finally, the presence of thick insulating layers tends to allow the magnetic field to be screened completely from the superconducting layers, so that the multilayer is effectively transparent to a parallel field. These facts mean that the fluctuation conductivity scaling laws should be applied to

[3]The factor 1.63 arises due to the fact that the zero temperature values for λ_{ab} and ξ_{ab} have been used to get the value of κ close to T_c.

parallel field data with some caution, as the validity of the theory is questionable in the case of strongly decoupled layers.

Before analysing the parallel field data it is also important to consider the possible effects of any misalignment of the field. For the samples measured in the dilution refrigerator the field was directed along the axis of the fridge unit, and careful mounting of the samples meant that the misalignment was less than 1°. To align the field with the layers in the other systems a finite field was applied to induce some resistance in the sample which was then rotated in order to find the position of minimum resistance. This position was assumed to correspond to the parallel field orientation, and could be determined with an accuracy of better than 0.2° (note that this allows an equally accurate determination of the perpendicular direction). The perpendicular component is therefore less than 2% of the parallel applied field in the dilution refrigerator and less than 0.4% of the parallel applied field in the other systems.

Figures 6.3(a) and 6.3(b) show the resistive transitions as a function of temperature in a parallel applied magnetic field for samples 6/G2 and 7/G1 respectively. Figure 6.3(c) shows the resistive transitions as a function of the parallel applied field at fixed temperature for sample 60/3G4. It can be seen that the critical fields are considerably higher than they were for the same samples in the perpendicular field orientation. An attempt has been made to scale the parallel field fluctuation conductivity for all of the samples where data was available, however only for sample 7/G1 could a convincing collapse of the data be obtained using a linear form for $H_{c2\|}$. Once again the 3D form for the scaling laws provided better scaling than the 2D form for this sample. The fact that the parallel field transitions of sample 7/G1 can be scaled shows that $H_{c2\|}$ fits the anisotropic Ginzburg–Landau model, as expected for a sample with thin insulating layers. Both $H_{c2\|}$ and $H_{c2\perp}$ for this sample are shown in Figure 6.3(e). The value 11 ± 1 obtained for $S_{\|}$ can be used to define the anisotropy according to Equation 5.7 which yields $\gamma = 5.8 \pm 0.8$.

The other samples with strongly coupled superconducting layers are 60/3G1 and 60/3G4, and possibly 33/1G4 and 36/2G1 although there was no perpendicular field data for the latter two. Application of the 3D scaling laws to the data from 60/3G1 and 60/3G4 showed some signs of a scaling collapse with $S_{\|} = 3.0 \pm 0.2$, but there was a considerable amount of spread in the scaled data, particularly at low temperatures. It was noted, however, that the parallel field transition curves of sample 60/3G4 show much less broadening than in the perpendicular case, so the critical field can be extracted directly from the data by defining $H_{c2\|}$ to be the steepest point on the transition. Although this defini-

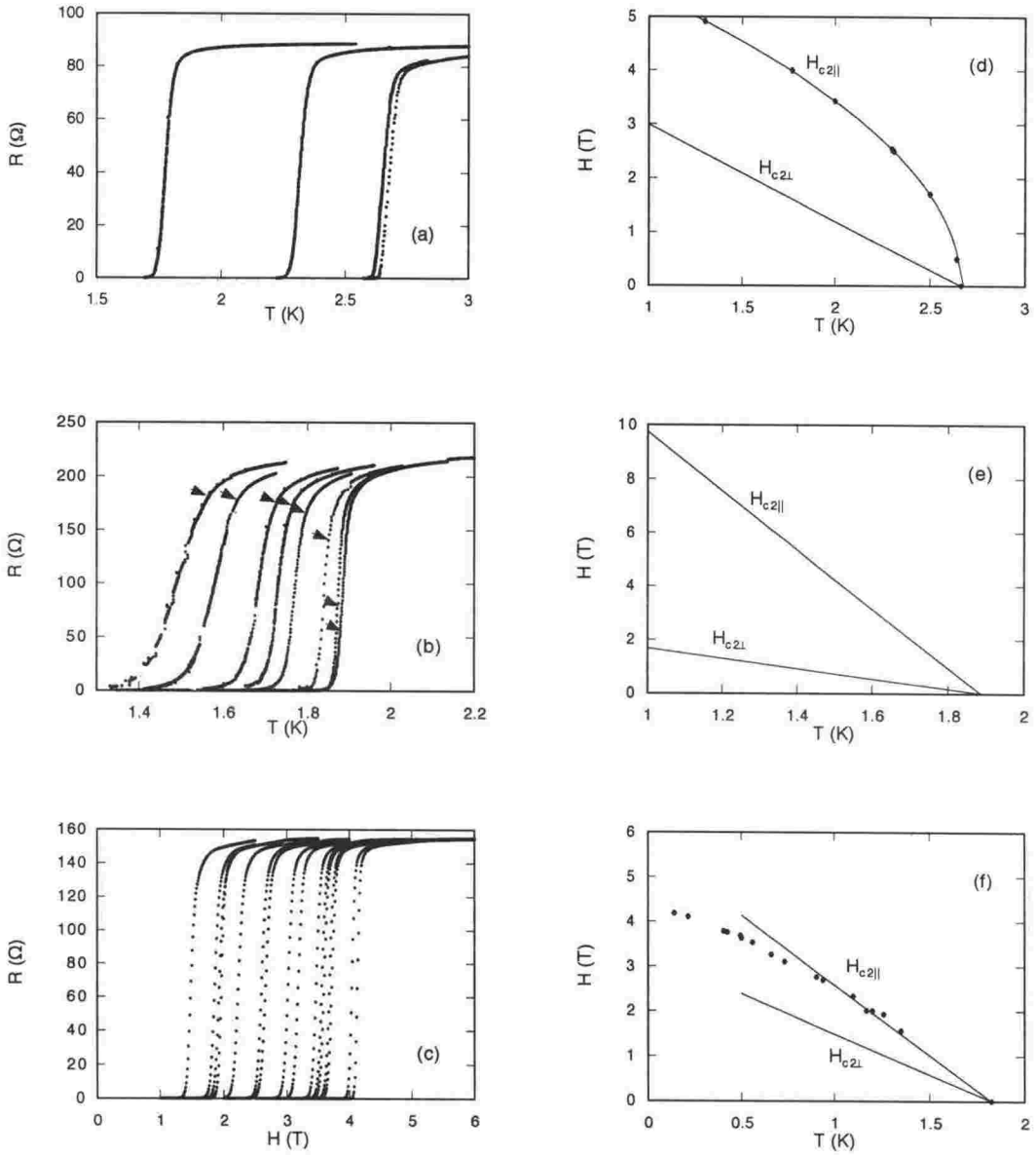

Figure 6.3: (a) - (c) Resistive transitions in a parallel applied field. (a) Sample 6/G2. From right to left the curves correspond to fields of 0, 0.5, 2.5 and 4.0 T. (b) Sample 7/G1. From right to left the curves correspond to fields of 0, 0.2, 0.5, 1.0, 1.5, 2.0, 3.0 and 4.0 T. The arrows mark the position of $H_{c2||}$. (c) Sample 60/3G4. From right to left the curves correspond to temperatures of 0.14, 0.215, 0.405, 0.425, 0.495, 0.5, 0.56, 0.66, 0.73, 0.905, 0.94, 1.1, 1.17, 1.2, 1.26 and 1.35 K. (d) - (e) Upper critical fields. (d) Sample 6/G2. The solid line through the points is a fit to Equation 5.10. (e) Sample 7/G1. (f) Sample 60/3G4. For 6/G2 and 60/3G4 $H_{c2\perp}$ is determined from the scaling laws while the points shown for $H_{c2||}$ are determined directly from the resistive transition. For 7/G1 both $H_{c2\perp}$ and $H_{c2||}$ are determined from the scaling laws.

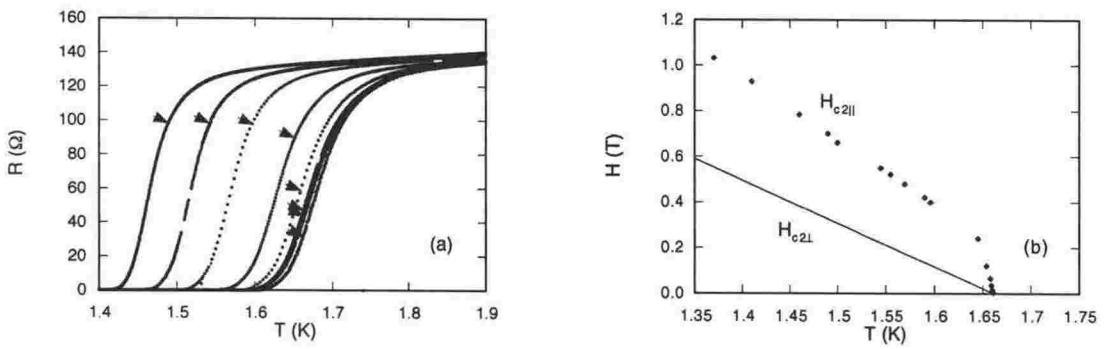

Figure 6.4: (a) The resistive transitions in a parallel applied field for sample 60/3G1. From right to left the curves correspond to fields of 0.0036, 0.015, 0.035, 0.065, 0.12, 0.24, 0.4, 0.55 and 0.7 T. The arrow marks the position of $H_{c2||}$ determined from the transition, and confirmed by the scaling of the fluctuation conductivity at higher fields. (b) The upper critical fields of sample 60/3G1. There is a crossover from linear 3D behavior at low temperatures to 2D square root behaviour at high temperatures, caused by the coherence length becoming larger than the total sample thickness.

tion of the critical field has less theoretical motivation than the scaling approach the narrowness of the parallel transitions ensures a reasonable degree of accuracy. The parallel critical field of sample 60/3G4 derived in this way is shown in Figure 6.3(f), along with $H_{c2\perp}$ derived from the scaling laws. The uncertainties in $H_{c2||}$ are taken from the width of the transition. It can be seen that $H_{c2||}$ is approximately linear near T_c with slope $S_{||} = 3.1 \pm 0.1$, but there is a deviation below the linear curve at lower temperatures. Once again this is in agreement with the predictions of the Werthamer, Helfand and Hohenberg theory which states that the upper critical field is only linear near T_c. The measured value of $H_{c2||}(0)$ lies below the extrapolated linear intercept by a factor of 0.76±0.2, which is close to the predicted value of 0.69, as noted in Section 5.1.3. For a similar reason the linear $H_{c2\perp}$ derived from the scaling laws has only been shown for temperatures above 0.5 K; at lower temperatures the scaling deteriorates due to the downturn in $H_{c2\perp}$. Thus the poor performance of this sample under the scaling laws is probably related both to a rather large degree of disorder and, at low temperatures, to the failure of the GL linear approximation to the critical fields.

Sample 60/3G1 was analysed closely at temperatures above 1.3 K in order to complement the low temperature data of the similar sample 60/3G4. Figure 6.4(a) shows the parallel field resistive transitions as a function of temperature for sample 60/3G1. As stated above there were signs of a parallel field scaling collapse for this sample, especially at higher fields. At the higher fields the value of $H_{c2||}$ determined from the scaling always corresponds to a point near

the sudden downturn in the resistance at the top of the transition curve, which is in agreement with the results displayed previously for sample 7/G1 (see Figures 6.2(b) and 6.3(b)). To extract the low field $H_{c2||}$ from the curves which did not scale well the position of the critical field on the transition was assumed to follow a similar trend to the critical field of the other samples i.e. as the temperature approaches T_c $H_{c2||}$ corresponds to a lower and lower resistance. Note that the $H = 0$ value is equal to T_c. The arrows on the curves in Figure 6.4(a) indicate the position of $H_{c2||}$ extracted in this way. The resulting phase diagram is shown in Figure 6.4(b) where the parallel field data points are from both field and temperature sweeps. $H_{c2||}$ is clearly linear at lower temperatures with $S_{||} = 2.8 \pm 0.1$, but shows a marked change near T_c to a behaviour resembling a square root dependence on temperature. Although the method used to determine $H_{c2||}$ is somewhat uncertain other definitions, for example using a constant resistance of $100\,\Omega$, also yielded a similar crossover in behaviour.

Such a change in the temperature dependence of $H_{c2||}$ can be interpreted as a dimensional crossover from linear 3D anisotropic GL behaviour at low temperatures to 2D square root behaviour as predicted by Equation 5.10. The crossover occurs as T_c is approached when $\xi_c(T)$ exceeds the total thickness of the sample. The temperature where this should occur can be estimated by setting $\xi_c(T) = \xi_c(0)(1 - T/T_c)^{-1/2}$ equal to the total sample thickness and using $\xi_c(0) = \xi_{ab}(0)/\gamma$ where $\gamma = S_{||}/S_{\perp} = 1.5 \pm 0.1$. This gives the expected crossover temperature as $1.656 \pm 0.002\,\mathrm{K}$, which corresponds fairly closely to the observed crossover point. Furthermore the points above the crossover have been fitted to the thin film expression for $H_{c2||}$ (Equation 5.10), where the only fitting parameter is the coefficient of the temperature dependence of the critical field (which is equal to $H_{c2||}(0)$). The fitting gives $H_{c2||}(0) = 2.1 \pm 0.3$, in reasonable agreement with the theoretical value of $\sqrt{12}\Phi_0/[2\pi d_t \xi_{ab}(0)] = 1.0 \pm 0.1$ where $d_t = 1200 \pm 100$Å is the total film thickness. These results strongly support the interpretation of the change in the critical field behaviour as being a dimensional crossover.

When the scaling laws were applied to the parallel field data of samples 33/1G4 and 36/2G1 only 36/2G1 showed signs of a scaling collapse with $S_{||} = 19 \pm 1$, although, as for samples 60/3G1 and 60/3G4, there was considerable spread. Determination of $H_{c2||}$ using the method described for sample 60/3G4 above also yielded a linear curve with slope 19 ± 1. Since there was no perpendicular field data available for this sample $S_{\perp}$ can not be determined, but by assuming it lies within the range of the other samples the anisotropy can be determined as $\gamma = 10 \pm 2$. Surprisingly, the parallel critical field of sample 30/3G1 determined in the same fashion also showed linear behaviour with $S_{||} = 14 \pm 1$,

implying an anisotropy of 7.4 ± 0.9. This could indicate that sample 30/3G1 has finite interlayer coupling despite the relatively thick Ge layers, although this seems unlikely. No parallel field transition data were available for the single layer sample 2/G6 which would be expected to show isotropic Ginzburg–Landau behaviour at low temperatures and may also have shown a dimensional crossover near T_c.

It was not possible to achieve good parallel field scaling behaviour for any of the other samples with relatively thick Ge layers. There was, however, considerably less broadening of the resistive transitions in this orientation as demonstrated by the data for sample 6/G2 shown in Figure 6.3(a). Therefore, as was the case for sample 60/3G4, $H_{c2\|}$ can be determined from the steepest point on the transition without introducing too much uncertainty. Figure 6.3(c) shows a plot of both $H_{c2\perp}$ and $H_{c2\|}$ for sample 6/G2 where $H_{c2\|}$ has been determined from the steepest point of the transitions in both field and temperature sweeps. The uncertainties determined from the width of the transition are too small to be visible. The solid line through $H_{c2\|}$ is a fit to Equation 5.10, where once again the only fitting parameter is the coefficient of the temperature dependence of the critical field which is equal to $H_{c2\|}(0)$. The fitted value 6.9 is in excellent agreement with the predicted value $\sqrt{12}\Phi_0/[2\pi d_s \xi_{ab}(0)] = 7 \pm 1$ based on the values previously determined for $\xi_{ab}(0)$ and d_s, indicating that the alloy layers in this sample behave as individual 2D superconductors.

The parallel critical fields of samples 5/G1 and 29/2G4 were determined in a similar fashion to sample 6/G2, and both of these showed the same square root dependence on temperature characteristic of 2D behaviour. Similarly sample 33/1G4, which did not obey the scaling laws despite the relatively thin Ge layers, was found to show a square root temperature dependence of $H_{c2\|}$. The fitted values for $H_{c2\|}(0)$ for samples 5/G1 and 29/2G4 were equal to 17.5 and 16.5 respectively, and for sample 33/1G4 $H_{c2\|}(0) = 17.0$. For sample 5/G1 the theoretical value based on Equation 5.10 is 23 ± 5 which is reasonably close to the fitted result, but for samples 29/2G4 and 33/1G4 the theoretical values[4] are 50 ± 5 and 35 ± 6, which are considerably higher than the fitted results. It was also noted that while the transitions as a function of field for sample 29/2G4 were sharp at low temperatures there was considerable broadening at temperatures close to T_c, a feature which may be related to the discrepancy between the fitted and expected values of $H_{c2\|}(0)$.

The results of the investigation of the parallel critical fields are displayed in

[4]To compare the value of $H_{c2\|}(0)$ for sample 33/1G4 with theory it was assumed that ξ_{ab} was within the range of the other samples.

Table 6.3. The dimensionality refers to the observed behaviour of $H_{c2\|}$, not the results of the fluctuation conductivity scaling. The measured and theoretical values of $H_{c2\|}(0)$ are shown only for the samples which displayed two-dimensional behaviour. From the results it can be concluded that three-dimensional behaviour is enhanced by thinner Ge layers. Comparison between samples 36/2G1 and 33/1G4, which have comparable Ge layer thicknesses, shows that the effective interlayer coupling is also enhanced by increasing the thickness of the superconducting layers. The overall picture is as follows: increasing the insulating layer thickness increases the anisotropy and thus raises $H_{c2\|}$ until the 2D limit is reached. In the 2D limit increasing the superconducting layer thickness causes a decrease in $H_{c2\|}$, as predicted by Equation 5.10. Similarly, in coupled multilayers increasing the superconducting layer thickness causes a decrease in $H_{c2\|}$ due to the decrease in the anisotropy.

Sample	$\gamma = \frac{s_\parallel}{s_\perp}$	$H_{c2\parallel}(0)$ (Tesla) (Fitted)	$H_{c2\parallel}(0)$ (Tesla) (Theory)	Dim.
29/2G4	-	16.5	50±5	2D
30/3G4	7.4±0.9	-	-	3D
32/2G1	-	-	-	-
33/1G4	-	17	35±6	2D
36/2G1	10±2	-	-	3D
60/3G1	1.5±0.1	-	-	3D
60/3G4	1.7±0.1	-	-	3D
2/G6	-	-	-	-
5/G1	-	17.5	23±5	2D
5/G2	-	-	-	-
6/G2	-	6.9	7±1	2D
7/G1	5.8±0.8	-	-	3D

Table 6.3: Parameters derived from the analysis of the parallel critical fields. The column marked Dim. is the dimensionality determined from the temperature dependence of the parallel upper critical field.

6.2 Zero Field BKT Transitions

It has already been noted that in some of the samples the zero resistance point lies well below the value of T_c determined from the fluctuation conductivity, especially in those with thinner superconducting layers. This is in agreement with the predictions of the Berezinskii-Kosterlitz-Thouless (BKT) theory discussed in Section 5.2.2 in which thermally created free vortices exist in 2D superconductors at temperatures close to T_c. The appropriate definition of two-dimensionality to be used here depends both on the Josephson coupling between the layers and the superconducting layer thickness. The presence of strong Josephson coupling modifies the logarithmic interaction between the vortices and inhibits the vortex unbinding, leading instead to a 3D phase with no free vortices [6]. The effect of increasing the layer thickness is illustrated by Equation 5.17 which shows that T_{BKT} increases with d_s until it approaches T_c, reflecting the greater interaction between vortex pairs in a thicker film. It can thus be concluded that the most likely samples to show a clear BKT signature well below T_c are those with the thinnest, most decoupled superconducting layers.

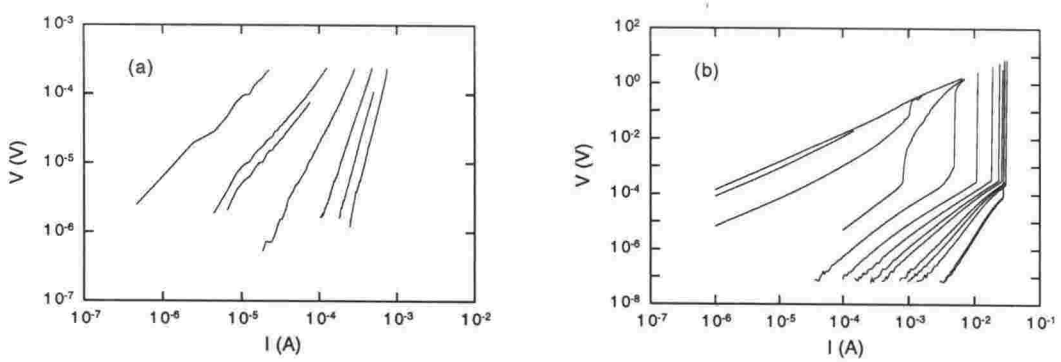

Figure 6.5: IV curves measured in zero applied magnetic field. (a) Sample 30/3G4. From right to left the curves correspond to temperatures of 0.57, 0.64, 0.72, 0.83, 0.9, 0.92 and 1.0K. (b) Sample 5/G1. From right to left the curves correspond to temperatures of 1.217, 1.222, 1.324, 1.4, 1.475, 1.625, 1.7, 1.8, 1.9, 2.0, 2.1, 2.182, 2.255 and 2.297K.

Figures 6.5(a) and 6.5(b) show sets of IV curves taken from samples 30/3G4 and 5/G1 at zero applied field, where each curve corresponds to a different temperature. For sample 30/3G4 the curves are clearly linear on the log–log plot indicating power law behaviour as predicted by the BKT theory. For sample 5/G1 the curves are also approximately linear until at high currents an instability sets in causing the sample to switch to the normal state resistance[5]. A similar instability also exists in 30/3G4, however this sample was studied in a dilution

[5]This instability is discussed in detail in Section 6.4.

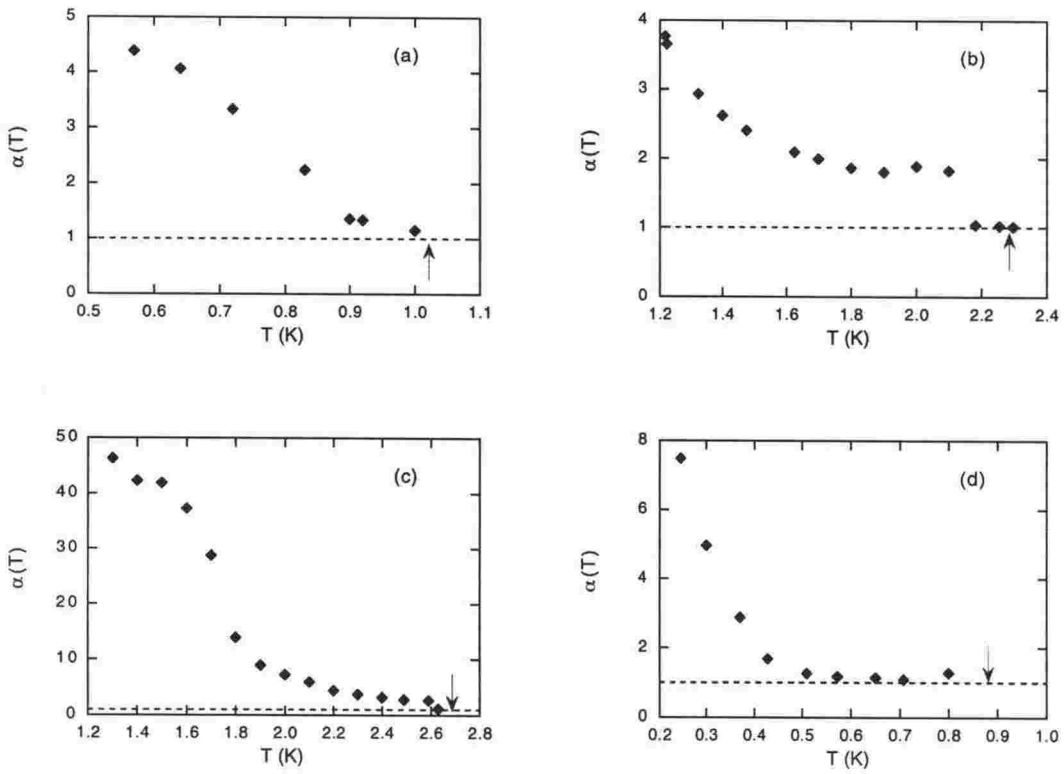

Figure 6.6: The exponent α of the power law fitted to the zero field IV data. (a) Sample 30/3G4. (b) Sample 5/G1. (c) Sample 6/G2. (d) Sample 29/2G4. The arrows mark the position of T_c and the dotted lines show $\alpha = 1$.

refrigerator where it was harder to maintain good temperature stability at high currents, so the instability is not shown in this case. For each sample where data was available a power law has been fitted to the region of the curves below the instability, with the resulting exponent α plotted as a function of temperature in Figures 6.6(a) - (d) for several samples with thick Ge layers. The position of T_c is marked by an arrow. In all cases α is initially 1 close to T_c, indicating linear resistivity, but then shows a steady increase at lower temperatures.

Such behaviour points to the presence of a BKT transition in these samples, with the position at which $\alpha = 3$ corresponding to the vortex pair unbinding temperature T_{BKT}. It is interesting to note, however, that rather than showing a sudden jump from 1 to 3 as expected, the variation in α is rather smooth when it passes through 3. Furthermore samples 5/G1 and 6/G2 do in fact show a jump in α below T_c, however the jump is from 1 to a value around 2 or 2.6 respectively rather than to $\alpha = 3$. Nevertheless it will be argued below that the jump in α does indeed correspond to the BKT transition in these samples, and that the absence of a jump in the other samples can be understood upon considering the

vortex pair unbinding in more detail.

As discussed in Section 5.2.2 the linear resistivity which results from the presence of free vortices above T_{BKT} occurs only at low currents, whereas at high currents the current induced vortex unbinding process dominates and the IV curves obey a power law with $1 < \alpha < 3$. As the temperature is decreased towards T_{BKT} and the density of free vortices falls the linear region is pushed to lower and lower current densities, with the size of the crossover current from linear to power law behaviour inversely related to the size of the largest vortex-antivortex pairs remaining bound. This indicates that in the samples which show a smooth rise in α around the BKT transition the measurements are being performed in the high current region so that there is no sharp jump near $\alpha = 3$, although the point where $\alpha = 3$ can still be associated with T_{BKT}. Only at higher temperatures where the density of free vortices is large does the linear region of the IV curves extend to high enough currents to be observed.

The above conclusion that the measurement currents are too high to easily observe the linear region of the IV curves in several of the samples does not explain why the exponent does not jump directly to 3 in samples 6/G2 and 5/G1. Careful inspection of Figure 6.5(b) shows that at temperatures close to T_{BKT} the IV curves do not obey a perfect power law but instead tend to flatten off at high currents. This could be due to the fact that the current is becoming large enough to unbind all of the vortex pairs so that the resistivity saturates, thereby causing the fitted value of α to be somewhat below the expected value of 3 or more. In contrast to this the the flattening of the IV curves is not so apparent at the lowest temperatures where instead there is a slight hint of upward curvature at low currents. Such upward curvature is most likely caused by a very small remnant field (e.g. the Earth's magnetic field) which creates a small density of free vortices even below T_{BKT}. Figure 6.6(c) also shows that the low temperature values of α for sample 6/G2 are considerably higher than for the other samples, until at the very lowest tempertures the rise in α levels off somewhat. It is possible that at these low temperatures the observed IV characteristics do not represent true BKT behaviour in this sample, and may instead be affected by pinning.

In order to compare the measured values of T_{BKT} with the theoretical predictions Equation 5.17 has been rearranged to give

$$T_{BKT}\lambda_{ab}^2(T_{BKT}) = \frac{\Phi_0^2 d_s}{8\pi k_B \mu_0} \tag{6.4}$$

where the substitution $\lambda_\perp = \lambda_{ab}^2/d_s$ has been made. Figure 6.7 shows a plot

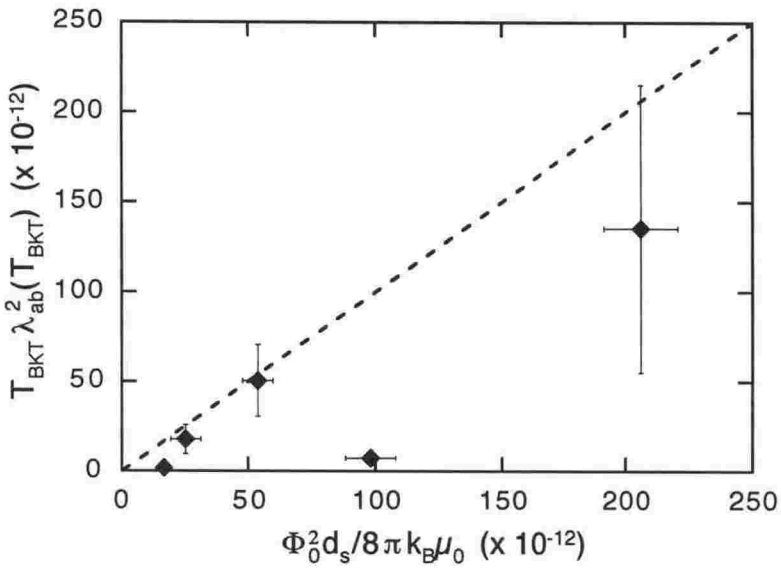

Figure 6.7: A comparison between the values of T_{BKT} determined from the analysis of the IV curves and the theoretical prediction. The straight line represents the expected behaviour based on Equation 5.17.

of $T_{BKT}\lambda_{ab}^2(T_{BKT})$ versus $\Phi_0^2 d_s/8\pi k_B\mu_0$ for several samples with thick Ge layers, where T_{BKT} is determined either from the jump in α or from the condition $\alpha = 3$ when there is no jump. The penetration depth $\lambda_{ab}(T_{BKT})$ is determined from $\lambda_{ab}(0)$ (see Table 6.2) using the GL expression for the temperature dependence, as is appropriate for dirty superconductors close to T_c [2]. For three of the samples (33/1G4, 5/G1 and 6/G2) the agreement between theory and experiment is very good with the points falling within the uncertainties of the line with unit slope[6]. For the other two samples (29/2G4 and 30/3G4) the measured BKT transition temperature is considerably lower than the theory predicts. This may be due to screening of the interaction between large vortex-antivortex pairs by smaller pairs, an effect which can be represented by the inclusion of a vortex dielectric constant in the denominator of Equation 5.17 [29,143]. If this is the case then the measured BKT transition temperatures imply a value of the dielectric constant of around 7 in sample 29/2G4 and around 10 in sample 30/3G4, similar to the values observed in thin films of $YBa_2Cu_3O_{7-\delta}$ [143]. The screening is likely to be most noticeable in the thinnest superconducting layers [143] which may explain why sample 29/2G4 has a high dielectric value, although it is harder to explain why the screening should be so high in sample 30/3G4 when it is not noticeable

[6]The uncertainties are associated mostly with determining the temperature dependence of λ_{ab}, especially in the samples where T_{BKT} is very close to T_c.

in the other samples. An alternative explanation is that the roughness of the boundaries between the superconducting and normal layers (≈ 8 Å [17]) lessens the effective layer thickness i.e. the supercurrents may essentially be confined to the centre of the layer rather than flowing uniformly throughout the thickness. Such an effect could considerably reduce the BKT transition temperature in the very thin sample 29/2G4, however it would be unlikely to be significant in sample 30/3G4.

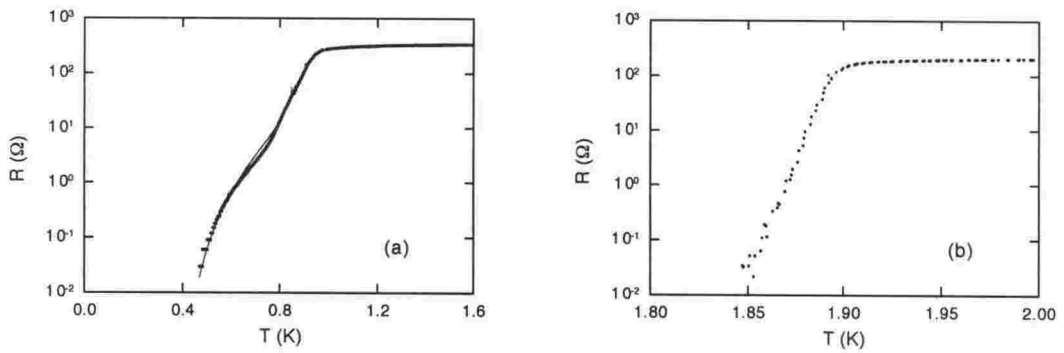

Figure 6.8: The low resistance portion of the zero field resistive transitions of (a) a decoupled sample (29/2G4) and (b) a strongly coupled sample (7/G1).

All of the samples considered above have thick Ge layers so that the individual superconducting layers can be considered two-dimensional with respect to the BKT transition. These samples can be compared with the samples with greater interlayer coupling by considering the resistive transitions in zero field. Figures 6.8(a) and 6.8(b) show plots of the resistive transitions on a logarithmic scale for samples 29/2G4 and 7/G1 respectively. For 29/2G4 the resistance decreases rapidly around T_c and then undergoes a more gradual decline at lower temperatures, whereas for 7/G1 the rapid decrease continues to the lowest measureable values. As T approaches T_{BKT} in the BKT theory the density of free vortices decreases, and in the limit of small currents the resistance is expected to go to zero according to

$$R(T) \simeq R_n \exp\left[-2\left(b\frac{T_c - T}{T - T_{BKT}}\right)^{1/2}\right] \tag{6.5}$$

where b is a material dependent parameter [6]. The solid line in Figure 6.8(a) shows a fit to this equation using the value $T_{BKT} = 0.35$ K determined from the IV curve analysis. The fit is almost indistinguishable from the measured data despite the fact that the only free parameter is b for which the fitted value of 5.1 is within the typical range of values measured on other systems [6]. Fits of

Equation 6.5 to the transitions of the other samples described above generally produce similar results, with values of b in the range 7–13. The most noteworthy exception is sample 30/3G4 in which the measured resistance is greater than the fitted value for temperatures below about 0.9 K. As noted above even the low measurement current used (1 μA) is enough to induce some vortex pair unbinding in this sample, and it is these current induced free vortices which cause the breakdown of the fit at low temperatures. This conclusion is further corroborated by the fact that the point at which the deviation from the fitted curve occurs corresponds closely to the point at which the IV exponent starts to increase smoothly above 1.

Fitting of Equation 6.5 to the data for sample 7/G1 yields less convincing results, mainly because 7/G1 does not demonstrate the change in slope on the logarithmic plot that the more two-dimensional samples show. Note also that the temperature range over which the resistance decreases below the measureable level is much smaller for sample 7/G1 than it is for 29/2G4. This is to be expected due to the strength of the interlayer coupling in 7/G1 which means that the sample undergoes a 3D transition well before the BKT transition can be observed [6]. The samples 2/G6 and 60/3G1 also display rapidly decreasing resistance below T_c with no clear sign of a BKT transition. The analysis of the fluctuation conductivity in Section 6.1 showed that sample 60/3G1 is only two-dimensional very close to T_c where the coherence length becomes greater than the total thickness, so it is not surprising that this sample does not show an observable BKT transition. The fluctuation conductivity for sample 2/G6 on the other hand was well described by a 2D model, however the single layer in 2/G6 is considerably thicker than the superconducting layers in all of the samples described above which show clear BKT signatures, so the expected BKT transition temperature is very close to T_c in this sample. The IV curves for 2/G6 do indeed change from linear to non-linear very close to T_c, but the voltage exhibits a much stronger dependence on the current than a power law. This may relate to the effects of pinning forces in this sample.

From this analysis it can be concluded that the samples with highly decoupled superconducting layers can be described by the zero field BKT theory. No evidence of the effect of pinning forces was observed due to the fact that the BKT transition generally occurs close to T_c where thermal disorder tends to average the pinning to zero. For two of the samples the observed BKT transition temperatures were considerably lower than the theoretical prediction. For the thin layered sample 29/2G4 this may relate to screening of the vortex-antivortex interaction or to interface effects at the layer boundary. The samples with stronger

interlayer coupling, as indicated by the fluctuation conductivity results, do not show signs of a BKT transition due to the fact that they are not two-dimensional with respect to vortex fluctuations. The single layer alloy film also does not show an observable zero field BKT transition due to its large thickness.

6.3 Vortex States and Dynamics

6.3.1 Perpendicular Fields

In Chapter 5 it was shown that the resistivity of type-II superconductors is governed by the motion of magnetic vortices, the dynamics of which depend sensitively on the vortex state. In order to understand the transport properties of the Ta_xGe_{1-x}/Ge multilayers it is therefore important to determine their magnetic phase diagrams as a function of field, temperature and current. Section 6.1 has already achieved this for the fluctuation region of the phase diagram where the resistance is close to the normal state value. In the present section the analysis is extended to examine the way in which the resistivity goes to zero, starting first with the simplest sample, the unlayered alloy 2/G6.

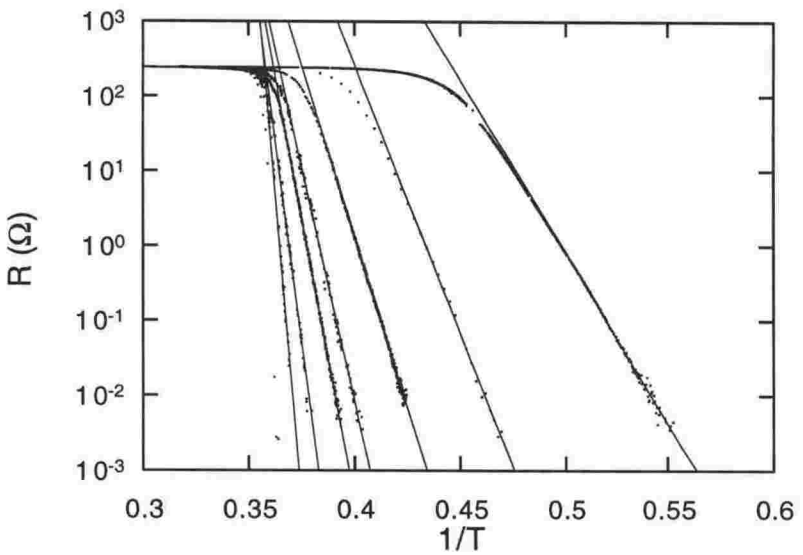

Figure 6.9: Perpendicular field Arrhenius plot for sample 2/G6. From left to right the curves correspond to fields of 0.0046, 0.01, 0.03, 0.07, 0.1, 0.2, 0.4 and 0.8 T. The solid lines represent fits to the low temperature thermally activated region, with the slope equal to the activation energy $U(H)$.

Figure 6.9 shows an Arrhenius plot of the resistance of sample 2/G6 where the different curves correspond to different perpendicular fields, each measured using a low applied current of $1\,\mu$A. A linear portion is clearly evident at low temperatures indicating a thermally activated resistance $R \propto \exp(-U/k_BT)$. If the activation energy is assumed to be of the form $U(H,T) = U(H)(1 - T/T_c)$ then the slope of the linear region on the log plot gives a measure of the activation energy $U(H)$ (see Appendix A). The measured slopes are shown as a function of

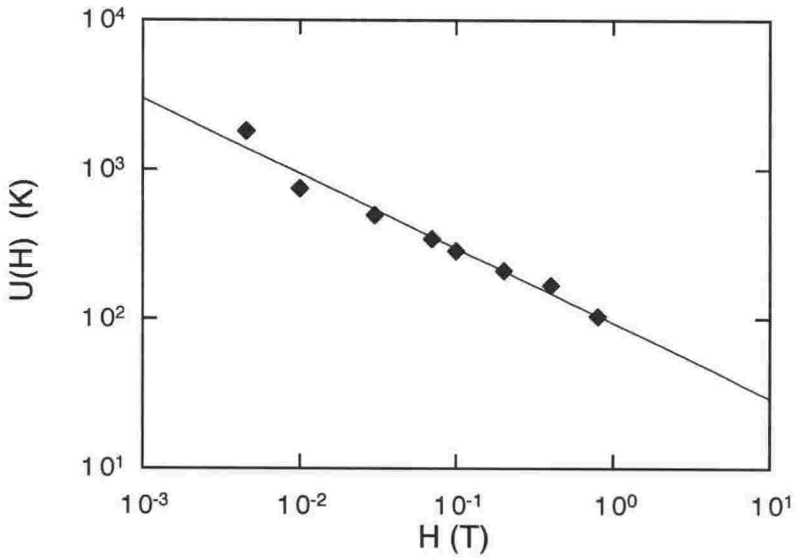

Figure 6.10: The activation energy (in Kelvins) for sample 2/G6 as measured from the Arrhenius plot of Figure 6.9. The straight line is a power law fit which shows that $U \propto 1/H^{1/2}$.

field in Figure 6.10 where the solid line is a fit to a power law of the form $U(H) = U_0 H^{-\beta}$. The resulting exponent β is equal to 0.5, so the activation barrier can be rewritten as $U(H) \simeq U_0 a_0/\sqrt{\Phi_0}$ where a_0 is the intervortex spacing given by Equation 5.3. This form of activation energy is predicted by Equation 5.62 and is characteristic of plastic vortex motion where the main barrier relates to the energy required for the vortices to hop over a distance a_0. However the fitted value of the prefactor U_0 is 93, whereas Equation 5.62 predicts a value $U_0 = 1400 \pm 400\,\mathrm{K}$ based on the value of λ_{ab} at $T = 0$ (see Appendix A). The disagreement indicates that a slightly different process to that described in Section 5.3.6 may determine the barriers against flux flow, but nevertheless it appears that the activation energy in this sample scales with the intervortex spacing indicating some form of plastic flux motion via large vortex hops.

Figure 6.11 shows an Arrhenius plot of the low current resistance of sample 6/G2 in various perpendicular fields, where once again thermally activated behaviour is evident at low temperatures. The corresponding activation energies are shown as a function of field in Figure 6.12(a) including a best fit line of the form $U(H) = 30 \times \ln(6.3/H)$ with H in Tesla. A logarithmic form for the activation energy is predicted by Equation 5.58 for the thermal creation of unbound, mobile dislocations of approximate size a_0^2/ξ_{ab}. For this sample the predicted value of the prefactor is $14 \pm 4\,\mathrm{K}$ which is in reasonably good agreement with

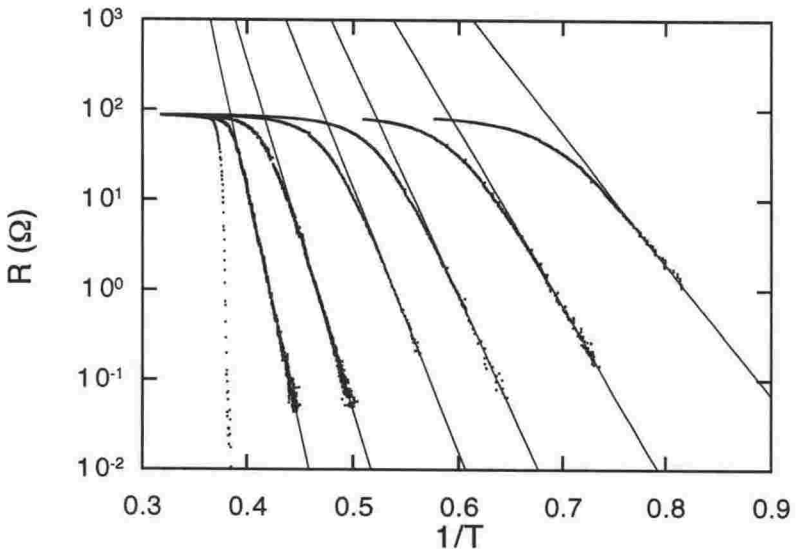

Figure 6.11: Perpendicular field Arrhenius plot for sample 6/G2. From left to right the curves correspond to fields of 0, 0.1, 0.3, 0.7, 1.0, 1.4 and 1.8 T. The solid lines represent fits to the low temperature thermally activated region.

the measured value of 30 K, especially considering the approximations associated with the theory. The same analysis has been performed for sample 30/3G4 yielding a similar activation energy as shown in Figure 6.12(b) where the best fit line is given by $U(H) = 5.2 \times \ln(1.7/H)$. For this sample the expected prefactor is 3 ± 1 K, once again reasonably close to the measured value and indicating also that the activation energy increases with the superconducting layer thickness d_s as predicted by the theory. The characteristic field at which the activation barrier vanishes is also larger in sample 6/G2 ($H_0 = 6.3$ T) than in sample 30/3G4 ($H_0 = 1.7$ T) which is a reflection of the smaller critical fields in 30/3G4 (due to the lower T_c). The similarity between the structures of samples 6/G2 and 30/3G4 provides evidence that this kind of activation energy is characteristic of multilayers where both the superconducting and insulating layers are relatively thick.

Further information can be gained about the vortex phases in these samples by studying their IV characteristics. Figures 6.13(a) and (b) show log–log plots of sets of IV curves for sample 2/G6 measured in perpendicular fields of 0.2 and 0.8 T respectively, where each curve corresponds to a different temperature. The persistence of superconductivity is limited at high currents by the existence of a Larkin–Ovchinnikov instability which will be discussed in Section 6.4. Below the instability the shape of the IV curves is strongly influenced by the temperature,

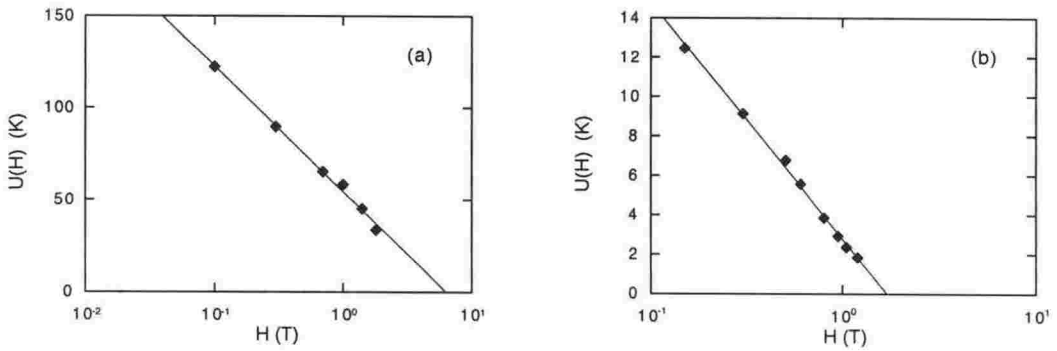

Figure 6.12: The activation energy (measured in Kelvins) for (a) sample 6/G2 as measured from the Arrhenius plot of Figure 6.11 and (b) sample 30/3G4. The solid lines are fits to Equation 5.58.

with the curves at high temperatures displaying linear behaviour at low currents followed by a non-linear rise at higher currents, whereas at low temperatures there is no sign of the linear region. Instead the voltage rises very rapidly as the current is increased until it begins to level off somewhat at high currents. Interestingly the low temperature curves are considerably less steep at 0.8 T than they are at 0.2 T, and the degree of rounding off at high currents is also less in the higher field. IV curves of this type are predicted within the vortex glass model where the upward curvature at low currents corresponds to plastic flux motion with finite activation energies in the flux liquid, as is observed in the Arrhenius plot for this sample. The downward sloping curves at low temperatures correspond to the diverging activation barriers in the vortex glass phase.

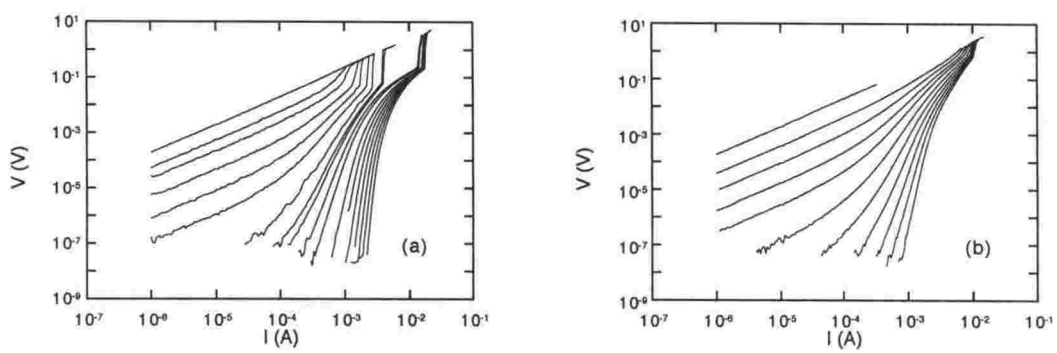

Figure 6.13: IV curves for sample 2/G6 in a perpendicular applied field of (a) 0.2 T. From right to left the curves correspond to temperatures of 1.36, 1.46, 1.56, 1.66, 1.76, 1.86, 1.96, 2.1, 2.167, 2.234, 2.267, 2.335, 2.43, 2.5, 2.54, 2.59, 2.63 and 2.72 K. Note the sharp downward curvature at low temperatures. (b) 0.8 T. From right to left the curves correspond to temperatures of 1.36, 1.46, 1.56, 1.66, 1.76, 1.86, 1.96, 2.03, 2.1, 2.167 and 2.335 K. The downward curvature at low temperatures is much less severe than it is at 0.2 T.

An attempt has been made to scale the IV curves according to the prescription of the vortex glass model (Equations 5.53) by varying the scaling exponents and the field dependent melting temperature. The scaling fit from the 0.2 T data set is shown in Figure 6.14(a) where the optimised values $\nu = 1.08$, $z = 9.0$ and $T_g = 2.20\,\mathrm{K}$ have been used. Similar scaling was observed at six other fields between 0.01 T and 0.8 T with essentially the same fitted values of $\nu = 1.08 \pm 0.04$ and $z = 9 \pm 1$. A collapse of the data onto two curves is clearly evident at low currents, however below T_g the curves deviate from the universal function at high currents. Such a breakdown in the scaling is expected when the Lorentz force on the vortices becomes large enough that the motion is no longer thermally activated, in which case a description in terms of flux flow is more appropriate. The IV curves closest to the melting temperature always follow a power law down to the lowest currents with a field independent exponent of around 6. This value is in fairly good agreement with the vortex glass theory which predicts an exponent equal to $(z+1)/(D-1) = 5.0 \pm 0.5$ assuming the dimensionality $D = 3$.

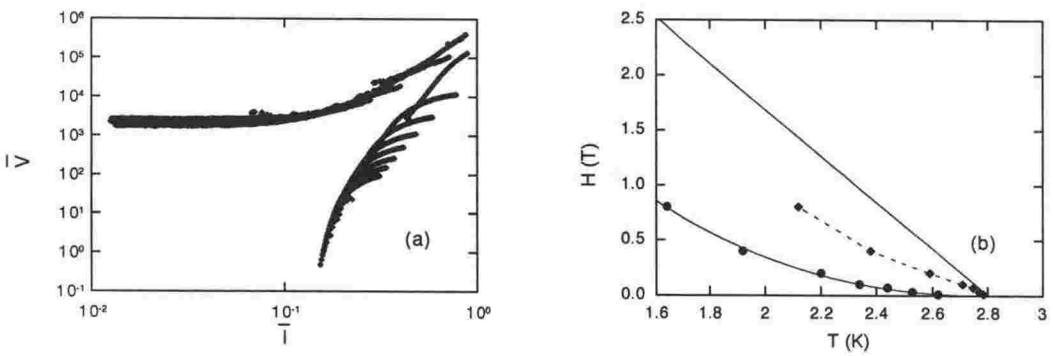

Figure 6.14: (a) IV curves for sample 2/G6 at 0.2 T transformed according to the vortex glass scaling laws. The parameters are $z = 9$, $\nu = 1.08$ and $T_g = 2.20\,\mathrm{K}$. (b) Perpendicular field phase diagram for sample 2/G6. The circles represent the vortex glass melting transition while the diamonds represent the boundary between the pinned liquid and the non-viscous liquid. The upper solid line is H_{c2}, the lower solid line through the circles represents a power law fit to the melting line and the dashed line through the diamonds is a guide to the eye.

The observation of vortex glass scaling in sample 2/G6 implies that the sample is three-dimensional with respect to the vortex properties despite its relatively small thickness. At least four length scales are important for determining the dimensionality within the vortex glass model: (i) the sample thickness d_s, (ii) the intervortex spacing a_0, (iii) the collective pinning length L_c and (iv) the vortex glass coherence length ξ_{vg}. The collective pinning length, which depends on the degree of disorder in the sample (see Equations 5.33), can be rewritten in the single vortex regime as $L_c \simeq \xi(j_0/j_c)^{1/2}$ [6] where j_0 is the depairing critical

current defined in Equation 1.1. Taking $j_c \approx 200 \times 10^6$ A/m^2 based on the point where the IV curves in Figure 6.13(a) begin to flatten[7] off, and substituting the calculated value of j_0 at $T = 0$ yields an upper estimate for L_c of about 500Å. This is less than or of the order of the intervortex spacing a_0 at all of the fields used here, justifying the use of the single vortex expression. Because L_c is also less than the sample thickness the vortices are able to optimise their pinning energy as they traverse the sample, and the pinning is therefore three-dimensional. On the other hand the vortex glass model described in Section 5.3.4 is strictly valid only when the vortex glass coherence length is less than the sample thickness but greater than the intervortex spacing (at least well below T_g) [110], conditions which the above discussion has shown cannot both be satisfied.

The conclusion therefore is that the sample is in the single vortex 3D pinning regime where the elastic creep barriers are expected to become infinite as the current goes to zero (see Equation 5.47), but the divergence of the vortex glass correlation length may be cut off by the finite dimensions of the sample as the temperature approaches the 3D transition temperature T_g. This means that a description in terms of a true glass transition is not strictly valid, but nevertheless it appears that in this sample the thickness is large enough relative to the other parameters that the signature of the vortex glass can be observed i.e. a scaling collapse. Similarly the melting line determined from the scaling analysis is probably best interpreted as a plastic/elastic boundary rather than a true vortex glass transition line. Above the melting line where the glass correlations are relatively small the dissipation is dominated by plastic motion, whereas below the melting line where the glass correlations are relatively large the plastic barriers grow so that only elastic hopping processes on scales less than ξ_{vg} are observable.

An attempt was made to fit the IV curves in the vortex solid phase to an equation of the form $\rho(T) \propto \exp^{-c(j_c/j)^\mu}$ (see Section 5.3.4) using the value $\mu = 1/7$ as appropriate for the single vortex regime, however the large number of parameters required means that the results were strongly dependent on the amount of the curve used for the fit. Furthermore the value of μ is expected to change rather rapidly from 1/7 to 5/2 as the field increases towards the small bundle pinning regime which adds further uncertainty to the fitting process, so overall the fitting of the IV curves did not provide any meaningful information about the vortex state. The parameter z determined from the scaling is somewhat higher than values measured on other systems which are typically in the range 4–7, however it has been noted that in a wide range of samples the slope of the power law

[7]This marks the crossover from thermally activated to flux flow behaviour.

at T_g is not universal but depends on the degree of disorder [144]. It is possible that this slope, which is related to z, also shows a similar dependence on the dimensionality. It should also be noted that the value of z is quite sensitive to the value of T_g e.g. increasing T_g by 0.05 K at 0.07 T combined with a new value for z of around 7.5 causes very little deterioration of the scaling collapse.

For sample 2/G6 the activation energies were measured at low currents where dissipation is only observable in the vortex liquid phase. The measured activation energies of this sample agree in form with the expression for plastic motion given in Equation 5.62, indicating that the vortex liquid is highly viscous in nature as may be expected due to the existence of finite vortex glass correlations. The thermally activated behaviour shown in Figure 6.9 does not continue in the vortex liquid phase right up to $H_{c2}(T)$, but changes to a more gradual increase as the resistance approaches R_n. In this region the thermal energy is high enough that the liquid is no longer viscous so pinning becomes ineffective [125] (see also Section 5.3.2), although similarly to results on $YBa_2Cu_3O_{7-\delta}$ [145] the free flux flow limit given by Equation 5.30 is never quite reached. The change in behaviour occurs at a resistance about one tenth of the normal state value so it can be concluded that the majority of the resistive transition takes place in the relatively unpinned vortex liquid phase, whereas the activated region which extends well below H_{c2} covers only the area close to zero resistance.

These ideas are collected together in a single phase diagram for sample 2/G6 shown in Figure 6.14(b) which includes the melting points determined from the scaling analysis and also the points where the Arrhenius plot shows a deviation from thermally activated behaviour. A simple power law has been fitted to the vortex glass melting points to give a melting line $H_g = 0.56(T_c - T)^{1.7}$ which is of the form predicted within the vortex glass model [44] although the exponent 1.7 is somewhat higher than the predicted value of 1.33. The prediction is expected to hold only close to T_c, whereas the measurements extend well below T_c which may explain the discrepancy.

A set of IV curves taken from sample 6/G2 in a perpendicular field of 0.7 T is shown in Figure 6.15(a). While the data appear similar to the IV curves of sample 2/G6, including rather clear power law behaviour at intermediate currents, a close inspection reveals that all of the IV curves show an upward curvature at low currents. In Figure 6.15(b) several of the low temperature IV curves at 0.7 T are compared to similar IV curves measured in a field of 0.3 T. Both sets show approximate power law behaviour at high currents, but unlike the 0.7 T curves the 0.3 T curves do show clear downward curvature at low currents indicating glass-like behaviour. There are two possible explanations for this observation.

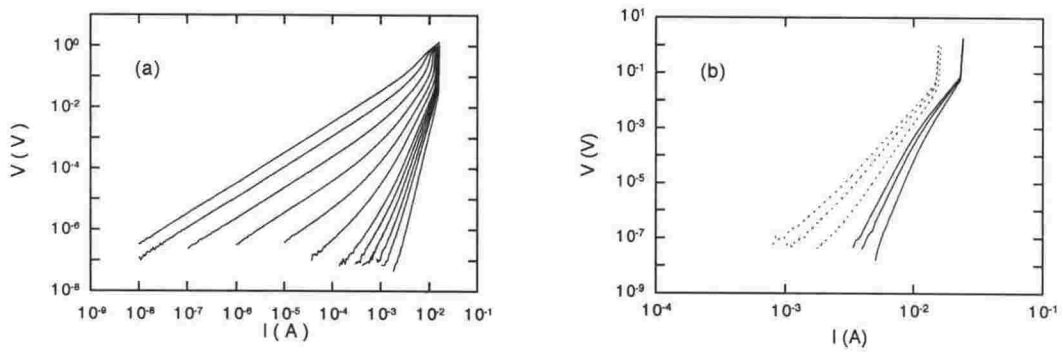

Figure 6.15: (a) IV curves for sample 6/G2 in a perpendicular applied field of 0.7 T. From right to left the curves correspond to temperatures of 1.21, 1.3, 1.35, 1.4, 1.45, 1.5, 1.6, 1.7, 1.8, 1.9, 2.0 and 2.1 K. (b) A comparison between the low temperature IV curves of sample 6/G2 in different perpendicular fields. The solid curves are measured in a field of 0.3 T at temperatures of 1.21, 1.3 and 1.35 K, while the dashed curves are measured at the same temperatures but in a field of 0.7 T. Both sets of curves show power law behaviour at high currents, but the 0.3 T curves bend downwards at low currents whereas the 0.7 T curves bend upwards.

Firstly it may be that at the field of 0.7 T the available temperature range meant that all of the measured curves were above the melting temperature. An attempt was made to scale the curves using a melting temperature below 1.21 K, however it was not possible to collapse them all onto the upper universal function unless a very high value (≈ 13) was used for z, and even then the scaling was rather poor. This is a reflection of the fact that even the IV curves with very large slopes show upward curvature at low currents. An alternative explanation is that the individual layers in this sample are two-dimensional at high fields so that the divergence of the vortex glass coherence length is cut off well before the melting line. This is similar to the proposed situation in sample 2/G6, but there the sample was sufficiently thick that the glass correlations became large enough to ensure plastic flux motion was unobservable below T_g. Figure 6.16(a) shows an attempt to scale the 0.7 T IV curves using the 3D vortex glass model with $T_g = 1.48$ K, $z = 6.9$ and $\nu = 1.1$. The high current portions of the curves do indeed collapse rather nicely onto two functions but at low currents the linear region of the IV curves below T_g deviates from the lower scaling function. Very similar behaviour has been observed in a 100Å thick film of $YBa_2Cu_3O_{7-\delta}$ [123] in which the deviation below T_g was due to plastic flux motion on scales greater than the vortex glass coherence length cutting off the diverging elastic activation energy (in even thinner films a 2D vortex glass was observed). At higher currents the length scale of the activated hopping process becomes less than ξ_{vg} (see Figure 5.13), so plastic motion is inhibited and the sample displays three-dimensional power law IV curves. The inset to the scaling plot shows the current I_x at which non-

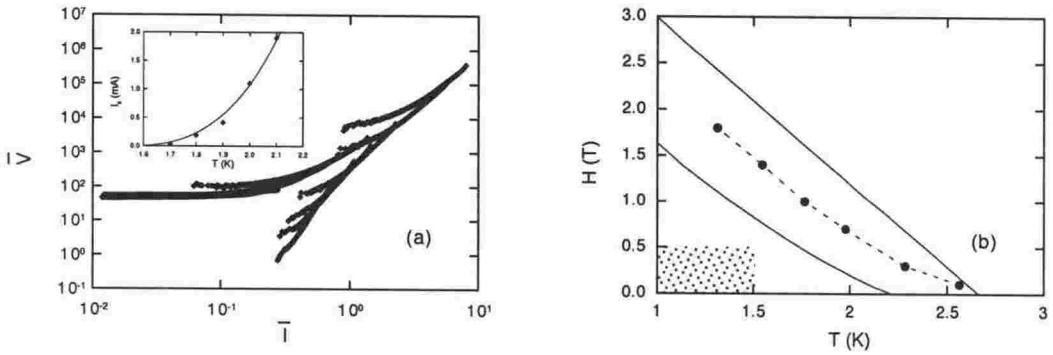

Figure 6.16: (a) IV curves for sample 6/G2 at 0.7 T transformed according to the vortex glass scaling laws. The parameters are $z = 6.9$, $\nu = 1.1$ and $T_g = 1.48$ K. The inset shows a plot of the current above which the 0.7 T IV curves become non-linear. The solid line is a fit to the predictions of the vortex glass theory. (b) Perpendicular field phase diagram for sample 6/G2. The upper solid curve is H_{c2} and the circles mark the boundary between activated and non-activated resistivity. The lower solid curve shows the dislocation mediated melting line predicted by Equation 5.2.4. Finally the shaded area marks a possible 3D vortex glass phase. Sample 30/3G4 has a similar phase diagram.

linearity first becomes apparent in the IV curves. Clearly I_x does not follow a linear temperature dependence as predicted by the simple Anderson–Kim flux creep model. The solid curve shows a fit to an equation of the form $I_x \propto (T - T_g)^{\nu(D-1)}$ as predicted by the vortex glass theory where the fitted parameters $T_g = 1.6$ and $\nu = 1.5$ are in reasonable agreement with the results of the scaling analysis. This provides further confirmation that the observed vortex dynamics relate to the growth of vortex glass coherence.

The fact that sample 6/G2 shows downward sloping IV curves at 0.3 T implies that it is at least quasi-three-dimensional at low fields, however it seems even more unlikely that the individual layers of this sample are thick enough to be three-dimensional on their own. Alternatively there may be a finite degree of coupling between the superconducting layers at low fields, with a dimensional crossover to a decoupled phase occuring somewhere between 0.3 and 0.7 T at low temperature. This is in contrast to the behaviour of the critical field which was well described by a two-dimensional model, and also to the observation of a zero field BKT transition close to T_c, although in both of these cases the relevant measurements were performed at high temperatures or field densities. Furthermore, consideration of the electron tunneling length in amorphous Ge of about 8 Å [20, 24] shows that there is unlikely to be any significant Josephson coupling between the layers at any fields in this sample. Finally, insertion of the field 0.3 T into Equations 5.27 and 5.28 yields values for the anisotropy γ of 7 ± 2 and 11 ± 3 respectively which are surely too low for this strongly decoupled

sample (although these values are similar to the somewhat anomalous value for the anisotropy observed in sample 30/3G4). Any coupling must therefore be magnetic in nature, although it is unclear whether magnetic coupling is able to increase the effective dimensionality of the flux creep and cause a transition into a glassy phase. Interestingly however, a similar crossover from a vortex glass phase at low fields to a two-dimensional phase at high fields has been observed in $Tl_2Ba_2CaCu_2O_8$ [146], where the crossover field was also found to be considerably higher than that predicted by Equations 5.27 or 5.28[8]. Abulafia *et. al* [119] found a rather large region below the melting line on the phase diagram of $YBa_2Cu_3O_{7-\delta}$ over which flux motion was dominated by dislocation motion. Interestingly the exponent μ describing the current dependence of the activation barriers for the dislocation motion was greater than zero implying glass-like dynamics. In light of this it could be speculated that the glass-like behaviour observed in sample 6/G2 may actually relate to the onset of pinning of the mobile dislocations.

Unlike sample 2/G6 both 30/3G4 and 6/G2 exhibit activation energies which vary logarithmically with field implying that the resistance in these samples is governed by the motion of thermally created dislocations of a size $\sim a_0^2/\xi_{ab}$. The relevant dislocations are created individually due to the disorder in the surrounding lattice, rather than in pairs as is required below T_m^{2D} in the absence of disorder. This description implies that the vortices are in a two-dimensional state subject to strong thermal fluctuations, crossing over to a possible 3D vortex glass phase at low temperatures and fields where both the plastic and elastic activation barriers become extremely large. In the measured regime there is no clear signature relating to the motion of dislocations created solely by the quenched disorder (see Equation 5.56 and the associated discussion). In samples such as these a two-dimensional BKT melting transition is also expected to occur at high fields, mediated by the unbinding of thermally created dislocation-antidislocation pairs [26,78,147]. In analogy to the zero field BKT transition it might be expected that the unbinding would lead to a distinct change in the resistivity at T_m^{2D}. The resistivity does indeed show a change from thermally activated behaviour to a slower temperature dependence close to H_{c2} which could be associated with the melting transition. It must be remembered, however, that at T_m^{2D} only the activation energy for unbinding the largest dislocation pairs vanishes, whereas the resistivity in the activated region shows that disorder cuts off the interaction between dislocations so that only pairs of size $\lesssim a_0^2/\xi_{ab}$ are bound at low temper-

[8]It may be that the decoupling transition in highly anisotropic systems is mediated by the unbinding of bound pairs of dislocations, or quartets (see Section 5.2.5), in which case Equations 5.27 and 5.28 are not relevant.

atures. Furthermore at temperatures just above T_m^{2D} the vortex liquid behaves like a solid at short length scales. The crossover to a non-activated resistivity is therefore most likely to signify the point at which the small dislocations unbind causing lattice order to be lost on short length scales, rather than signifying the melting transition itself.

The perpendicular field phase diagram of sample 6/G2 is shown in Figure 6.16(b). The upper solid line represents H_{c2} while the circles show the boundary between the activated and non-activated resistivities. This boundary, which occurs at a resistance around one tenth of the normal state value, is similar to the boundary between the viscous and non-viscous liquids in sample 2/G6 and covers about the same fraction of the phase diagram (note the different scales in Figures 6.14(b) and 6.16(b)). It was argued above that the boundary occurs above T_m^{2D} where the smallest dislocation pairs unbind, however the correlation length which describes the dislocation pair unbinding decreases rapidly above T_m^{2D} [78], so the point where the resistance changes is probably fairly closely associated with the clean limit 2D melting temperature. To test this idea the predicted melting line has been calculated from Equation 5.2.4 using a value of 0.64 for the renormalisation constant[9] A. The predicted melting line, shown as the lower solid curve on the phase diagram, does lie a small distance below the dotted line indicating that the crossover into a non-activated resistivity is indeed caused by the unbinding of small sized dislocation pairs[10]. The shaded region at low fields and temperatures marks approximately the area where the IV curves indicate a 3D vortex glass phase may exist. Just above this region the IV curve analysis also displays some evidence for glass-like behaviour, however the finite sample size limits the growth of the vortex glass correlations. These correlations decrease at higher fields and temperatures so that the dissipation is dominated by small scale dislocations. Note that in sample 2/G6 the activation energy was considerably higher in the vortex liquid phase than the activation energy in sample 6/G2 in the 2D vortex solid, whereas it might be expected that the barriers should be larger in the solid phase. To account for this it must be remembered that in the 3D liquid finite vortex glass correlations exist which limit the modes of plastic flux creep, whereas in two dimensions plastic deformations are allowed even below the melting line. The available measurements indicate that sample 30/3G4 has a similar phase diagram to that of the similarly structured sample 6/G2 shown in Figure 6.16(b).

[9]This is the value found in thin films of Nb_xGe_{1-x} [20], although T_m^{2D} is only weakly dependent on A in any case.

[10]Yazdani *et al.* [26] refer to this as local melting of the disordered 2D vortex lattice.

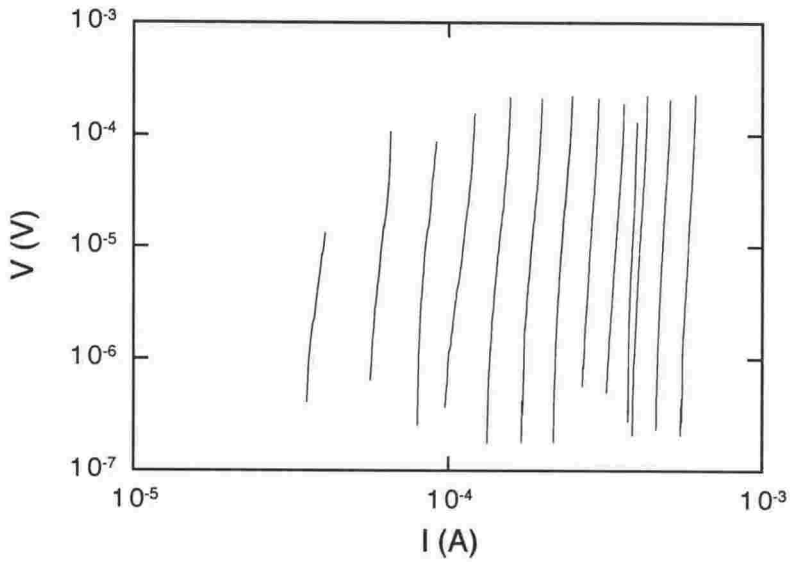

Figure 6.17: Perpendicular field IV curves for sample 30/3G4 measured at 77 mK. From right to left the curves range from 0.1 - 1.3 T in 0.1 T steps. The curves are almost vertical due to the lack of thermal energy at this low temperature.

Measurements have also been made on sample 30/3G4 in the extreme low temperature limit. Figure 6.17 shows a set of perpendicular field IV curves taken from sample 30/3G4 at 77 mK, where the lowest curve corresponds to $H/H_{c2} \approx 0.05$ and the highest to $H/H_{c2} \approx 0.7$. Fits to a power law give exponents between 20 and 70, indicating the extreme steepness of the curves due to the lack of thermal energy to assist the vortex hopping. At low currents vortex motion is not possible in this regime, however as soon as the current is sufficient to overcome the pinning barriers the vortices move freely leading to the observed rapid rise in the resistance. This type of current dependence of the resistivity is similar to the predictions of the vortex glass model in which the resistance also decreases rapidly with current. The main difference is that the vortex glass requires a diverging activation energy to prevent vortex motion at finite temperatures, whereas in this case the resistance increases due to the lack of thermal energy to propel the vortices over pinning barriers of any size[11]. An interesting possibility is that quantum tunneling [6] may influence the vortex dynamics at these low temperatures, although a detailed investigation is beyond the scope of this work.

[11]Note that this does not exclude the possibility of diverging activation barriers at low temperature in this sample. The point is that any barrier height will prevent vortex motion below j_c if there is no thermal energy.

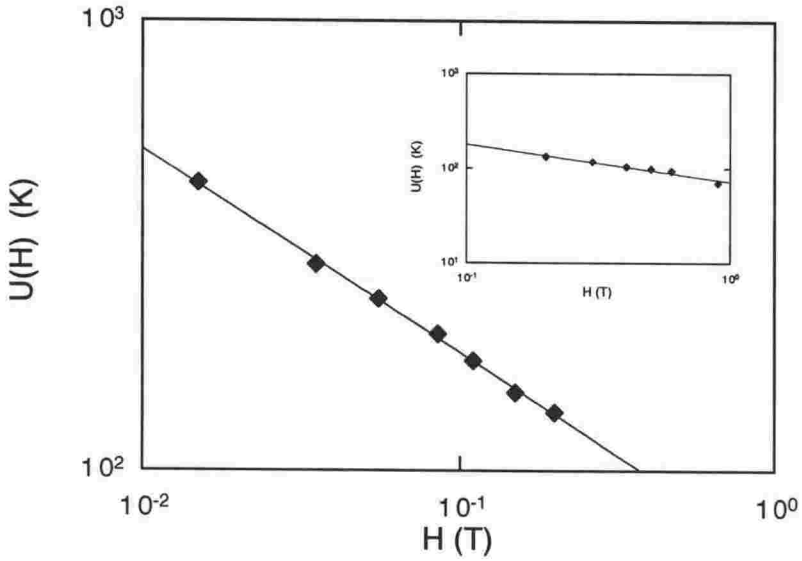

Figure 6.18: The activation energy (in Kelvins) for sample 60/3G1. The power law fit shows that $U \propto a_0$ with a very similar prefactor to sample 2/G6, implying that both behave three-dimensionally. The inset shows the activation energy of sample 7/G1 which also shows a similar sized activation energy but with a slightly weaker field dependence.

Further understanding of the role of dimensionality in determining the vortex properties can be gained from an investigation of more strongly coupled multilayer samples such as 60/3G1, 60/3G4 and 7/G1. Figure 6.18 shows a plot of the perpendicular field activation energies of sample 60/3G1 determined from the Arrhenius plots in the manner described above. The solid line is a power law fit of the form $U(H) = 64 \times H^{-0.45}$. The exponent is close to 1/2 which indicates that like sample 2/G6 the activation energy of this sample can be written in the form $U(H) \approx U_0 a_0/\sqrt{\Phi_0}$. Furthermore if account is taken of the anisotropy ratio of sample 60/3G1 then the values of U_0 for the two samples are almost identical. Several conclusions can be drawn from this similarity. Firstly, although the activation energies are not of the correct size, both the field dependence and the dependence on anisotropy agree with the predictions of Equation 5.62. Secondly, since the activation energy does not depend on the thickness of the sample the vortex dynamics in 2/G6 and 60/3G1 must surely be three-dimensional. This agrees with the observation of vortex-glass behaviour in sample 2/G6, and is also consistent with the description of the activation energies in terms of the 3D viscous liquid model. The inset to Figure 6.18 shows the activation energy of sample 7/G1 which also shows a power law field dependence of the activation energy but with an exponent of 0.4. The fields used for 7/G1 are higher than those used

for samples 2/G6 and 60/3G1, so it may be that the exponent decreases slightly with increasing field.

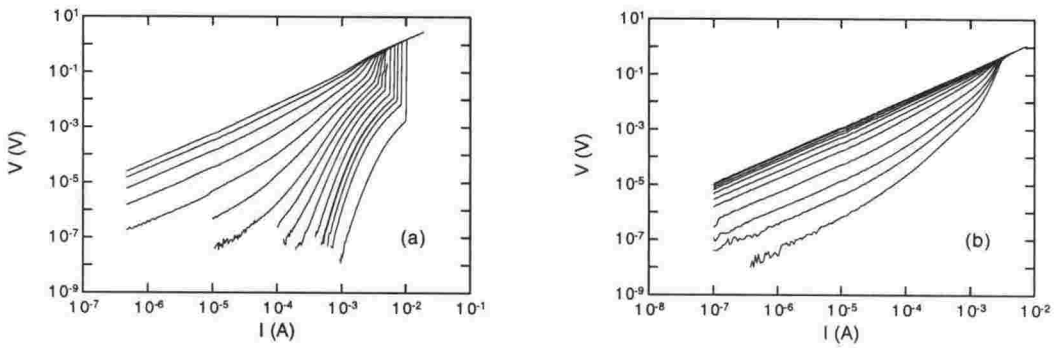

Figure 6.19: (a) IV curves measured at 1.373 K for sample 60/3G1. From right to left the curves correspond to fields of 0.0035, 0.015, 0.025, 0.035, 0.055, 0.085, 0.11, 0.14, 0.17, 0.2, 0.25, 0.3, 0.35, 0.4 and 0.45 T. (b) IV curves from the same sample measured at 1.570 K. From right to left the curves correspond to fields of 0.015, 0.025, 0.035, 0.055, 0.085, 0.11, 0.14, 0.17, 0.2, 0.25 and 0.3 T. Note the absence of downwards sloping IV curves at the higher temperature.

The anisotropy caused by the layering in sample 60/3G1 means that the typical length scales for vortex fluctuations and pinning along the field axis are reduced relative to the isotropic case. The thickness of this sample is about twice that of sample 2/G6 which displayed strong signs of 3D vortex glass behaviour, so it can be concluded that 60/3G1 is even more likely to display a true phase transition at the vortex glass melting temperature. Figure 6.19(a) shows a set of IV curves for this sample taken in various perpendicular fields at 1.373 K, while Figure 6.19(b) shows a similar set taken at 1.570 K. The low temperature IV curves are indeed of the form predicted by the vortex glass model, with upward curvature as the current is decreased at high fields and downward curvature in the low field glass phase. The vortex glass scaling laws have been applied to these and other similar sets of IV curves covering a range of fields and temperatures and in each case a reasonable scaling collapse is observed using the values $z = 6.0 \pm 0.5$ and $\nu = 1.2 \pm 0.1$, both well within the typical range seen in other systems. A melting line of the form $H_g = 1.6(T_c - T_g)^{2.2}$ has been determined and this coupled with the universality of the scaling parameters allows the vortex glass scaling to be performed at constant temperature rather than constant field. The results of the scaling of a set of curves taken at 1.456 K is shown in Figure 6.20(a). Overall the scaling collapse is excellent although the same deviation can be seen at high currents as was observed in sample 2/G6.

The IV data in Figure 6.19(b) look somewhat different to the low temperature set in Figure 6.19(a) in that none of the curves show a downward slope. This

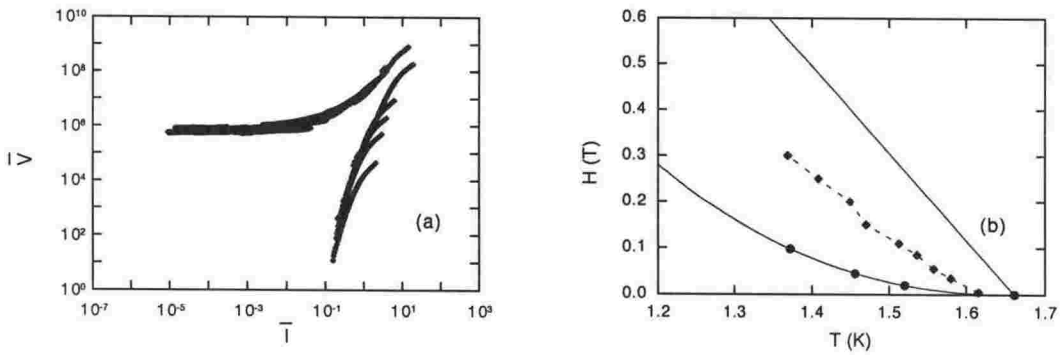

Figure 6.20: (a) Scaling collapse of a set of IV curves taken from sample 60/3G1 at 1.456 K. The scaling parameters are $z = 6.0$, $\nu = 1.2$ and the melting temperature has been determined at each field from the inversion of the melting line equation given in the text. (b) Perpendicular field phase diagram for sample 60/3G1. The upper solid line is H_{c2}, the diamonds show the crossover from activated to non-activated behaviour and the circles show H_g. The lower solid curve is a power law fit to the melting line.

provides evidence that a vortex glass phase may not exist at all in this sample at temperatures close to T_c. As the temperature was increased the parallel critical field of this sample was shown to undergo a crossover to a two-dimensional phase where no vortex glass would be expected, although the crossover occured at a temperature well above 1.570 K. Nevertheless the change in the nature of the IV curves may indicate that the vortices are entering a state where the relevant bending lengths are greater than the total sample thickness so that no 3D vortex glass phase can exist. Note that the vortex glass melting field also approached zero well below T_c in sample 2/G6.

The perpendicular field phase diagram of sample 60/3G1 is shown in Figure 6.20(b). As expected the phase diagram is very similar to that of sample 2/G6 although the melting line of sample 60/3G1 actually lies closer to the critical field than that of 2/G6 at similar values of T/T_c. This may be related to the finite size effects which are important in the thinner sample. The crossover line between thermally activated and non-activated behaviour is also shown in Figure 6.20(b) and has a similar form to the corresponding line in the other samples.

Thus far all of the samples have displayed evidence of three-dimensional behaviour in at least some regions of the phase diagram, due either to large superconducting layer thicknesses or to strong interlayer coupling. To conclude this section on the perpendicular field vortex states and dynamics the thicker samples are compared to samples 5/G1, 5/G2 and 29/2G4 which have very thin, decoupled superconducting layers and are thus expected to be fully two-dimensional. A

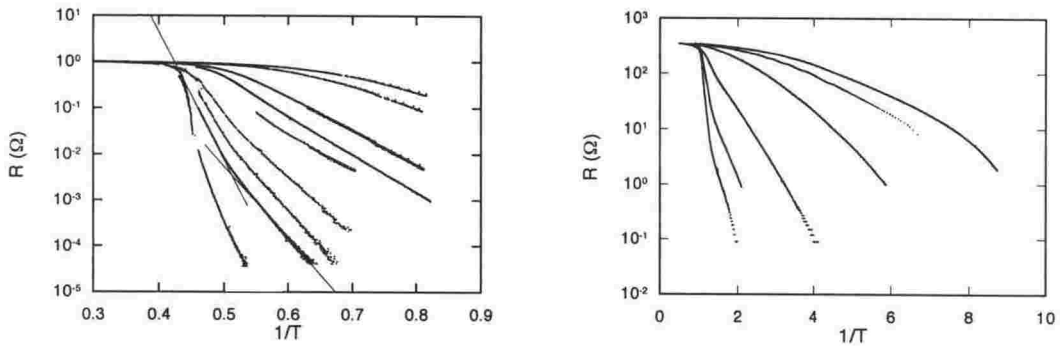

Figure 6.21: Arrhenius plots for three decoupled multilayers with thin superconducting layers. (a) Samples 5/G1 and 5/G2 combined. From left to right the curves correspond to perpendicular fields of 0.005, 0.03, 0.05, 0.1, 0.2, 0.3, 0.5, 1.0 and 1.2 T. Note the change in the activation energy at T_x which occurs in the low field curves. The solid lines correspond to fits to the two different activated regions at 0.2 T, with the point where the lines cross defining T_x. (b) Sample 29/2G4. From left to right the curves correspond to perpendicular fields of 0, 0.075, 0.25, 0.7, 0.95 and 1.05 T. This sample also shows a change in the Arrhenius plot slope at T_x.

perpendicular field Arrhenius plot for the two similar samples 5/G1 and 5/G2 is displayed in Figure 6.21(a) where the data have been combined together and normalised to R_n, while Figure 6.21(b) shows an Arrhenius plot for sample 29/2G4. A thermally activated resistivity is evident at low fields and temperatures on both plots, but more strikingly there is a sudden change in the slope of the curves at a field dependent temperature T_x. As the field is increased T_x moves closer and closer to the non-activated region until the change in slope is no longer observable. A change from one slope to another on the Arrhenius plot implies a change in the dominant dissipation mechanism with a corresponding change in the activation energy. Similar kinks have been observed in the Arrhenius plots of several different layered systems in which the change in activation energy has been attributed either to a dimensional crossover [24] or to 2D vortex lattice melting [20, 30]. It will be shown below that neither of these scenarios is applicable here and instead the crossover at T_x is due to a change in the dominant contribution to the resistivity from two competing modes of vortex motion.

The activation energies of samples 5/G1 and 5/G2 measured at temperatures below and above T_x ($U_1(H)$ and $U_2(H)$ respectively) are shown as a function of field in Figure 6.22. The values of $U_1(H)$ and $U_2(H)$ converge at a field of about 0.5 T above which the activation energy corresponds fairly closely to the extrapolation of $U_1(H)$. The lower solid line shows a fit of the form $U_1(H) = 8.4 \times \ln(2.5/H)$. This is similar to the field dependence of the activation energy observed in samples 6/G2 and 30/3G4 in which the activation barriers were interpreted as the energy required to create small dislocations within the

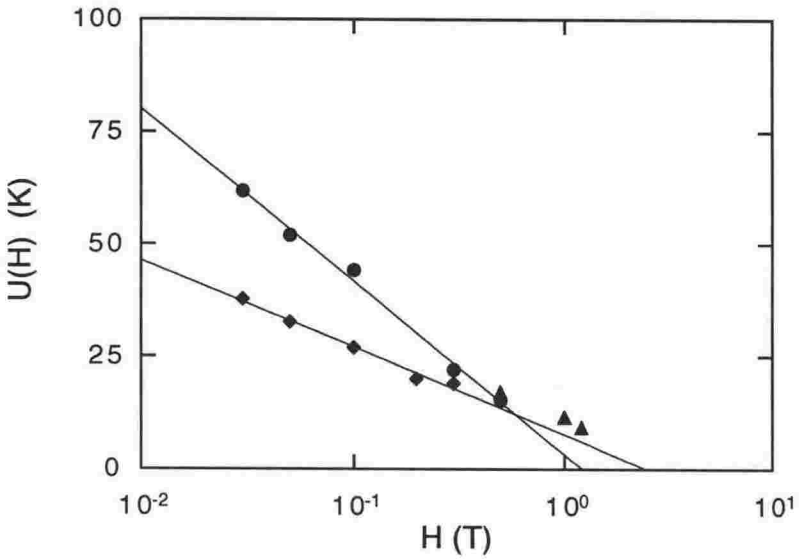

Figure 6.22: The activation energies (in Kelvins) for samples 5/G1 and 5/G2. The diamonds represent the activation energy at temperatures below T_x ($U_1(H)$) while the circles represent the activation energy at temperatures above T_x ($U_2(H)$). The high field data represented by the triangles fit fairly closely onto the extrapolation of $U_1(H)$.

2D vortex solid. In those samples the fitted coefficient of the logarithmic field dependence was proportional to d_s/λ_{ab}^2 and substitution of the relevant parameters shows that the coefficient of $U_1(H)$ scales in the same way. The dissipation mechanism in samples 5/G1 and 5/G2 at temperatures below T_x must therefore be the same as that in the thicker samples i.e. motion of dislocations of size $\sim a_0^2/\xi_{ab}$ for which the energy of creation is finite due to the disorder in the vortex lattice.

The activation energy at temperatures above T_x is also best fitted by a logarithmic equation of the form $U_2(H) = 16.7 \times \ln(1.2/H)$ where it should be noted that the coefficient is almost exactly twice that of $U_1(H)$. So far the motion of disorder induced free dislocations is the only mode of flux creep which has been shown to have a logarithmic field dependence of the activation energy. The model which led to the logarithmic field dependence implied that in the limit of strong disorder only the smallest dislocations remain bound in pairs. The activation energy for creating the bound pairs can be approximated from Equation 5.54 by making the substitution $r = a_0^2/\xi_{ab}$, leading to [148]

$$U_{pair} \simeq \frac{\Phi_0^2 d_s}{16\pi^2 \mu_0 \lambda_{ab}^2(T)} \ln\left(\frac{H_0}{H}\right) \tag{6.6}$$

with $H_0 \simeq H_{c2}$. Equation 6.6 is preferred over the similar Equation 5.55 which

is based on the thermal average over dislocation pairs of all sizes. Because this mode involves two dislocations the activation energy is exactly twice that of the free dislocations which are responsible for $U_1(H)$ (Equation 5.58), so $U_2(H)$ may be identified with the barrier required to create small dislocation pairs.

Figure 6.22 shows that $U_2(H)$ is actually greater than $U_1(H)$ at all fields below 0.5 T despite the fact that the resistivity is larger above T_x than below. This implies that above T_x the higher barriers are offset by a much larger value of R_0 in the equation for the activated resistivity $R = R_0 \exp(-U/k_B T)$, where R_0 is determined by the density of activated units (e.g. dislocation pairs), the amount of flux in the activated unit and the size of the hopping process. The crossover at T_x occurs when the resistance due to the dissipation process governed by activation energy U_2 becomes larger than that governed by U_1. The crossover need not be associated with any phase transition such as layer decoupling or 2D melting, but only requires two competing modes of flux motion in which the relevant activation energies and the values of R_0 are of the right size. Evidently the value of R_0 is greater for the small dislocation pairs than for the free dislocations, thus enabling the crossover at T_x to be observed.

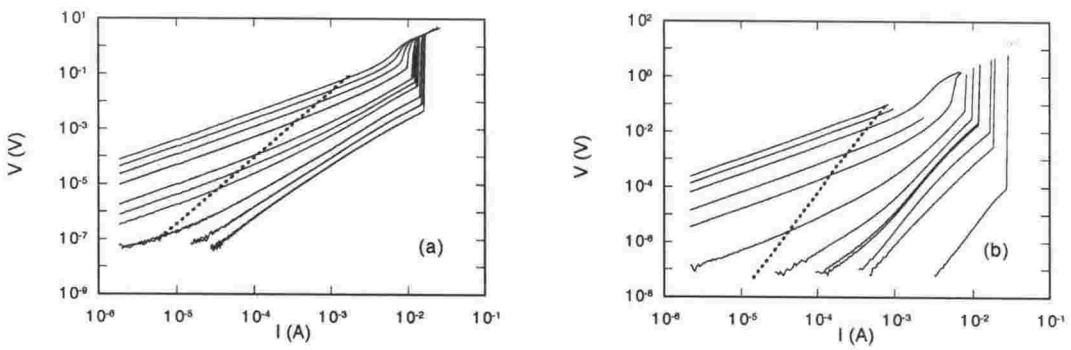

Figure 6.23: (a) IV curves measured at 1.71 K for sample 5/G1. From right to left the curves correspond to fields of 0.004, 0.01, 0.02, 0.05, 0.07, 0.1, 0.2, 0.3, 0.4 and 0.5 T. (b) IV curves measured at 1.245 K for sample 5/G2. From right to left the curves correspond to fields of 0, 0.011, 0.0198, 0.0493, 0.05, 0.1, 0.2, 0.5, 0.7, 1.0, 1.2 and 1.4 T. The dotted lines mark the points where the IV curves deviate from the low current linear behaviour.

The previous samples have shown that when the thickness of the superconducting layers is reduced the three-dimensional vortex glass correlations are restricted, making it natural to ask whether samples 5/G1 and 5/G2 exhibit the properties of a two-dimensional vortex glass. This question can be answered by comparing the IV curves of these samples to the predictions of the 2D vortex glass model, but it is also important to determine whether the observed form of the activated low current resistivity is consistent with the existence of finite

vortex glass correlations.

A set of perpendicular field IV curves taken from sample 5/G1 at 1.71 K is shown in Figure 6.23(a) and a set taken from sample 5/G2 at 1.245 K is shown in Figure 6.23(b). Despite the fact that some of the curves are measured at temperatures and fields well below H_{c2} there is no sign of the sharp downward curvature that was evident in each of the other samples. At most the zero field curves in Figure 6.23(b) show a power law dependence on the current due to the zero-field BKT transition, while all other curves display a linear low current resistivity followed by a non-linear region at higher currents. The absence of downward sloping IV curves indicates that the vortex lattice in these 2D samples is unstable against plastic flux motion over all of the observable phase diagram, and therefore there is no vortex glass transition at finite temperature. Any transition into a vortex glass state must therefore occur only at $T = 0$ as predicted in the 2D model.

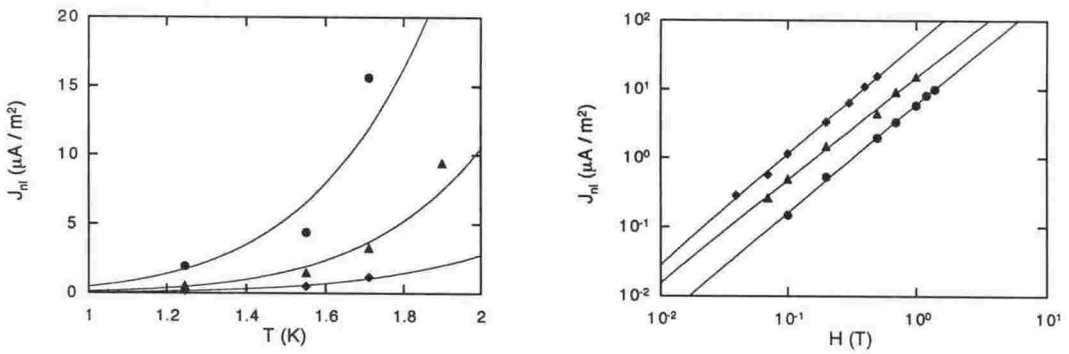

Figure 6.24: (a) The crossover current J_{nl} separating the linear and non-linear regions on the IV curves as a function of temperature for samples 5/G1 and 5/G2. From top to bottom the data sets correspond to fields of 0.5, 0.2 and 0.1 T. The solid lines show power law fits. (b) J_{nl} as a function of field. From top to bottom the data sets correspond to temperatures of 1.71, 1.55 and 1.245 K and once again the solid lines are fits to a power law.

A crossover from linear resistivity at low currents to non-linear resistivity at high currents is predicted to occur in the 2D vortex glass model when the length scale probed by the current becomes less than the 2D vortex glass correlation length ξ_{vg}^{2D}. The crossover current density J_{nl} where the IV curves first deviate from the extrapolated linear region at low currents has been extracted from the IV curves and is shown as a function of temperature in Figure 6.24(a) for several different fields. Clearly the temperature dependence is not consistent with the Anderson–Kim model which predicts $J_{nl} \propto T$, but instead fits more closely to a power law $J_{nl} \propto T^{6.0\pm0.5}$. The 2D vortex glass model does in fact predict a power law for the temperature dependence of J_{nl} (Equation 5.59), although the expo-

nent is expected to be equal to 3 rather than 6. It has been suggested that higher powers are possible [44], so the observed behaviour is not altogether inconsistent with the existence of 2D vortex glass correlations in these samples. The field dependence of J_{nl} is shown in Figure 6.24(b) for several different temperatures, where once again the measured points fit very well to a power law, this time with an exponent of 1.5 ± 0.1. This implies that $J_{nl} \propto 1/a_0^3$ whereas the predicted behaviour is a $1/a_0$ dependence on the intervortex spacing [124, 149].

The low current resistivity has been shown to correspond to the motion of dislocations of approximate size a_0^2/ξ_{ab}, where the activation barrier relates to the energy needed to create the dislocations rather than to overcome pinning forces. A thermally activated resistance is consistent with Equation 5.60 as long as the exponent p is equal to 1, which is indeed the value suggested by Fisher *et al.* [149], however in the 2D vortex glass model the activation barriers at low current correspond to the energy needed to move vortex segments of characteristic size ξ_{vg}^{2D}. This contrast between the source of the experimentally measured activation energy and the 2D vortex glass prediction would seem to imply that these samples do not show 2D vortex glass correlations. However it must be remembered that the creation of the free dislocations requires the displacement of the surrounding vortices, and it may be that this process does show features related to glass-like elastic vortex correlations. This might help to explain why the temperature dependence of J_{nl} shows glass-like non-linearity whereas the activation energy is not of the usual 2D vortex glass type. The overall conclusion at least is that the crossover to non-linear resistivity in the IV curves is more complex than the simple predictions of the Anderson–Kim flux creep model.

At the highest currents in Figures 6.23(a) and (b) there are clear signs of a return to linear behaviour, especially at the higher temperature where the thermal disorder of the vortices tends to average out the pinning forces. The resistivity just below the LO instability has been measured from the IV curves and found to be about half of the flux flow value given by Equation 5.30, although it does show the predicted linear field dependence. The corresponding low current resistivity ranges from 1% of the high current value at a field of 0.02 T to 95% of the high current value at 0.5 T. From this it can be concluded that a current induced crossover occurs from a pinned state where the resistance is dominated by motion of dislocations to a largely unpinned state with a freely moving flux lattice. At high fields the pinning is weak enough that the two states are practically indistinguishable i.e. the vortices are depinned without assistance from the current.

The phase diagram for samples 5/G1 and 5/G2 is shown in Figure 6.25 includ-

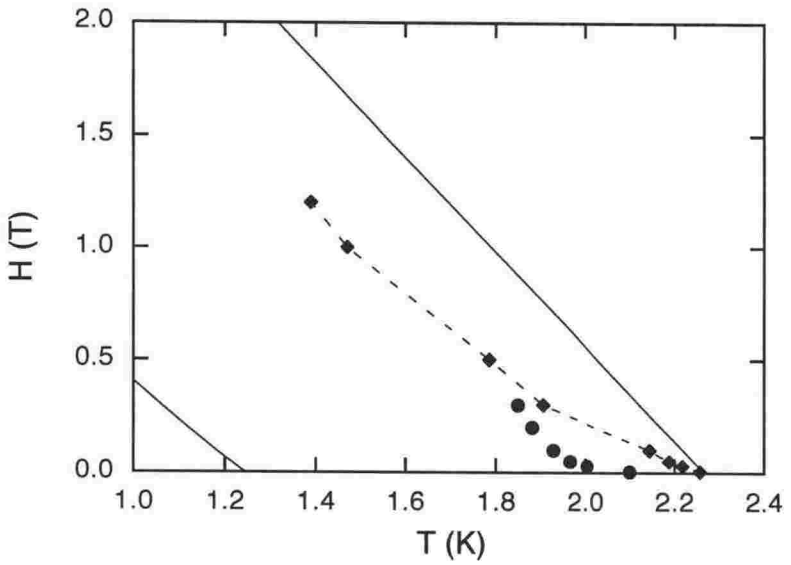

Figure 6.25: Perpendicular field phase diagram for samples 5/G1 and 5/G2. The upper solid line is H_{c2}, the triangles represent the boundary between the activated and non-activated resistivity and the circles represent T_x. The solid line to the left of the plot is the calculated position of the 2D melting line, which clearly falls well below T_x.

ing $H_{c2\perp}$ and the temperatures T_x at which the kinks in the Arrhenius plot occur. The solid line at the lower left of the figure is the predicted 2D melting line due to dislocation pair unbinding calculated from Equation 5.25 with $A = 0.64$ and using the full expression for the shear modulus c_{66}. Clearly the predicted melting line does not correspond to any of the features observed in these samples. The crossover line between the activated and non-activated resistivity is also shown on the phase diagram. For this sample the crossover line corresponds to a rather high resistance of the order of 0.2–0.3 R_n indicating that the activated behaviour extends over a much larger fraction of the transition than in the thicker samples.

6.3.2 Parallel Fields

The intrinsic pinning in layered superconductors is expected to lead to a considerable reduction in the parallel field resistivity relative to the isotropic case. For this reason much of the theoretical and experimental work performed to date has concentrated on the perpendicular field orientation, as it is the perpendicular field component which tends to limit the superconductivity. Of course this also means that parallel fields offer the greatest possibility of enhancing variables such as the critical current or field for use in applications, so a study of this orientation is clearly of interest. A complete study of the parallel field behaviour along the

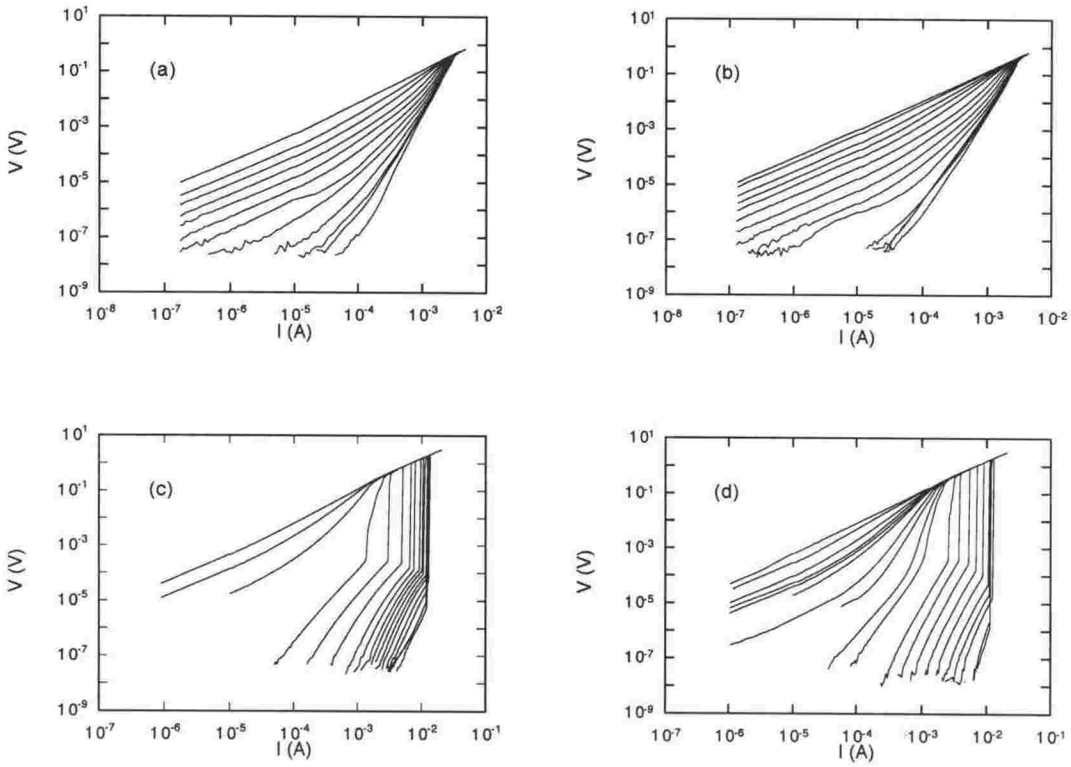

Figure 6.26: Parallel field IV curves for sample 60/3G1. (a) 1.590 K, current parallel to field. The curves range from 0.005 (far right) to 0.35 T (far left). (b) 1.590 K, current perpendicular to field. The curves range from 0.005 to 0.40 T. (c) 1.460 K, current parallel to field. The curves range from 0.005 to 0.70 T. (d) 1.460 K, current perpendicular to field. The curves range from 0.005 to 0.70 T.

same lines as the perpendicular field is beyond the scope of this work, but a few points will be made here to highlight the differences between the two different orientations.

Figure 6.26(a) shows a set of IV curves taken from sample 60/3G1 at 1.590 K in different parallel fields where the current is applied in the same direction as the field. Figure 6.26(b) shows a similar set of IV curves from sample 60/3G1 with the only difference being that the current is now directed perpendicular to the field. Both sets of curves are remarkably similar despite the different current orientations. Figures 6.26(c) and (d) show similar sets of IV curves to the above, but this time taken at a lower temperature of 1.460 K where two qualitatively different regimes are clearly evident. If only the high field data are considered then the behaviour is quite similar to that observed at 1.590 K i.e. the curves are all linear at low currents followed by a non-linear rise and an eventual convergence to the normal state resistance at a field independent current. At low fields the IV curves display downward curvature at low currents indicative of vortex glass

like behaviour. At higher currents an LO instability is present which resembles that seen in the perpendicular field data, however in this orientation the voltage jump actually corresponds to a much larger change in resistance. The crossover between the low and high field regimes is rather sudden indicating that they may be separated by a phase transition in the magnetic state.

Before drawing any conclusions from this data it should first be noted that the total thickness of the sample is considerably less than the c-axis penetration depth, so it is not possible to form well defined vortices parallel to the layers. Nevertheless the IV characteristic is strongly field dependent at constant temperature indicating that the field does penetrate throughout the sample[12], possibly in a form closely resembling the usual Abrikosov vortices but with a cutoff in the extent of the screening currents. This makes it difficult to fully interpret the parallel field data, but the following observations can be made.

Firstly the difference between the 1.590 K and the 1.460 K data sets resembles the differences between the corresponding perpendicular field measurements which it was suggested could be related to a crossover from two- to three-dimensional vortex dynamics. The relevant object in the parallel field case may be the perpendicular component of the kink structures which nucleate vortex motion across the layers (see Section 5.3.7). At high temperatures such a kink structure may in fact extend across the whole sample. The similarity between the data in the two different current orientations also supports the notion that the dissipation is dominated by the thermal excitation of vortex segments perpendicular to the layers (and therefore perpendicular to the current). The glass-like current dependence observed at low fields and temperatures is also in agreement with the behaviour predicted in Section 5.3.7. Finally the parallel field activation energies have been determined for this sample and were found to be equal to a field independent value of about 1400 K for parallel fields between 0.015 and 0.4 T, decreasing to around 700 K at 0.7 T. These are considerably higher than the perpendicular field barriers demonstrating the natural reduction in dissipation in the parallel orientation. Overall this speculative picture clearly calls for a more detailed study of the parallel field response of a thin multilayer system, including a determination of the vortex structure and also an investigation of the possible vortex states.

Figure 6.27 shows a set of IV curves taken from the strongly layered sample 6/G2 at a temperature of 1.3 K. The IV curves differ markedly from the perpendicular case in that significant dissipation is only apparent very close to H_{c2}

[12]Note that the measured anisotropy of this sample is far too low for the dissipation to be related simply to a small perpendicular field component caused by misalignment.

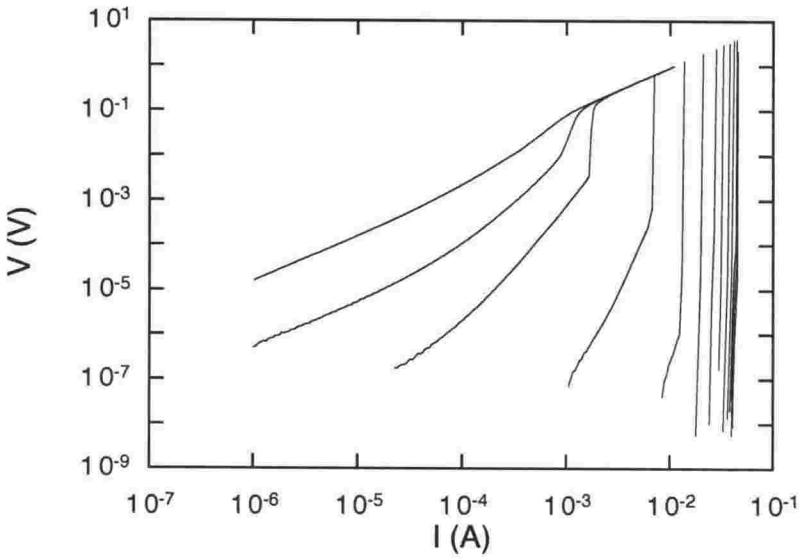

Figure 6.27: Parallel field IV curves for sample 6G2 measured at 1.3 K. From right to left the curves correspond to fields of 0, 0.5, 1.0, 1.5, 2.0, 2.5, 3.0, 3.5, 4.0, 4.5, 4.75, 4.83, 4.9 T. Almost no dissipation is observable below the instability point until very close to H_{c2}.

($H_{c2\|} \approx 4.9$ T at 1.3 K) indicating that the field is effectively trapped between the superconducting layers. The temperature 1.3 K is well below the zero field BKT transition of this sample, so there is little energy to create vortex-antivortex pairs within the superconducting layers. These pairs provide the nucleus for flux motion in the parallel field orientation (see Section 5.3.7) so their absence explains the very low dissipation levels. As the field is lowered the observable dissipation region becomes smaller and smaller until the IV curves actually jump to the normal state at the instability point without any intermediate resistive phase. At the very lowest fields a small dissipation region again becomes apparent prior to the instability, although the cause of this is unknown.

6.4 Larkin-Ovchinnikov Instabilities

A complete description of the vortex state must include the response of the vortices to very high applied currents up to and exceeding the depinning critical current. The aim of this section is to examine the high current regime in each of the multilayer samples and to compare the results with the Larkin-Ovchinnikov (LO) theory introduced in Section 5.3.9. The LO theory predicts a fundamental instability in the rapidly moving vortex system which sets an absolute upper limit on the current which can be applied while still maintaining signs of superconductivity. The IV curves displayed in the previous sections do indeed display an upturn at high currents which has previously been shown to agree with the LO theory [141], although the justification for this statement is repeated here for completeness.

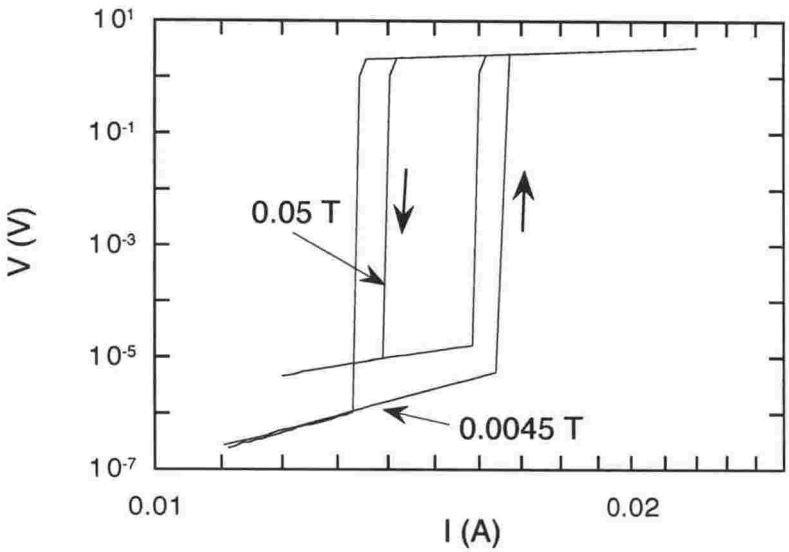

Figure 6.28: A closeup of the parallel field instability point in sample 60/3G1 in two different fields at a temperature of 1.424 K. There is very little hysteresis despite the huge difference between the power levels on the upwards and downwards current sweeps.

To demonstrate that the instability is of the LO type it is first necessary to eliminate any other possible sources of a sudden jump in the IV characteristic. Figure 6.28 shows an enlarged view of the instability point for two different parallel field IV curves taken from sample 60/3G1 at a temperature of 1.424 K. The instability is observed on both the upward and the downward sweeps with only a small difference between the current at which it occurs in either case despite the fact that the power levels on either side of the transition differ by more than 5

orders of magnitude. The other samples also show similar results with little or no hysteresis. This rules out Joule heating as the source of the instability, which is a result of the fact that the measurements have been performed with the samples immersed directly in liquid helium to maximise cooling. The depairing currents have been calculated for some of the samples using Equation 1.1 and in every case were found to be too large to be related to the abrupt voltage changes. The Josephson behaviour used to explain the sudden jumps in resistance observed in some highly anisotropic high-T_c samples [150] is not appropriate here either as the voltage upturns have been observed in the unlayered alloy sample 2/G6 as well as the multilayer samples. Depinning, accompanied by vortex lattice crystallisation, has also been shown to result in jumps in the resistance [8, 10]. For samples 5/G1 and 5/G2 a crossover to a free flux flow state was observed at high currents well before the instability, so depinning can not be the cause of the voltage jumps observed here. Furthermore the transition always involves a jump to a resistance close to the normal state value whereas in a depinning transition the jump would be expected to be to the flux flow resistance. Thus it is concluded that the LO theory is the most promising to pursue in analysing the high current instability in these samples.

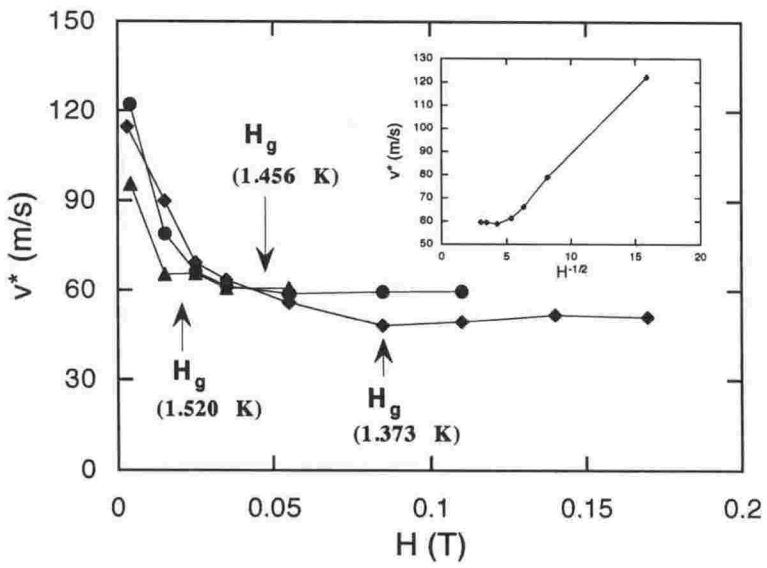

Figure 6.29: The measured critical vortex velocity for sample 60/3G1 in a perpendicular field. The diamonds correspond to a temperature of 1.373 K, the circles to 1.456 K and the triangles to 1.520 K. The vortex glass melting field is marked by an arrow on each curve. The inset shows the 1.456 K data plotted versus $H^{-1/2}$ which is linear at fields below H_g.

One of the main results of the LO theory is the derivation of the dependence

of the critical vortex velocity v^* on the electron inelastic scattering time τ_{in} (see Equation 5.65). The values of v^* have been determined from the IV curves of sample 60/3G1 using Equation 5.66 where at low fields V^* is defined as the voltage just before the resistance jump, while at high fields V^* is defined as the voltage just before the point where the IV curve shows a rapid change in slope. Figure 6.29 shows a plot of v^* as a function of the perpendicular applied field for sample 60/3G1 where the different curves correspond to different temperatures. Each of the curves displays similar behavior, decreasing with field at first before levelling off to an almost temperature independent value of about 50-60 ms^{-1}.

For the pure Ta multilayers the value of τ_{in} has been determined previously from a study of the temperature dependence of the normal state conductivity [17, 36], thus allowing a comparison between the measured and theoretical values of v^*. At low temperatures the inelastic scattering processes are dominated by electron-electron scattering events for which the 3D value of τ_{in} is given at 1 K as 1.25×10^{-8} s. The same source gives the value of the diffusion constant D as 1.2×10^{-4} $\mathrm{m}^2\mathrm{s}^{-1}$. Combining these values into Equation 5.65 yields predictions for v^* of 72, 66 and 60 ms^{-1} at temperatures of 1.373, 1.456 and 1.520 K respectively which are in remarkably good agreement with the experimental results, especially considering the large uncertainty associated with both D and τ_{in}. The observed lack of a clear temperature dependence of v^* does not agree with the predictions of the LO theory, however it should be remembered that τ_{in} is a decreasing function of temperature which offsets the behaviour given explicitly in Equation 5.65. Overall the measured results provide very compelling evidence that the instability is indeed of the LO type.

The values of the critical vortex velocity have also been extracted from the IV data for the other samples and, similarly to sample 60/3G1, a region is observed in each where v^* is approximately independent of field. The values of v^* determined in this region are shown as a function of temperature in Figure 6.30 for samples 2/G6, 6/G2, 60/3G1 and 5/G1 and 5/G2 combined. The overall magnitude of the critical velocity provides an estimate of the ratio $(D/\tau_{in})^{1/2}$ for each of the samples, however there is no clear trend in the values which would allow a determination of the dependence of $(D/\tau_{in})^{1/2}$ on the layer thicknesses. This is not entirely surprising as the inelastic scattering time depends on the sample composition and the level of impurities as well as the dimensionality, and the former are not held constant between the samples. However one trend which is evident is a slight increase in v^* with increasing temperature which indicates that the temperature dependence of τ_{in} is dominating the term $(1 - T/T_c)^{1/2}$ in Equation 5.65.

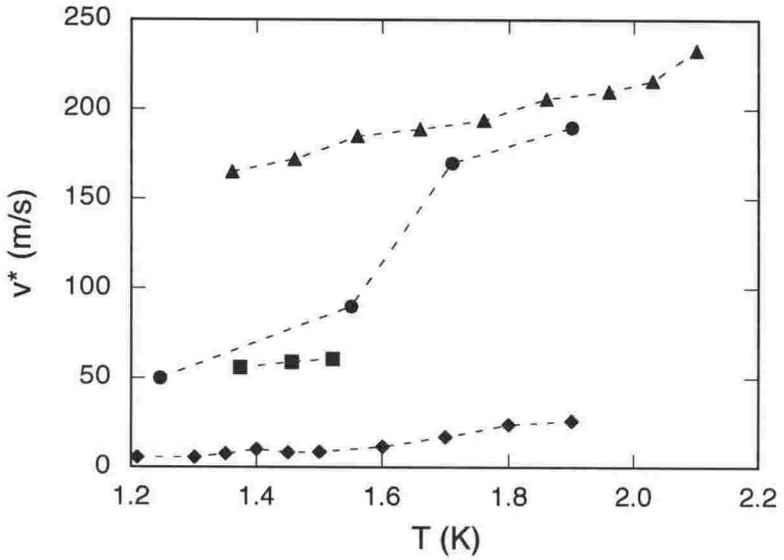

Figure 6.30: A comparison between the measured perpendicular field LO critical vortex velocities for several samples. The diamonds are from sample 6/G2 in a field of 0.7 T, the squares are from sample 60/3G1 at 0.055 T, the circles are a combination of samples 5/G1 and 5/G2 at 0.2 T and the triangles are from sample 2/G6 at 0.8 T.

A detailed inspection of any of the sets of IV data presented in the previous section (e.g. Figure 6.19(a)) reveals several features characteristic of the IV curves at the instability point. At low fields the jump in resistance is extremely abrupt having no measureable width irrespective of the size of the current steps, and the transition is always to a resistance which closely approaches the normal state value rather than the flux flow resistivity. As the field is increased the abrupt transitions gradually begin to broaden until at the highest fields they become almost imperceptible, although once again the resistance above the transition point closely approaches the normal state value. Similar behaviour can also be observed if the IV curves are plotted at a single field and a range of temperatures, leading to the conclusion that the broadening occurs as H_{c2} is approached. Finally, both the voltage V^* and the current density J^* at which the instability takes place depend on the applied field and temperature. Some of these features are predicted by the LO theory, such as the variation in V^* with field, however other features are not directly predicted and require further investigation.

A useful place to begin is the consideration of the expected behaviour below the instability point where the LO theory makes specific predictions regarding the form of the IV curves which should be observed. In the absence of any pinning forces the IV curves are described by the equation [15,16,35]

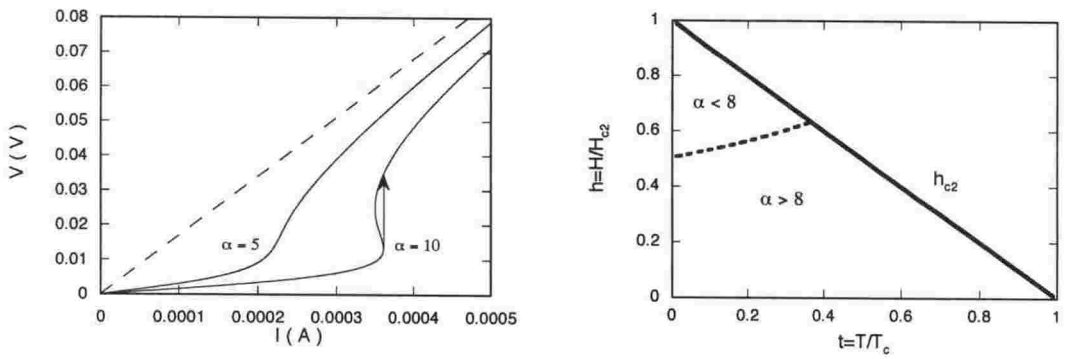

Figure 6.31: (a) IV curves calculated according to Equation 6.7, showing the characteristic backbending shape at low field. The curve on the left has $\alpha = 5$, while the curve on the right has $\alpha = 10$. Both curves have $R_n = 170\,\Omega$ and $V^* = 0.01\,V$. The dashed line represents the normal state resistance. (b) The boundary on the magnetic phase diagram separating the regions where $\alpha > 8$, which are expected to display sharp transitions at the LO instability, and $\alpha < 8$ where the transitions are broadened.

$$I = \frac{V}{R_n}\left[\alpha \frac{1}{1+(V/V^*)^2} + 1\right] \tag{6.7}$$

where R_n is the normal state resistivity and α is given by

$$\begin{aligned} \alpha &= \frac{4.04 H_{c2}}{H(1-T/T_c)^{1/2}}, \quad H \ll H_{c2} \\ \alpha &= \frac{\pi^5 e D}{130\zeta(3)k_B}\left(-\mu_0 \frac{dH_{c2}}{dT}\right), \quad H \lesssim H_{c2} \end{aligned} \tag{6.8}$$

with D the electron diffusion coefficient, $R_{ff} = R_n B/H_{c2}$ the usual flux flow resistivity which occurs when $\eta = \eta(0)$, and $\zeta(3) = 1.202$. Differentiation of this equation with respect to V shows that the IV curve has two critical points given by

$$V^2 = V^{*2}\left(\frac{(\alpha-2) \pm \sqrt{\alpha^2 - 8\alpha}}{2}\right). \tag{6.9}$$

When $\alpha > 8$ (i.e. at low fields) the solutions to Equation 6.9 are real and the IV curve bends backwards as shown by the right hand curve in Figure 6.31(a). The lower critical point corresponds to the LO instability where the voltage makes an abrupt jump to the upper branch of the IV curve on which the resistance approaches the limiting value R_n (shown by the dashed line). At higher fields where $\alpha < 8$ the back-bending is no longer evident, and instead a rapid but continuous rise in the IV characteristic is observed as shown by the left hand

curve in Figure 6.31(a). The values chosen for R_n ($170\,\Omega$) and V^* ($0.01\,V$) are typical of the Ta_xGe_{1-x}/Ge multilayer systems studied here.

It should be noted that two different expressions for the IV curves were presented in the original LO paper, the first of which has been discussed above (Equation 43 in Ref. [15], Equation 1 in Ref. [35]). The second expression (Equation 53 in Ref. [15]), which has subsequently been used by several other authors [137,138], is equivalent to

$$I = \frac{V}{R_{ff}} \left[\frac{1}{1 + (V/V^*)^2} + c \left(1 - \frac{T}{T_c} \right)^{1/2} \right] \tag{6.10}$$

where c is a constant of order unity. An analysis of this equation shows that there are no critical points so it does not describe a back-bending IV curve, and furthermore the limiting value of the resistivity at large V is $R_{ff}/c(1 - T/T_c)^{1/2}$, whereas the experimental data clearly show that the resistivity tends to R_n at large vortex velocities.

Equation 6.8 can be used to predict the crossover between sharp and broadened transitions in the IV curves. Figure 6.31(b) shows the line on the magnetic phase diagram where $\alpha = 8$ which divides the points where the transition at the LO instability is expected to be sharp and the points where it is expected to be broad. This is based only on the low field expression for α. Inclusion of the high field expression would have led to an additional region close to the phase boundary where $\alpha < 8$ at all temperatures.

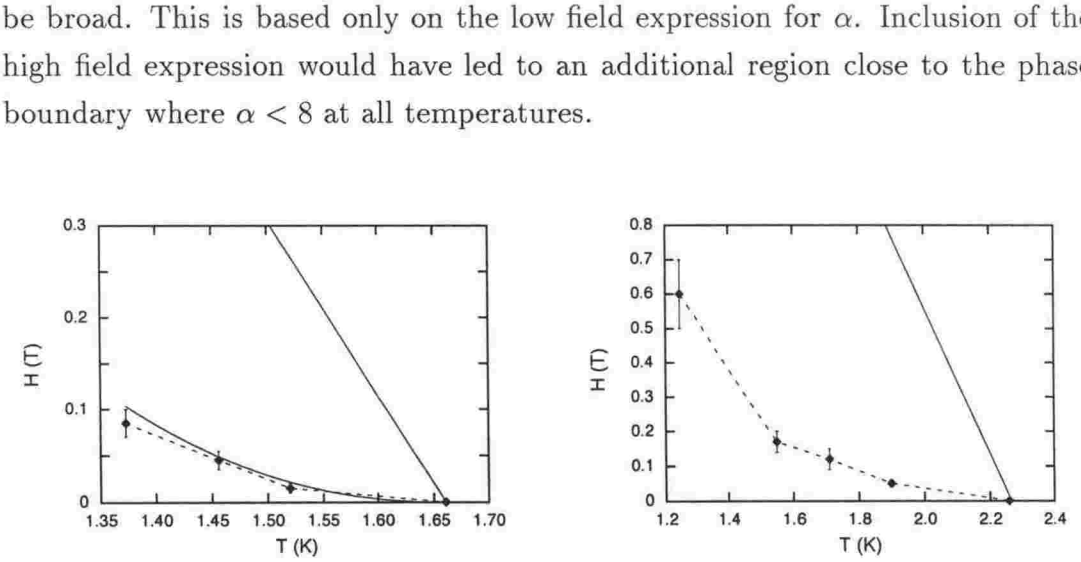

Figure 6.32: (a) The measured position of the onset of broadening in the LO instability for sample 60/3G1. The upper solid line is H_{c2} and the lower solid curve is the vortex glass melting line. (b) The position of the onset of broadening in the LO instability for samples 5/G1 and 5/G2. The solid line is H_{c2}.

The measured boundaries between the sharp and broad instabilities are shown for sample 60/3G1 in Figure 6.32(a) and for samples 5/G1 and 5/G2 in Figure 6.32(b) where H_{c2} has been included also. Clearly the measured boundaries

do not correspond to the predicted behaviour shown in Figure 6.31(b) indicating that further processes are involved. Also shown in Figure 6.32(a) is the vortex glass melting line determined from the scaling analysis in Section 6.3.1, which shows remarkable similarity to the broadening line. This correspondence can in fact be seen in the IV data for this sample in which the downward sloping curves always correspond to sharp transitions while the upward sloping curves correspond to the broad transitions. For samples 5/G1 and 5/G2 the broadening line does not correspond to any observed transition, however there is a fairly close correlation between the broad transitions and the existence of pronounced non-linearity in the IV curves at intermediate currents. These observations make it clear that a complete description of the instabilities in these samples must include the effects of pinning forces as well as the vortex viscosity term. This is made even more clear by an inspection of the 0.7 T IV curves for sample 6/G2 presented in Figure 6.15(a) which show that just below the instability the IV curves follow a power law dependence characteristic of vortex glass behaviour rather than the linear IV characteristic that would be expected if there were no pinning forces. The fact that pinning forces are able to influence the instability is a reflection of the low values of the critical vortex velocity. These velocities can be reached while pinning is still appreciable.

To date few attempts have been made to include the effects of pinning on the shape of the LO IV curve, with most attempts being restricted to the subtraction of a critical current I_c from the left hand side of Equation 6.7. This is equivalent to treating the pinning as a constant drag force independent of the vortex velocity. An accurate treatment of pinning on the other hand, must take into account the relationship between the pinning force and the size of the vortex core. The collective pinning theory (Section 5.3.1) provides a means of relating the pinning force on the vortex lines to the coherence length. Equation 5.34 shows that the single vortex collective pinning energy is an increasing function of the coherence length, so as the vortex velocity increases and the vortex cores begin to shrink there will not only be a decrease in the viscous drag but also in the size of the pinning force. Therefore the inclusion of pinning forces adds a velocity dependent term to the vortex equation of motion which could significantly modify the shape of the IV curves. The overall strength of the pinning forces depends on the vortex regime, for example a significant reduction in pinning occurs upon melting of the vortex glass, which may explain the correlation between the onset of broadening in the LO instabilities and the vortex glass melting transition[13] [141].

[13]The agreement between the measured and theoretical values of the critical velocity discussed above was based on data at fields well above the melting line where pinning is not

A further effect which is worthy of consideration is the distribution of vortex velocities which exist in the vortex liquid state. It has been shown in the previous sections that as the field or temperature are increased towards H_{c2} the vortex lattice can become unstable to plastic vortex motion, due either to melting of the vortex glass in 3D or to the formation of dislocations in 2D. The rather jumpy transitions observed in the instability just at the onset of broadening are in fact quite suggestive of some form of plastic flux motion where some parts of the vortex lattice undergo the instability ahead of other parts. While the above arguments fall far short of providing a rigorous theoretical analysis of the effects of pinning and thermal disorder on the high current properties of the vortices they do at least highlight some of the important features which a complete theory must include.

It was noted above that the measured critical vortex velocity shows a fairly strong field dependence at low fields (see Figure 6.29), whereas no such effect is predicted by the LO theory. As discussed in Section 5.3.9 such a field dependence has been predicted by Bezuglyj and Shklovskij [134] and also by Doettinger *et al.* [138]. In the first instance the field dependence is caused by heating effects in the vortex cores whereas the second theory is based on a spatially inhomogeneous quasiparticle distribution due to the localisation of excitations within the vortex cores. To help determine which of these effects is relevant (if any) the data at 1.456 K have been replotted versus $H^{-1/2}$ in the inset to Figure 6.29 where a linear dependence can be seen at low fields. The data at the other temperatures show similar behaviour although with slightly more scatter. This linear dependence on $H^{-1/2}$ agrees with the predictions of Doettinger *et al.*, however it is also shown on the plot that the point at which the curves flatten off corresponds closely to the vortex glass melting field whereas the theory predicts that the flattening off occurs when the intervortex spacing becomes small enough that the inhomogeneous quasiparticle distribution is averaged out by the flowing vortices. A natural explanation for this coincidence is that the averaging of the quasiparticle distribution is in fact performed by the thermal motion of the vortices in the liquid state which allows the vortex core to sample a much larger fraction of the surrounding superconductor. These results indicate that the observed field dependence of the critical vortex velocity is best interpreted in terms of the theory of Doettinger *et al.*. It is interesting to note however that the values of v^* in sample 2/G6 actually show a sudden decrease as the temperature is raised above the lambda point of liquid helium. This is most easily attributable to a change in

expected to be significant.

the cooling power of the liquid helium leading to a decrease in v^* as predicted by Bezuglyj and Shklovskij. Therefore both theories seem to be of some relevance to this system.

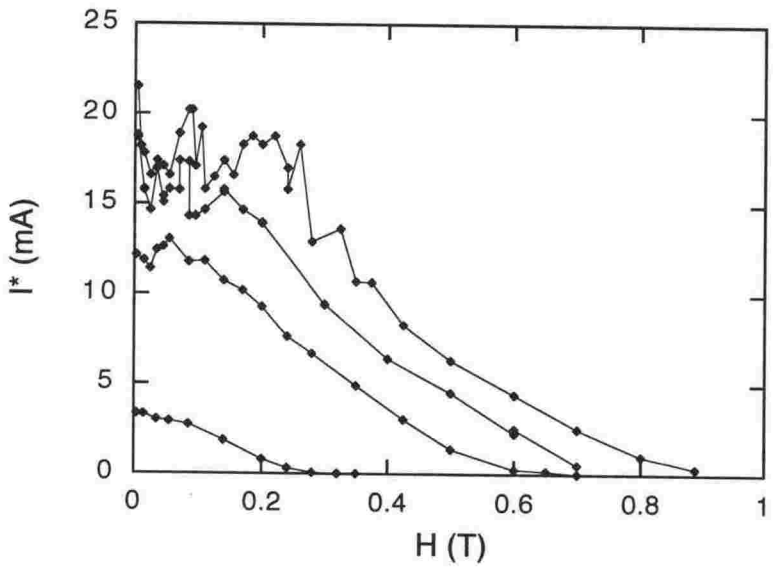

Figure 6.33: The parallel field critical current at the LO instability for sample 60/3G1. From top to bottom the curves correspond to temperatures of 1.373, 1.410, 1.460 and 1.550K. Note the non-monotonic behaviour at low temperatures and fields.

To finish this section on Larkin-Ovchinnikov instabilities a brief consideration is given of the parallel field orientation. Parallel field IV curves for the decoupled sample 6/G2 have already been presented in Figure 6.15 where it was shown that the voltage jumps from an unmeasureably low value to the normal state as the instability is reached, corresponding to a remarkably low value for v^*. It therefore seems even clearer in the parallel field case than in the perpendicular case discussed above that additional effects are important in determining the behaviour of the instability. Further investigation of this field orientation, especially in strongly anisotropic samples, is clearly warranted.

Several sets of parallel field IV curves taken from sample 60/3G1 were also presented in Section 6.3.2. At low fields and temperatures these curves displayed an instability similar to the one observed in perpendicular fields, however the jump in resistance was over a larger scale in the parallel field case. Furthermore an inspection of the high current region in Figure 6.26(c) shows that the current I^* is in fact non-monotonic in the applied field. I^* is plotted as a function of the applied field in Figure 6.33 where the different curves correspond to different temperatures. Clearly the non-monotonic region is confined to low fields and

temperatures indicating a possible change in the vortex state. This behaviour is observed most strongly when the field and current are parallel so that there is no Lorentz force, whereas Figure 6.26(d) shows that when the current is perpendicular to the field there is only a hint of non-monotonic behaviour in I^*. Once again this suggests that a description of the instability solely in terms of the viscosity force is not adequate in the parallel case, and instead the complicated activation barriers and pinning forces arising in this orientation must also be considered.

Chapter 7

Conclusions

The main aim of this thesis was to study the superconducting properties of a highly disordered low-T_c multilayer system in order to examine the effects of layering and reduced dimensionality on superconductivity in type-II materials. The multilayer system studied consisted of layers of amorphous Ta or Ta_xGe_{1-x} ($x \approx 0.3$) interleaved with amorphous Ge where the individual layers ranged in thickness from 17 to 210Å. A further single layer Ta_xGe_{1-x} sample of thickness 670Å was also investigated for comparison with the layered samples. By altering the layer thicknesses the dimensionality was varied from the 3D limit down to the 2D limit with consequences for both the low current and the high current dissipation regimes. The main results, which are summarised below, are expected to have relevance for all layered or low dimensional type-II superconductors.

In order to study the role of dimensionality in determining the superconducting properties it is necessary to know the T_c values and the characteristic length scales associated with each of the samples. The zero field fluctuation conductivity was extracted from the resistive transitions and fitted to the simple Aslamasov–Larkin predictions yielding T_c values in the range 0.882 to 2.802 K, with the lower values corresponding samples with pure Ta layers. Apart from one of the samples with relatively thin Ge layers the 2D form of the theory gave a better description of the measured data than the 3D form. Following this the perpendicular upper critical fields of the samples were determined from the in-field fluctuation conductivity using the scaling theory of Ullah and Dorsey. Once again the 2D form generally provided a better scaling fit except for the sample mentioned above for which the data collapsed very convincingly under the 3D scaling laws. For some of the other strongly coupled samples the dimensionality was hard to judge from the scaling analysis, possibly due to the effects of disorder on the width of the tansitions. The upper critical fields were used to find

the in-plane coherence length ξ_{ab} which ranged in value from 75 to 133Å, with the pure Ta multilayers tending to have slightly larger values than the alloyed multilayers. The in-plane penetration depth λ_{ab} was also determined from T_c and the zero temperature resistivity and was found to lie between 11000 and 20000Å, with the larger values once again corresponding to the pure Ta multilayers. The ratio $\kappa = \lambda_{ab}/\xi_{ab}$ was between 70 and 90 for all of the samples. These values are comparable to those found in other highly disordered low-T_c systems, and also lie much closer to the values observed in the high-T_c superconductors than do conventional low-T_c materials.

An attempt was made to treat the parallel field fluctuation conductivity in the same manner as above, but only for the samples with strongly coupled superconducting layers could a reasonable scaling collapse be obtained. For these the scaling was used to deduce $H_{c2||}$ which in turn was used to define the anisotropy parameter γ. The anisotropy values ranged between 1.5 and 10 and increased with increasing Ge layer thickness or with decreasing Ta or Ta_xGe_{1-x} thickness. For the less strongly coupled samples it was noted that the resistive transitions were considerably less broad in the parallel field orientation, enabling an accurate determination of $H_{c2||}$ using a simple resistance criteria. The temperature dependence of $H_{c2||}$ for the strongly decoupled samples was generally consistent with the square root form expected in 2D, and for the Ta_xGe_{1-x} multilayer samples the magnitude also agreed with the theoretical predictions.

The zero field IV curves of each of the 2D samples were examined as a function of temperature and found to be consistent with the form predicted by the Berezinskii-Kosterlitz-Thouless theory in which the resistive transition is governed by the unbinding of thermally created vortex-antivortex pairs. The Ta_xGe_{1-x} samples showed the predicted jump in the exponent of the power law describing the IV curves at a temperature which agreed with the theoretically predicted BKT transition. For two of the pure Ta multilayers the transition temperature was somewhat lower than expected. For one of these samples the disagreement between theory and experiment may relate either to screening effects or to mixing at the layer boundaries, however the disagreement is harder to explain for the other sample. Overall the results provide a nice validation of the zero field BKT theory for 2D superconductors.

The above results define the range of fields and temperatures over which the samples are in the superconducting state, however finite dissipation is still possible within this range due to thermally assisted flux creep. Tremendous effort has been put into gaining an understanding of this phenomena in layered type-II materials like the high-T_c superconductors because it places severe restrictions

on the conditions under which the benefits of dissipationless current flow can be utilised. The activation barriers relating to the thermally activated motion were measured for a wide range of multilayer samples and three qualitatively different regimes were found. In the strongly coupled samples or in the (relatively thick) single layer alloy the activation energy was proportional to the intervortex spacing and independent of the sample thickness or the individual layer thicknesses. This barrier was identified as a plastic barrier corresponding to a 3D viscous vortex liquid phase. In the decoupled samples with thick superconducting layers the activation energies were much smaller and showed a logarithmic dependence on the applied field. This indicated that the dominant mode of flux motion was the creep of dislocations in the 2D vortex lattice for which the activation energy is finite due to the disorder in the lattice. For the decoupled multilayers with the thinnest superconducting layers an interesting crossover is observed in the activation energy at a field dependent temperture T_x. The activation energy has a logarithmic field dependence both above and below T_x, although with different coefficients in each case. Below T_x the dissipation was shown to be the same as that in the thicker samples i.e. motion of dislocations, while above T_x the resistivity was dominated by the motion of small scale paired dislocations. This is in contrast to the explanations proposed to explain similar crossovers seen in other systems which involved phase transitions in the vortex state.

At lower fields and temperatures the samples which showed 3D type behaviour also exhibited signs of a transition into a vortex glass state in which the activation barriers diverge with decreasing current. Reasonable agreement was found with the predicted scaling behaviour in the vortex glass model, especially in the sample with the largest total thickness. Some evidence for vortex glass like correlations were also observed in one of the decoupled samples with thick superconducting layers, however the correlations were cut off by the finite layer thickness so that no true glass phase resulted. In the decoupled samples with thin superconducting layers there was no evidence for a vortex glass transition at finite temperature, although the IV curves did show some evidence for the existence of 2D glass-like correlations. These results clearly demonstrate the absence of a vortex glass state in two dimensions and also highlight the decreased effectiveness of the pinning forces at preventing vortex motion in thin superconducting layers.

One of the most unique aspects of this study was the ability to trace the superconducting behaviour over the whole range of currents from the low current regime described above to the high current regime in which an instability exists in the vortex solid that provides an absolute limit to the sustainable supercurrent. This instability was shown to be of a type predicted by Larkin and

Ovchinnikov, including quantitative agreement between the measured and theoretically expected values of the critical vortex velocity. The instability also showed a characteristic broadening at fields and temperatures close to H_{c2} which was shown to be affected both by the strength of the pinning forces and by the state of the vortices prior to the instability point.

Appendix A

Temperature Dependence of the Thermal Activation Energies

Because they depend on the characteristic length scales of the samples the activation energies are generally a function of temperature as well as magnetic field. Close to T_c the temperature dependence can be separated from the field dependence so that the activation energy can be written [151]

$$U(H,T) = U(H)(1 - T/T_c)^q \tag{A.1}$$

where q is expected to lie between 0.5 and 2. For example, the plastic activation barriers discussed in Section 5.3.5 all depend on $1/\lambda_{ab}^2 \propto (1-T/T_c)$ so that $q = 1$. The activated resistance takes the form $R = R_0 \exp(-U(H,T)/k_B T)$ so for $q = 1$ an Arrhenius plot has the slope

$$\frac{d \ln R}{dT^{-1}} = -U(H) \tag{A.2}$$

independent of T. The measured Arrhenius plot slopes therefore give a measure of the zero temperature field dependence of the activation energy, while the temperature dependence is reflected in the prefactor R_0. This is valid as long as the temperature range over which the slope is measured is small so that the plot remains linear, a condition which is met in most cases due to the steepness of the Arrhenius plots. For other values of q the measurement of $U(H)$ is not so simple, however the results of Section 6.3 showed that the Ta_xGe_{1-x}/Ge systems studied here can be well described by assuming $q = 1$.

Bibliography

[1] H. Kamerlingh Onnes, Leiden Comm. **120b, 122b, 124c** (1911).

[2] M. Tinkham, *Introduction to Superconductivity*, 2nd ed. (McGraw-Hill, New York, 1996).

[3] *Superconductivity*, edited by R. D. Parks (Marcel Dekker, New York, 1969).

[4] V. L. Ginzburg and L. D. Landau, Zh. Eksp. i. Teor. Fiz. **20**, 1064 (1950).

[5] J. G. Bednorz and K. A. Müller, Z. Phys. B **64**, 189 (1986).

[6] G. Blatter *et al.*, Rev. Mod. Phys. **66**, 1125 (1994).

[7] J. Bardeen, L. N. Cooper, and J. R. Schreiffer, Phys. Rev. **108**, 1175 (1957).

[8] M. C. Hellerqvist *et al.*, Phys. Rev. Lett. **76**, 4022 (1996).

[9] M. C. Hellerqvist and A. Kapitulnik, Phys. Rev. B **56**, 5521 (1997).

[10] J. A. Fendrich *et al.*, Phys. Rev. Lett **77**, 2073 (1996).

[11] S. Bhattacharya and M. J. Higgins, Phys. Rev. B **52**, 64 (1995).

[12] W. Henderson, E. Y. Andrei, M. J. Higgins, and S. Bhattacharya, Phys. Rev. Lett. **77**, 2077 (1996).

[13] A. C. Marley, M. J. Higgins, and S. Bhattacharya, Phys. Rev. Lett. **74**, 3029 (1995).

[14] W. K. Kwok *et al.*, Phys. Rev. Lett. **76**, 4596 (1996).

[15] A. I. Larkin and Y. N. Ovchinnikov, Zh. Eksp. Teor. Fiz. **31**, 1915 (1975), [Sov. Phys. JETP **41**, 960 (1976)].

[16] A. I. Larkin and Y. N. Ovchinnikov, in *Nonequilibrium Superconductivity*, edited by D. N. Langenberg and A. I. Larkin (North-Holland, Amsterdam, 1986), p. 493.

[17] H. L. Johnson, Ph.D. thesis, Victoria University of Wellington, 1993.

[18] S. T. Ruggiero, T. W. Barbee, Jr., and M. R. Beasley, Phys. Rev. Lett. **45**, 1299 (1980).

[19] S. T. Ruggiero, T. W. Barbee, Jr., and M. R. Beasley, Phys. Rev. B **26**, 4894 (1982).

[20] P. Koorevaar, P. H. Kes, A. E. Koshelev, and J. Aarts, Phys. Rev. Lett. **72**, 3250 (1994).

[21] P. Berghuis and P. H. Kes, Phys. Rev. B **47**, 262 (1993).

[22] P. Berghuis, A. L. F. van der Slot, and P. H. Kes, Phys. Rev. Lett. **65**, 2583 (1990).

[23] W. R. White, A. Kapitulnik, and M. R. Beasley, Phys. Rev. Lett. **70**, 670 (1993).

[24] W. R. White, A. Kapitulnik, and M. R. Beasley, Phys. Rev. Lett. **66**, 2826 (1991).

[25] D. Ephron, A. Yazdani, A. Kapitulnik, and M. R. Beasley, Phys. Rev. Lett. **76**, 1529 (1996).

[26] A. Yazdani *et al.*, Phys. Rev. Lett. **70**, 505 (1993).

[27] O. Brunner *et al.*, Phys. Rev. Lett. **67**, 1354 (1991).

[28] D. P. Norton and D. H. Lowndes, Phys. Rev. B **48**, 6460 (1993).

[29] S. Vadlamannati *et al.*, Phys. Rev. B **44**, 7094 (1991).

[30] N. Y. Fogel, V. G. Cherkasova, O. A. Koretzkaya, and A. S. Sidorenko, Phys. Rev. B **55**, 85 (1997).

[31] D. Neerinck *et al.*, Phys. Rev. Lett. **67**, 2577 (1991).

[32] T. W. Haywood and D. G. Ast, Phys. Rev. B **18**, 225 (1978).

[33] C. Li *et al.*, in *Materials Research Society Symposium Proceedings*, edited by J. M. Gibson (Materials Research Society, Pittsburgh, Pennsylvania, 1986), Vol. 56, p. 177.

[34] P. L. Gammel, A. F. Hebard, and D. J. Bishop, Phys. Rev. Lett. **60**, 144 (1988).

[35] A. V. Samoilov *et al.*, Phys. Rev. Lett. **75**, 4118 (1995).

[36] H. L. Johnson and H. J. Trodahl, J. Phys. Condens. Matter **7**, 1159 (1995).

[37] L. J. Törnquist, Master's thesis, Victoria University of Wellington, 1997.

[38] S. Rupp, Master's thesis, Victoria University of Wellington, 1997.

[39] G. V. M. Williams, Ph.D. thesis, Victoria University of Wellington, 1990.

[40] H. J. Trodahl *et al.*, Phys. Rev. B **53**, 15265 (1996).

[41] P. N. Baker, Thin Solid Films **14**, 3 (1972).

[42] A. G. Jackson and T. W. Haas, J. Vac. Sci. and Technol. **4**, 42 (1967).

[43] M. P. A. Fisher, Phys. Rev. Lett. **62**, 1415 (1989).

[44] D. S. Fisher, M. P. A. Fisher, and D. Huse, Phys. Rev. B **43**, 130 (1991).

[45] S. Kumar and H. J. Trodahl, J. Appl. Phys. **73**, 1761 (1992).

[46] A. Edgar, private communication, 1997.

[47] D. Belitz and T. R. Kirkpatrick, Revs. Mod. Phys. **66**, 261 (1994), and references therein.

[48] B. Y. Jin and J. B. Ketterson, Advances in Physics **38**, 189 (1989).

[49] W. E. Lawrence and S. Doniach, in *Proc. 12th Int. Conf. Low Temp. Phys.*, edited by E. Kanda (Academic Press, Tokyo, 1971), p. 361.

[50] N. R. Werthamer, E. Helfand, and P. C. Hohenberg, Phys. Rev. **147**, 295 (1966).

[51] L. P. Gor'kov, Zh. Eksp. i. Teor. Fiz. **36**, 1918 (1959), [Sov. Phys. JETP **9**, 1364 (1959)].

[52] A. A. Abrikosov, Zh. Eksp. i. Teor. Fiz. **32**, 1442 (1957), [Sov. Phys. JETP **5**, 1174 (1957)].

[53] G. Blatter, V. B. Geshkenbein, and A. I. Larkin, Phys. Rev. Lett. **68**, 875 (1992).

[54] G. Deutcher and O. Entin-Wohlman, Phys. Rev. B **17**, 1249 (1978).

[55] L. P. Gor'kov, Zh. Eksp. i. Teor. Fiz. **37**, 833 (1959), [Sov. Phys. JETP **10**, 593 (1960)].

[56] L. G. Aslamasov and A. I. Larkin, Phys. Rev. Lett. **26A**, 238 (1968).

[57] W. J. Skocpol and M. Tinkham, Rep. Prog. Phys. **38**, 1049 (1975).

[58] S. Ullah and A. T. Dorsey, Phys. Rev. Lett. **65**, 2066 (1990).

[59] S. Ullah and A. T. Dorsey, Phys. Rev. B **44**, 262 (1991).

[60] U. Welp *et al.*, Phys. Rev. Lett. **67**, 3180 (1991).

[61] D. H. Kim, K. E. Gray, and M. D. Trochet, Phys. Rev. B **45**, 10801 (1992).

[62] M. H. Theunissen and P. H. Kes, Phys. Rev. B **55**, 15183 (1997).

[63] W. Lang, G. Heine, W. Kula, and R. Sobolewski, Phys. Rev. B **51**, 9810 (1995).

[64] J. Pearl, Appl. Phys. Lett. **5**, 65 (1964).

[65] V. L. Berezinskii, Sov. Phys. JETP **32**, 4936 (1970).

[66] V. L. Berezinskii, Sov. Phys. JETP **34**, 610 (1971).

[67] J. M. Kosterlitz and D. J. Thouless, J. Phys. C **6**, 1181 (1973).

[68] J. M. Kosterlitz, J. Phys. C **7**, 1046 (1974).

[69] M. V. Feigel'man, V. B. Geshkenbein, and A. I. Larkin, Physica (Amsterdam) **167C**, 177 (1990).

[70] A. M. Kadin, K. Epstein, and A. M. Goldman, Phys. Rev. B **27**, 6691 (1983).

[71] A. T. Fiory, A. F. Hebard, and W. I. Glaberson, Phys. Rev. B **28**, 5075 (1983).

[72] S. Martin *et al.*, Phys. Rev. Lett. **62**, 677 (1989).

[73] E. H. Brandt, Phys. Rev. Lett. **63**, 1106 (1989).

[74] A. Houghton, R. A. Pelcovits, and A. Sudbø, Phys. Rev. B **40**, 6763 (1989).

[75] B. I. Halperin and D. R. Nelson, J. Low Temp. Phys. **36**, 599 (1979).

[76] F. R. N. Nabarro, *Theory of Dislocations* (Clarendon, Oxford, 1967).

[77] E. H. Brandt, Phys. Rev. B **34**, 6514 (1986).

[78] D. S. Fisher, Phys. Rev. B **22**, 1190 (1980).

[79] J. R. Clem, Phys. Rev. B. **43**, 7837 (1991).

[80] D. R. Nelson, Phys. Rev. Lett. **60**, 1973 (1988).

[81] J. R. Clem, Supercond. Sci. Technol. **5**, S33 (1992).

[82] M. Tachiki and S. Takahashi, Solid State Comm. **72**, 1083 (1989).

[83] M. Machida and H. Kaburaki, Phys. Rev. Lett. **74**, 1434 (1995).

[84] A. Gurevich, E. Kadyrov, and D. C. Larbalestier, Phys. Rev. Lett. **77**, 4078 (1996).

[85] H. Safar *et al.*, Phys. Rev. Lett. **69**, 824 (1992).

[86] W. K. Kwok *et al.*, Phys. Rev. Lett. **72**, 1092 (1994).

[87] R. Liang, D. A. Bonn, and W. N. Hardy, Phys. Rev. Lett. **76**, 835 (1996).

[88] U. Welp *et al.*, Phys. Rev. Lett. **76**, 4809 (1996).

[89] A. Schilling *et al.*, Nature **382**, 791 (1996).

[90] A. Schilling *et al.*, Phys. Rev. Lett. **78**, 4833 (1997).

[91] A. Junod *et al.*, Physica C **275**, 245 (1997).

[92] E. Brezin, D. R. Nelson, and A. Thiaville, Phys. Rev. B **31**, 7124 (1985).

[93] S. Watauchi, H. Ikuta, J. Shimoyama, and K. Kishio, Physica C **259**, 373 (1996).

[94] D. T. Fuchs *et al.*, Phys. Rev. B **55**, 6156 (1997).

[95] E. Zeldov *et al.*, Nature **375**, 373 (1995).

[96] H. Pastoriza, M. F. Goffman, A. Arribére, and F. de la Cruz, Phys. Rev. Lett. **72**, 2951 (1994).

[97] J. A. Fendrich *et al.*, Phys. Rev. Lett. **74**, 1210 (1995).

[98] J. Bardeen and M. J. Stephen, Phys. Rev. **140**, 1197 (1965).

[99] A. I. Larkin and Y. N. Ovchinnikov, J. Low Temp. Phys. **34**, 409 (1979).

[100] T. Nattermann, Phys. Rev. Lett. **64**, 2454 (1990).

[101] M. C. Marchetti and D. R. Nelson, Phys. Rev. B **41**, 1910 (1990).

[102] V. M. Vinokur, P. H. Kes, and A. E. Koshelev, Physica (Amsterdam) **168C**, 29 (1990).

[103] A. Barone, A. I. Larkin, and Y. N. Ovchinnikov, J. Supercond. **3**, 155 (1990).

[104] B. I. Ivlev and N. B. Kopnin, J. Low Temp. Phys. **77**, 413 (1989).

[105] B. I. Ivlev and N. B. Kopnin, Phys. Rev. Lett. **64**, 1828 (1990).

[106] M. V. Feigel'man and V. M. Vinokur, Phys. Rev. B **41**, 8986 (1990).

[107] P. W. Anderson and Y. B. Kim, Rev. Mod. Phys. **36**, 39 (1964).

[108] P. Hänggi, P. Talkner, and M. Borkovec, Rev. Mod. Phys. **62**, 251 (1990).

[109] B. M. Forrest and L.-H. Tang, Phys. Rev. Lett. **64**, 1405 (1990).

[110] R. H. Koch *et al.*, Phys. Rev. Lett. **63**, 1511 (1989).

[111] P. L. Gammel, L. F. Schneemeyer, and D. J. Bishop, Phys. Rev. Lett. **66**, 953 (1991).

[112] H. Safar *et al.*, Phys. Rev. Lett. **68**, 2672 (1992).

[113] Q. Li *et al.*, Phys. Rev. B **50**, 4256 (1994).

[114] N.-C. Yeh *et al.*, Phys. Rev. Lett. **71**, 4043 (1993).

[115] W. Lang *et al.*, Z. Phys. B **100**, 13 (1996).

[116] N. W. Ashcroft and N. D. Mermin, *Solid State Physics* (HRW International Editions, CBS Publishing Asia Ltd., Philadelphia, 1987).

[117] F. Pardo *et al.*, Phys. Rev. Lett. **78**, 4633 (1997).

[118] M.-C. Miguel and M. Kardar, Phys. Rev. B **56**, 11903 (1997).

[119] Y. Abulafia *et al.*, Phys. Rev. Lett. **77**, 1596 (1996).

[120] A.-C. Shi and A. J. Berlinsky, Phys. Rev. Lett. **67**, 1926 (1991).

[121] A. V. Balatskii and V. M. Vinokur, Solid State Commun. **52**, 847 (1984).

[122] V. M. Vinokur, P. H. Kes, and A. E. Koshelev, Physica C **248**, 179 (1995).

[123] C. Dekker *et al.*, Phys. Rev. Lett. **69**, 2717 (1992).

[124] H. H. Wen *et al.*, Phys. Rev. Lett. **80**, 3859 (1998).

[125] V. M. Vinokur, M. V. Feigel'man, V. B. Geshkenbein, and A. I. Larkin, Phys. Rev. Lett. **65**, 259 (1990).

[126] L. D. Landau and E. M. Lifshitz, *Theory of Elasticity*, Vol. 7 of *Course in Theoretical Physics* (Pergamon, London/Paris, 1959).

[127] V. B. Geshkenbein, M. V. Feigel'man, A. I. Larkin, and V. M. Vinokur, Physica **162-164C**, 239 (1989).

[128] M. Tinkham, Phys. Rev. Lett. **61**, 1658 (1988).

[129] B. I. Ivlev and N. B. Kopnin, Phys. Rev. Lett. **64**, 1828 (1990).

[130] B. I. Ivlev and N. B. Kopnin, J. Low Temp. Phys. **80**, 161 (1990).

[131] S. Chakravarty, B. I. Ivlev, and Y. N. Ovchinnikov, Phys. Rev. B **42**, 2143 (1990).

[132] S. Chakravarty, B. I. Ivlev, and Y. N. Ovchinnikov, Phys. Rev. Lett. **64**, 3187 (1990).

[133] A. E. Koshelev and V. M. Vinokur, Phys. Rev. Lett. **73**, 3580 (1994).

[134] A. I. Bezuglyj and V. A. Shklovskij, Physica (Amsterdam) **202C**, 234 (1992).

[135] S. G. Doettinger, R. P. Huebener, and A. Kühle, Physica (Amsterdam) **251C**, 285 (1995).

[136] L. E. Musienko, I. M. Dmitrenko, and V. G. Volotskaya, JETP Lett. **31**, 567 (1980).

[137] W. Klein, R. P. Huebener, S. Gauss, and J. Parisi, J. Low Temp. Phys. **61**, 413 (1985).

[138] S. G. Doettinger *et al.*, Phys. Rev. Lett. **73**, 1691 (1994).

[139] Z. L. Xiao and P. Ziemann, Phys. Rev. B **53**, 15265 (1996).

[140] Z. L. Xiao, P. Voss-de Haan, G. Jakob, and H. Adrian, Phys. Rev. B **57**, 736 (1998).

[141] B. J. Ruck *et al.*, Phys. Rev. Lett. **78**, 3378 (1997).

[142] P. H. Kes and C. C. Tsuei, Phys. Rev. B **28**, 5126 (1983).

[143] Y. Matsuda *et al.*, Phys. Rev. B **48**, 10498 (1993).

[144] B. Brown, J. M. Roberts, J. Tate, and J. W. Farmer, Phys. Rev. B **55**, 8713 (1997).

[145] T. R. Chien, T. W. Jing, N. P. Ong, and Z. Z. Wang, Phys. Rev. Lett. **66**, 3075 (1991).

[146] H. H. Wen *et al.*, Phys. Rev. Lett. **79**, 1559 (1997).

[147] B. A. Huberman and S. Doniach, Phys. Rev. Lett. **43**, 950 (1979).

[148] S. Friemel and C. Pasquier, Physica C **265**, 121 (1996).

[149] M. P. A. Fisher, T. A. Tokuyasu, and A. P. Young, Phys. Rev. Lett. **66**, 2931 (1991).

[150] R. Kleiner and P. Muller, Phys. Rev. B **49**, 1327 (1994).

[151] T. T. M. Palstra *et al.*, Phys. Rev. B **41**, 6621 (1990).